Sputtering Deposition and Characterization of Topological Insulator BiSb – Ferromagnet Multilayers

18D18392

TUO Fan

A thesis submitted for the degree of Doctor of Engineering at

Tokyo Institute of Technology in 2021

Department of Electrical and Electronic Engineering

Supervisor: Prof. Dr. Pham Nam Hai

Acknowledgements

Eventually, I am approaching the end of my student career. There are numerous people who have given me supports in these years. It would be impossible for me to accomplish my Ph.D. work without them.

First of all, I would like to express my gratitude to my academic supervisor, Prof. Pham Nam Hai, who has instructed me for these three years with his professionalism, wisdom and enthusiasm. He is an excellent supervisor that not only teaches the knowledge and instruct the experiments, but also brings me to the research world, stimulates my inspiration and supports my academic life. I had felt annoyed in research, but he let me know its interest and value since I joined his group. He paid plenty of effort on my way from a rookie to a Ph.D. candidate. Three years are not long, but his advice will forever be invaluable in my future career.

I would like to specially appreciate my tutor, Dr. Nguyen Huynh Duy Khang. What he has helped me is much more than that of a tutor's responsibility. Almost all my experimental techniques, from sample growth to device fabrication and measurements, are learned from him. He is a real researcher with noble-minded and pure spirits, whose love to research deeply expressed me. His behaviors I have seen every day set a role model to me as a Ph.D. student and then a young researcher.

I would like to express the thankfulness to all of my former and current colleagues in this group. I am especially thankful to Hu Tianxiang, Yao Kenichiro and Shirokura Takanori. Hu and I know each other before I came to this lab. He has given me fruitful advice that made me adapt to the lab quickly. Yao has taught me the experiments and helped me understand the project at the beginning of my research. Shirokura has also given me much help in my research. I have acquired a lot from the beneficial discussion with him. I am also thankful to other members in this lab. Many people have provided me support in my work, such as Dr. Bui Cong Tinh, Nakano Soichiro, Ho Hoang Huy, and exchange student Mustafa Tobah. I also enjoy the times I spend with everyone that makes me not feel lonely in Japan. These years will be an unforgettable period in my memory.

I am grateful to Dr. Ohkubo Tadakatsu and engineer Uzuhashi Jun in National Institute for Material Science (NIMS). Dr. Ohkubo is my supervisor, and Uzuhashi is the instructor for my internship in NIMS. I have learned a lot from them for the structural and elemental analysis. This unique experience has broadened my horizon, and been a beneficial supplement for my student career.

I would like to thank the Material Analysis Division (especially technician Iida Yu) and Nakagawa Lab (especially Dr. Takamura Yota) in Tokyo Institute of Technology, and Tanaka Lab in the University of Tokyo, for the technical support in my work.

I acknowledge the financial support from JST-CREST and Tsubame Project of Tokyo Tech.

I appreciate Prof. Nakagawa Shigeki, Prof. Yamada Akira, Prof. Manaka Takaaki and Prof. Miyajima Shinsuke from Tokyo Tech, and Dr. Nakamura Shiho from Kioxia, for being the examiners of my Ph.D. thesis in their busy time.

Lastly, I owe the deepest gratitude and love to my dearest mom, dad and family. I am unable to succeed anything without their endless support, trust and encouragement. Words are not powerful to express my emotion. I hope I can have them around me forever.

In addition, I would like to share my gratitude and delightfulness with my wife. Although I don’t know yet where you are, I hope this regard in advance will bring you to my side as soon as possible.

Publications and presentations

Publications

[1] Khang N. H. D., **Fan T.**, and Hai P. N. Zero-field topological Hall effect as evidence of ground-state skyrmions at room temperature in BiSb/MnGa bilayers. AIP Adv. 9, 125309 (2019).

[2] **Fan T.**, Tobah M., Shirokura T., Khang N. H. D., and Hai P. N. Crystal growth and characterization of topological insulator BiSb thin films by sputtering deposition on sapphire substrates. Jpn. J. Appl. Phys. 59, 063001 (2020).

[3] **Fan T.**, Khang N. H. D., Shirokura T., Huy H. H., and Hai P. N. Low power spin–orbit torque switching in sputtered BiSb topological insulator/perpendicularly magnetized CoPt/MgO multilayers on oxidized Si substrate. Appl. Phys. Lett. 119, 082403 (2021).

[4] **Fan T.**, Khang N. H. D., Nakano S., and Hai P. N. Ultrahigh efficient spin-orbit torque magnetization switching in all-sputtered topological insulator-ferromagnet multilayers. arXiv:2007.02264, under review by Sci. Rep.

International conferences

[1] **Fan T.**, Tobah M., Shirokura T., Khang N. H. D., Hai P. N. Crystal Growth and Characterization of Topological Insulator BiSb Thin Films by Sputtering Deposition for SOT-MRAM Applications, SSDM 2020, Sept. 2020.

[2] **Fan T.**, Khang N. H. D., Nakano S., Hai P. N. Ultrahigh efficient spin-orbit-torque magnetization switching in sputtered topological insulator BiSb/$(Co/Pt)_2$ multilayers, 2020 Magnetism and Magnetic Materials, Nov. 2020.

[3] **Fan T.**, Khang N. H. D., Hai P. N. Low power spin-orbit torque magnetization switching in all-sputtered BiSb topological insulator / perpendicularly magnetized CoPt / MgO multilayers on Si substrate, 2022 Joint MMM-Intermag, Jan. 2022.

Domestic Conferences

[1] **Fan T.**, Tobah M., Shirokura T., Khang N. H. D., Hai P. N. Crystal Growth and Evaluation of BiSb Topological Insulator by Sputter Deposition, The 80th JSAP Autumn meeting, Sept. 2019.

[2] **Fan T.**, Khang N. H. D., Nakano S., Hai P. N. Ultrahigh efficient spin-orbit-torque magnetization switching in sputtered BiSb topological insulator and Co/Pt ferromagnetic multilayers, The 81th JSAP Autumn meeting, Sept. 2020.

[3] **Fan T.**, Khang N. H. D., Hai P. N. Low power spin-orbit torque magnetization switching in all-sputtered BiSb topological insulator / perpendicularly magnetized CoPt / MgO multilayers on Si substrate, 82th JSAP Autumn meeting, Sept. 2021.

Abstract

This thesis comprises the recent work on sputtering deposition and characterization of BiSb topological insulator – ferromagnet multilayers for spin orbit torque (SOT) – magnetoresistive random access memory (MRAM) mass production. BiSb is a promising candidate as the spin source of SOT-MRAM thanks to its giant spin Hall effect and high electrical conductivity. However, the previous work that demonstrated the high potential of BiSb are done by molecular beam epitaxy (MBE). For SOT-MRAM mass production, it is required to deposit high quality BiSb thin film and ferromagnetic free layer by sputtering deposition. In this thesis, we realize the SOT magnetization switching in an all sputtered BiSb – ferromagnet heterostructures, demonstrating the feasibility of BiSb as the spin source and the high potential of implementation of SOT-MRAM.

There are three main studies in this work. In the first part, we show that it is possible to deposit high quality quasi-single-crystal BiSb thin films by sputtering deposition with quality approaching that of MBE-grown epitaxial thin films. We confirmed the existence of surface states from the thickness-dependence and temperature-dependence of the electrical conductivity/resistivity. In the second part, the large spin Hall angle and high electrical conductivity is confirmed in all-sputtered BiSb – Co/Pt multilayers on sapphire substrate. The CoPt has a large perpendicular magnetic anisotropy (PMA) field, which is comparable to that of CoFeB/MgO, and satisfies the requirements for non-volatility. SOT switching is realized with power consumption 1 or 2 orders of magnitude smaller than that of other materials. In the third part, BiSb – Co/Pt multilayer with large PMA is deposited on Si/SiO_x substrate. The large spin Hall angle is demonstrated, and low power SOT magnetization switching is realized. In addition, we use scanning transmission electron microscope (STEM) and energy dispersive X-ray (EDX) spectroscopy to analyze

the elements distribution in different structures. The results can provide some guidance for our future works to further improve the spin Hall angle and by suppressing the Sb diffusion.

List of abbreviations

SOT	Spin orbit torque
STT	Spin transfer torque
MRAM	Magnetoresistive random access memory
GMR	Giant magnetoresistance
TMR	Tunneling magnetoresistance
MTJ	Magnetic tunnel junction
FM	Ferromagnetic
NM	Non-magnetic
TI	Topological insulator
DRAM	Dynamic random access memory
SRAM	Static random access memory
SHE	Spin Hall effect
SOI	Spin orbit interaction
ARPES	Angle resolved photoemission spectroscopy
MBE	Molecular beam epitaxy
SQUID	Superconducting quantum interference device
XRD	X-ray diffraction
AFM	Atomic force microscope
TEM	Transmission electron microscope
STEM	Scanning transmission electron microscope
EDX	Energy dispersive X-ray

List of symbols

e Electron charge

c Speed of light

$\hbar$ Reduced Planck constant

k_B Boltzmann constant

Contents

Chapter 1 Introduction **1**

1.1 Spintronics 1

1.2 Commercial spintronics devices 3

1.3 Spin-orbit-torque magnetoresistive random access memory 7

1.4 Motivation and thesis outline 8

Chapter 2 Fundamental physics of spin orbit torque in topological insulator BiSb **13**

2.1 Spin-orbit interaction 13

2.2 Spin Hall effect 14

2.3 Spin orbit torque 16

2.4 Topological insulator 17

2.5 A conductive topological insulator BiSb 19

2.6 Summary 22

Chapter 3 Crystal growth and characterization of BiSb thin films by sputtering deposition on sapphire substrates **27**

3.1 Introduction 27

3.2 Growth and characterization techniques 28

3.3 BiSb thin Film growth and characterization 30

3.4 Electrical measurements 37

3.5 Conclusion 45

Chapter 4 Ultrahigh efficient spin-orbit torque magnetization switching in all-sputtered topological insulator – ferromagnet multilayers **47**

4.1 Introduction 47

4.2 Sample growth and device fabrication 48
4.3 Characterization techniques 51
4.4 Spin Hall angle evaluation 54
4.5 Ultrahigh efficient spin-orbit torque magnetization switching by DC and pulse currents 60
4.6 Discussion 64
Chapter 5 Low power spin-orbit torque switching in sputtered BiSb topological insulator / perpendicularly magnetized CoPt / MgO multilayers on oxidized Si substrate 68
5.1 Introduction 68
5.2 Sample growth 70
5.3 Spin Hall angle evaluation 71
5.4 SOT magnetization switching by DC and pulse currents 75
5.5 Discussion 80
Chapter 6 Structure analysis by transmission electron microscope 83
6.1 Introduction 83
6.2 Characterization technique: transmission electron microscope 84
6.3 Sample growth and specimen processing 84
6.4 Experimental results 87
6.5 Discussion 93
Chapter 7 Conclusion 95

Chapter 1 Introduction

Spintronics has stepped into its golden era with the discovery of various breakthroughs. It has become an important pillar of modern electronics. Along with the development of spintronics, high-density data storage has evolved generation by generation and contributed to various aspects of day life. In this chapter, we present a brief overview of spintronics. The data storage technology based on spintronics will be introduced, with emphasis on Spin orbit torque (SOT) – magnetoresistive random access memory (MRAM), which is considered as a highly promising next generation non-volatile memory. We will introduce a potential solution for mass production of SOT-MRAM that uses topological insulator (TI) BiSb as the spin Hall material, which will be presented in details by the experiments in following chapters. The motivation and outline of this work will be introduced.

1.1 Spintronics

Spintronics, also known as spin electronics, is a subfield of electronics that studies and takes advantages of both the charge and spin of electrons. It is universally recognized that spintronics stepped into its golden era with the discovery of the giant magnetoresistance (GMR) effect independently by Fert [1] and Grünberg [2] in 1988. As shown in Figure 1.1, the resistance of Fe/Cr multilayers changes by 3% at room temperature and 50% at 4.2 K under an external magnetic field, which is much larger than the anisotropy magnetoresistance effect, and thus named as GMR effect. In a system with two ferromagnetic (FM) layers separated by a non-magnetic (NM) layer, the resistance is significantly larger when the magnetization of FM layers are anti-parallel than when the magnetization are parallel. It is revealed that the magnetoresistance depends on the spin-dependent scattering of electrons at the FM/NM interface of in the FM layers. On the other hand, tunneling magnetoresistance (TMR) effect was discovered in 1975 [3], that in a magnetic tunnel junction (MTJ) with two FM layers separated by a thin insulating layer, electrons can transport through the insulating layer perpendicular to film plane by the quantum tunneling effect. The TMR effect is the result of the spin-dependent quantum tunneling effect that electrons in one FM layer can pass through the insulating layer only in case that the spin polarization of electrons in another FM is the same. Therefore, the multilayers have low resistance because the tunneling probability of electrons is high when the magnetization of two FM layers are parallel, i.e., the majority of electrons have same spin polarization. Figure 1.2 shows the schematic of TMR in parallel and anti-parallel states. With the intensive development on spintronics, the TMR ratio was enhanced to 604% in 2008 [4].

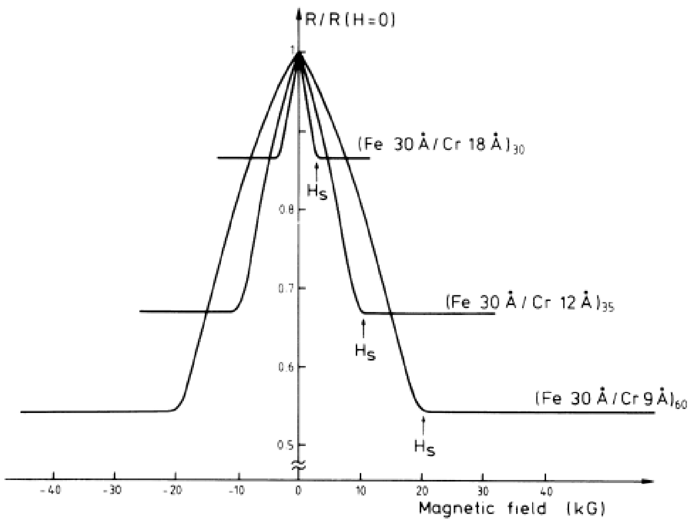

Figure 1.1 GMR effect in Fe/Cr superlattice at 4K [1]. Reprinted figure with permission from Baibich M. N. et al., Phys. Rev. Lett., 61, 2472 (1988). Copyright (2022) by the American Physical Society.

The large TMR effect is considered to drive the evolution of non-volatile magnetic memories. In traditional electronics, low and high voltages are used to express the binary bit ‘0’ and ‘1’, respectively. It requires power supply to refresh the bit states in case of the loss of charge. On the other hand, a “spintronics” device uses spin, which is the intrinsic attribute of electrons, to represent the bit states, such that the device does not need power supply to preserve the states. Based on TMR effect, the high and low resistance in MTJ can be used to express the bit ‘0’ and ‘1’. By utilizing permanent magnets, the long-lifetime non-volatility can be expected thanks to its enduring magnetization [5-11]. Therefore, spintronics is highly expected for the application in next generation electronics, especially non-volatile memory devices [12].

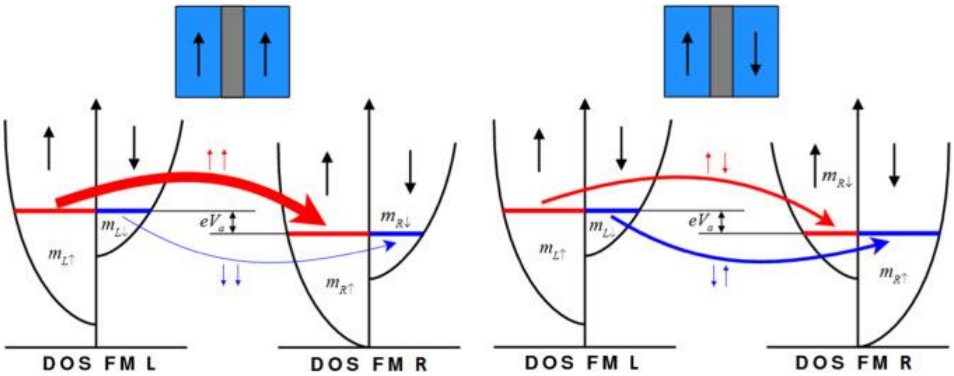

Figure 1.2 TMR in parallel (left) and anti-parallel (right) states [13]. Reprinted figure with permission from Petukhov D. A. et al., Physica E, 80, 31 (2016). Copyright (2022) by Elsevier.

1.2 Commercial spintronics devices

In this section, we introduce some spintronics memory devices that have already been mass produced. In recent decades, the application of TMR effect has been expanded to several commercial devices. The devices belong to two major types: magnetic read head and MRAM.

Magnetic read head

The first application of TMR effect and MTJ is the magnetic read head [14, 15]. As introduced before, the high and low resistance of MTJ can be expressed as the bit '0' and '1' respectively. Therefore, in order to manipulate the bit state, it is necessary to change the state of two FM layers to parallel or antiparallel. In the reading element of magnetic read head using MTJ, one of the FM layers has relatively small magnetic anisotropy field, which is referred to as the free layer. The magnetization of the free layer senses the stray field from the medium. The other FM layer is referred to as reference layer, whose magnetization is fixed. The resistance of the read head device, which will change according to the alignment of magnetization of free layer and reference layer, can be sensed to read the data.

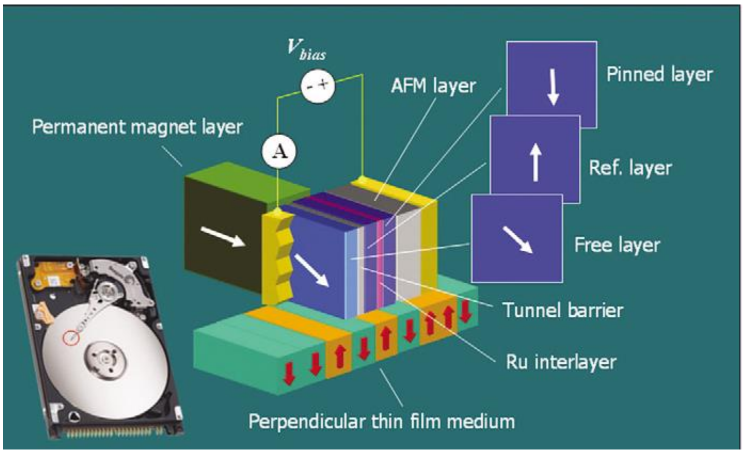

Figure 1.3 Magnetic read head in HDD [14]. Reprinted figure with permission from Zhu J., et al. Mater. Today 9, 36 (2006). Copyright (2022) by Elsevier.

There are technical challenges in commercialization of magnetic read head. In order to fix the magnetization of reference layer, it is antiferromagnetically coupled with a pinned layer through a metallic interlayer. The pinned layer is constrained by the exchange bias field arises from an antiferromagnet interface. The demagnetizting field of the reference layer can be compensated by the pinned layer. FM with high spin polarization such as CoFe and CoFeB are good candidate for the reference layer and pinned layer for high sensitivity. Another key requirement is to improve the signal-to-noise ratio (SNR) by operating the device in single domain mode. This requirement is realized by applying a biasing longitudinal magnetic field using a pair of permanent magnet. Furthermore, higher TMR ratio is required for higher SNR and higher data rate. Thus, MgO is so far the best candidate for the tunnel barrier layer. The TMR read head using MgO barrier layer has helped realize the bit density of over 1 Tbit/cm^2 [16]. Compared with the TMR read head using other amorphous barrier layer such as AlO_x, the data rate is improved by 2 – 3 times up to 2015.

Magnetoresistive random access memory

MRAM is another spintronics device based on TMR effect. Compared with other charge-based memory devices such as dynamic random access memory (DRAM) or static random access memory (SRAM), MRAM does not need power supply to preserve the bit states. It uses the magnetic state of the free layer and reference layer, which is parallel or anti-parallel, to store the data bits. Thus, the most significant advantages of MRAM are non-volatility, fast operation (~ 10 ns), and long lifetime. In the early days of MRAM, the Oersted magnetic field generated by a nearby current is used to manipulate the magnetization direction of the free layer as shown in Figure 1.3(a) (toggle MRAM). However, this technique requires a large current to switch the magnetization, making the bit density limited. Therefore, the largest capacity of toggle MRAM produced by Everspin is only 32 Mb. Nevertheless, its non-volatility, high speed and long lifetime has attracted the interest for further exploration of MRAM.

The improvement of switching efficiency is required for next-generation MRAM. It is found that spin transfer torque (STT) induced by a spin polarized current can lead to the magnetization switching in FM layer of MTJ [17]. This phenomenon is theoretically predicted [18, 19] and experimentally demonstrated [20-22] in 1996 and 1999, respectively. As shown in Figure 1.3(b), when a current pass through the reference layer, the spin of electrons is polarized. When the spin-polarized current is injected to the free layer, STT is generated to switch the magnetization.

However, there still remains some limitation of STT-MRAM that make it difficult to further reduce the writing current. The writing current and writing energy of STT-MRAM is still larger than that of SRAM or DRAM by 1 order of magnitude. Similar to the toggle MRAM, the large writing current will also limit the bit density of STT-MRAM [23]. Moreover, writing and reading process share one path in STT-MRAM, making it vulnerable to tunneling barrier breakdown [24, 25]. Therefore, magnetization switching by even smaller writing current is highly required for higher bit density and reliability.

The reason of large writing current I_c is the low efficiency of charge-to-spin conversion in the STT technique. The spin current in STT-MRAM is given by: $I_s = (\hbar/2e)PI_c$. In this equation, the spin polarization P cannot exceed 1 because $P = (n\uparrow - n\downarrow) / (n\uparrow + n\downarrow)$, where $n\uparrow$ and $n\downarrow$ are up-spin and down-spin electron density, respectively. This fact limits the spin current generation efficiency.

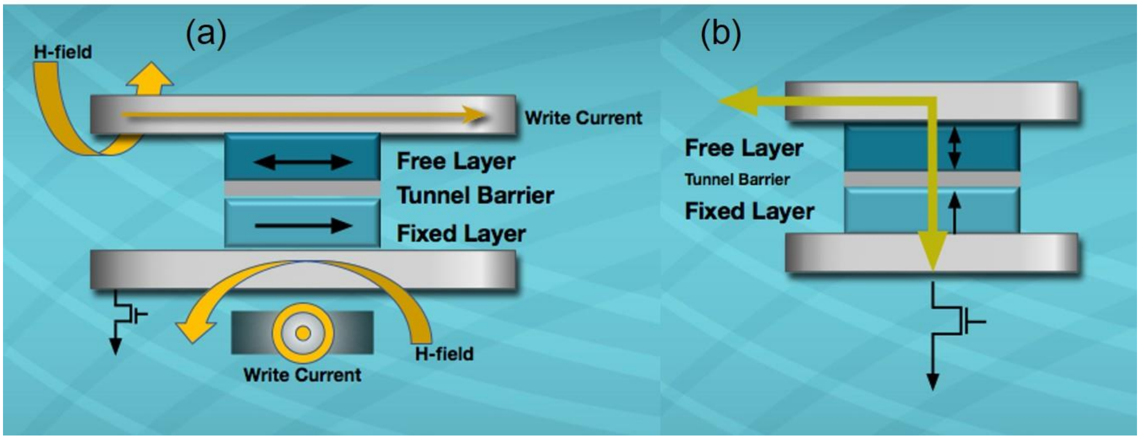

Figure 1.4 **(a)** Toggle MRAM and **(b)** STT-MRAM. Source: Everspin.

1.3 Spin-orbit-torque magnetoresistive random access memory

It is reported that a different torque, spin-orbit-torque (SOT), can become a more efficient way to switch the magnetization [26]. The SOT effect inspires the exploration of SOT-MRAM [27]. The structure of a bit cell of SOT-MRAM is shown in Figure 1.4. In SOT-MRAM, there is a spin Hall layer in contact with the free layer. The up-spin and down-spin electrons split up to opposite direction because of the spin Hall effect (SHE) when a charge current flows in the spin Hall layer. The pure spin current generated by SHE can exert a torque in the free layer, which drives the magnetization switching.

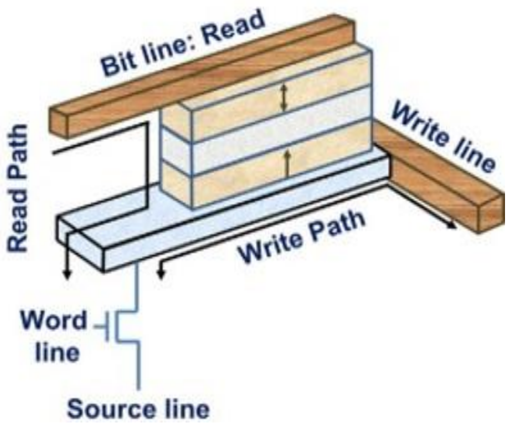

Figure 1.5 Bit cell of SOT-MRAM [12]. Reprinted figure with permission from

Bhatti S., et al. Mater. Today 20, 530 (2017). Copyright (2022) by Elsevier.

SOT-MRAM becomes the best hope as the next generation MRAM for high bit density, fast writing speed and high durability. The spin current in SOT-MRAM is given by $I_s = (\hbar/2e)(L/t)\theta_{SH}I_c$, where θ_{SH} is the spin Hall angle, L is the length of MTJ and t is thickness of spin Hall layer. Here, θ_{SH} represents the strength of the SHE. The factor $(L/t)\theta_{SH}$ can be much larger than unity if the spin Hall angle is large enough, which means the SOT-MRAM can generate a much large spin current than STT-MRAM by a same charge current. Furthermore, the read and write path are separated in SOT-MRAM, because the writing current is applied in the spin Hall layer without flowing into the MTJ and read line. Finally, since the spin-polarization of the pure spin current is perpendicular to the magnetization direction of the free magnetic layer, the spin torque is maximized and the magnetization can switch very fast (< ns) in SOT-MRAM with PMA. These characteristics make SOT-MRAM very promising for higher writing speed, lower writing energy and higher reliability compared with STT-MRAM.

According to the relationship between charge current and spin current in SOT-MRAM, the most important parameter is the spin Hall angle of the spin Hall layer. In this work, we select the BiSb, a topological insulator (TI) which has a spin Hall angle larger than 10, as the spin Hall material. The fundamental physics of SHE in BiSb will be explained in chapter 2.

1.4 Motivation and thesis outline

For mass production of SOT-MRAM, the following three minimum requirements must be satisfied for spin Hall material: (1) large spin Hall angle, (2) large electrical conductivity, and (3) can be deposited using industry friendly techniques, such as sputtering deposition. TI BiSb has shown its high potential thanks to its large spin Hall angle and high electrical conductivity, but in previous works it was deposited by the molecular beam epitaxy method. Meanwhile, it needs to be deposited by sputtering deposition in realistic SOT-MRAM. Moreover, the free layer is needed to have large PMA for long time non-volatility. This research investigated heterostructures of TI BiSb – FM Co/Pt multilayers with PMA by sputtering deposition, which can be a possible solution for the spin Hall layer – free layer in SOT-MRAM.

In this thesis, we introduce the background and fundamental physics in Chapter 1 and 2, respectively. These two chapters show the bright prospect of SOT-MRAM, and explain why we use TI BiSb for the spin current source in SOT-MRAM, and the necessity of BiSb deposition by sputtering. In Chapter 3, we demonstrate the deposition of high quality BiSb thin films with high electrical conductivity by sputtering deposition. In Chapter 4, the large spin Hall angle of BiSb is demonstrated in BiSb / FM CoPt multilayers, and the ultrahigh efficient SOT magnetization switching is achieved. In Chapter 5, the low power SOT magnetization switching is realized in BiSb/CoPt deposited on Si/SiO_x substrate. Chapter 6 presents some solutions to increase the spin Hall angle through transmission electron microscope (TEM) images and energy dispersive X-ray (EDX) spectroscopy. We conclude this work and propose future works in Chapter 7.

References

[1] Baibich M. N., et al. Giant magnetoresistance of (001) Fe/(001) Cr magnetic superlattices. Phys. Rev. Lett. 61, 2472 (1988).

[2] Binasch G., et al. Enhanced magnetoresistance in layered magnetic structures with

antiferromagnetic interlayer exchange. Phys. Rev. B 39, 4828 (1989).

[3] Julliere M. Tunneling between ferromagnetic films. Phys. Lett. A 54, 225 (1975).

[4] Ikeda S., et al. Tunnel magnetoresistance of 604% at 300 K by suppression of Ta diffusion in CoFeB/MgO/CoFeB pseudo-spin-valves annealed at high temperature." Appl. Phys. Lett. 93, 082508 (2008).

[5] Žutić I., et al. Spintronics: Fundamentals and applications. Rev. of Mod. Phys. 76, 323 (2004).

[6] Wolf S. A., et al. Spintronics: a spin-based electronics vision for the future. Science 294.5546, 1488 (2001).

[7] Kang S. H., et al. Emerging materials and devices in spintronic integrated circuits for energy-smart mobile computing and connectivity. Acta Mater. 61, 952 (2013).

[8] Aradhya S. V., et al. Nanosecond-timescale low energy switching of in-plane magnetic tunnel junctions through dynamic Oersted-field-assisted spin Hall effect. Nano Lett. 16, 5987 (2016).

[9] Yang S., et al. Domain-wall velocities of up to 750 ms^{-1} driven by exchange-coupling torque in synthetic antiferromagnets. Nature Nanotechnol. 10, 221 (2015).

[10] Parkin S., et al. Magnetic domain-wall racetrack memory. Science 320.5873, 190 (2008).

[11] Hirohata A., et al. Future perspectives for spintronic devices. J. Phys. D: Appl. Phys. 47, 193001 (2014).

[12] Bhatti S., et al. Spintronics based random access memory: a review. Mater. Today 20, 530 (2017).

[13] Petukhov D. A. Spin-polarized current and tunnel magnetoresistance in heterogeneous single-barrier magnetic tunnel junctions. Phys. E: Low-Dimens. Syst.

Nanostructures 80, 31 (2016).

[14] Zhu J., et al. Magnetic tunnel junctions. Mater. Today 9, 36 (2006).

[15] Mao S., et al. Commercial TMR heads for hard disk drives: characterization and extendibility at 300 Gbit/in^2. IEEE Trans. Magn. 42, 97 (2006).

[16] Ando Y. Spintronics technology and device development. Jpn. J. Appl. Phys. 54, 070101 (2015).

[17] Wang K. L., et al. Low-power non-volatile spintronic memory: STT-RAM and beyond. J. Phys. D: Appl. Phys 46, 074003 (2013).

[18] Slonczewski J. Current-driven excitation of magnetic multilayers. J. Magn. Magn. Mater. 159, L1 (1996).

[19] Berger L. Emission of spin waves by a magnetic multilayer traversed by a current. Phys. Rev. B 54, 9353 (1996).

[20] Myers E. B., et al. Current-induced switching of domains in magnetic multilayer devices. Science 285.5429, 867 (1999).

[21] Tsoi M., et al. Excitation of a magnetic multilayer by an electric current. Phys. Rev. Lett. 80, 4281 (1998).

[22] Wegrowe J., et al. Current-induced magnetization reversal in magnetic nanowires. Europhys. Lett. 45, 626 (1999).

[23] Ramaswamy R. et al. Recent advances in spin-orbit torques: Moving towards device applications. Appl. Phys. Rev. 5, 031107 (2018).

[24] Zhao W. S. et al. Failure and reliability analysis of STT-MRAM. Microelectron. Reliab. 52, 1848 (2012).

[25] Panagopoulos G., et al. Modeling of dielectric breakdown-induced time-dependent STT-MRAM performance degradation. 69th Device Research Conference. IEEE,

2011.

[26] Han X., et al. Spin-orbit torques: Materials, physics, and devices. Appl. Phys. Lett. 118, 120502 (2021).

[27] Garello K., et al. Manufacturable 300 mm platform solution for Field-Free Switching SOT-MRAM. 2019 Symposium on VLSI Technology, JFS4-5 (2019).

Chapter 2 Fundamental physics of spin orbit torque in topological insulator BiSb

In this chapter, we briefly explain the spin orbit interaction (SOI) and SHE, which can generate a pure spin current by the charge current. The SOT is introduced as a result of SHE, which can switch the magnetization in NM/FM heterostructure. We introduce the TI BiSb with emphasis on its surface states with strong SOI, and its unique characteristics as a conductive TI will be mentioned. The giant SHE and high electrical conductivity make BiSb a very promising candidate for spin Hall material in SOT-MRAM.

2.1 Spin-orbit interaction

SOI describes the phenomenon that the spin angular momentum $\boldsymbol{S}$ of electrons interacts with its orbital angular momentum $\boldsymbol{L}$. We now consider a case that an electron with charge $-e$ is moving around a nucleus with charge $+Ze$ in the laboratory rest frame. This frame can be transferred to the electron rest frame by the Lorentz transformation [1]:

$$\boldsymbol{E}'_{\parallel} = \boldsymbol{E}_{\parallel}, \qquad \boldsymbol{B}'_{\parallel} = \boldsymbol{B}_{\parallel},$$

$$\boldsymbol{E}'_{\perp} = \gamma(\boldsymbol{E}_{\perp} + \boldsymbol{v} \times \boldsymbol{B}), \qquad \boldsymbol{B}'_{\perp} = \gamma(\boldsymbol{B}_{\perp} - \frac{\boldsymbol{v}}{c^2} \times \boldsymbol{E}),$$

where $\gamma = \frac{1}{\sqrt{1-v^2/c^2}}$ is the Lorentz factor and c is the speed of light. The schematic of the laboratory rest frame and the electron rest frame are shown in Figure 2.1. In the electron rest frame, the orbiting nucleus generates a $\boldsymbol{B}$' field acting on the electron with the internal energy $E_{in} = -\mu B'$, where μ is the spin magnetic moment. In order to minimize the internal energy and reach the ground state, the spin of electron is aligned antiparallel to the $\boldsymbol{B}$' field. Thus, the spin angular momentum is "locked" to the orbital angular momentum, restricting the electrons with +1/2 and –1/2 spin to move to different direction.

The Hamiltonian that describes SOI is given as: $H_{\mathrm{SOI}} = \frac{Ze^2}{2m^2c^2r^3}\boldsymbol{L}\cdot\boldsymbol{S}$, where m is the electron mass, and r is the orbit radius. The concept of SOI brings various potential applications to our sight by manipulating the electron's momentum according to its spin or vice-verse. The SHE is one of the most famous and attractive phenomenon for spintronics device exploration.

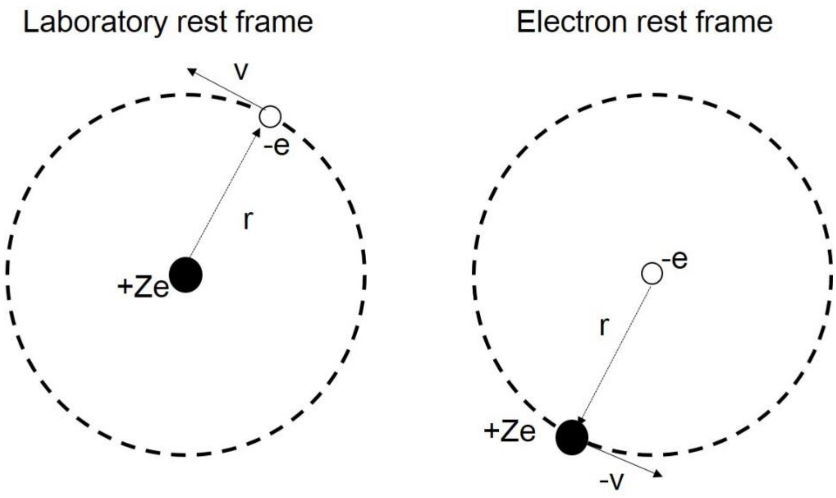

Figure 2.1 Schematic of SOI of an electron orbiting around the nucleus in laboratory rest frame (left) and electron rest frame (right).

2.2 Spin Hall effect

Before introduction of SHE, we would like to first introduce the concept of spin current [2]. In a spin-polarized current, up-spin and down-spin electrons move to the same direction. The net current is defined by the sum of electrons, while the net spin current is defined by the difference between up-spin and down-spin electrons. On the other hand, there is a situation that up-spin and down-spin electrons move to opposite direction. In this case, the net current is defined by the difference of up-spin and down-spin electrons, while the net spin current is defined by the sum. The most interesting situation is the pure spin current. There are up-spin and down-spin electrons of equal number flowing to opposite direction. Therefore, the net spin current is the total number of up-spin and down-spin current, while the net current is zero.

SHE is a phenomenon that a transverse pure spin current is generated by a charge current due to the SOI [3]. There are two main mechanisms for SHE: the intrinsic mechanism and the extrinsic mechanism. The extrinsic contribution is from the skew scattering and side jump [5-10]. In NM materials, the electrons shows a spin-dependent asymmetric scattering with up-spin and down-spin electrons accumulating to different side due to SOI. Similar to the atomic SOI, the movement of scattered electrons is affected by the interaction between the electron and the local potentials $\boldsymbol{V}(r)$. The SOI Hamiltonian describing this interaction is given by $H_{\mathrm{scat}} = \eta\sigma[\boldsymbol{k}\times \boldsymbol{V}(r)]$, where η is the modified SOI parameter, and σ is the spin polarization. The intrinsic contribution for SHE comes from the Berry phase of band structure. The Berry phase can be very large if there are Dirac points in the band structure [11-15]. Therefore, the intrinsic mechanism is considered as the main contribution for SHE in TIs with Dirac-like topological surface states [16, 17].

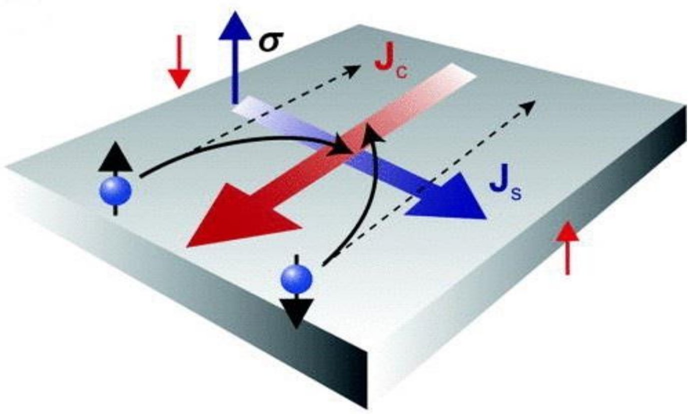

Figure 2.2 Schematic illustration of SHE [4]. Reprinted figure with permission from Ando K. et al., J. Appl. Phys. 109, 103913 (2011). Copyright (2022) by AIP

publishing.

Because of the SHE, when a charge current $\boldsymbol{J}_c$ flows in the spin Hall layer, a spin current $\boldsymbol{J}_s$ is generated perpendicular to the $\boldsymbol{J}_c$ direction as $\boldsymbol{J}_s \propto \boldsymbol{\sigma} \times \boldsymbol{J}_c$, where $\boldsymbol{\sigma}$ is the spin polarization. The conversion efficiency from charge current to spin current is represented by the spin Hall angle θ_{SH}, which is given by:

$$\theta_{SH} = \frac{2eJ_s}{\hbar J_c}.$$

The spin Hall angle is the most important parameter for the spin current source. Large spin Hall effect has been discovered in heavy metals like Pt [18, 20], Ta [21, 22], W [23, 24], and TIs such as BiSb [25, 26], Bi_2Se_3 [27, 28], Bi_2Te_3 [29, 30], and $(BiSb)_2Te_3$ [28, 30, 31]. Particularly, BiSb has the largest spin Hall angle among these materials.

2.3 Spin orbit torque

In NM/FM heterostructures, the spin current can exert a spin orbit torque acting on the FM layer, and drives magnetization switching [32]. The dynamics of magnetization can be described by the Landau-Lifshitz-Gilbert (LLG) equation [33]:

$$\frac{d\boldsymbol{m}}{dt} = -\gamma \boldsymbol{m} \times \boldsymbol{H}_{\text{eff}} + \alpha \boldsymbol{m} \times \frac{d\boldsymbol{m}}{dt} + \zeta_{\text{FL}}(\boldsymbol{\sigma} \times \boldsymbol{m}) + \zeta_{AD}(\boldsymbol{m} \times (\boldsymbol{\sigma} \times \boldsymbol{m}))$$

where γ is the gyromagnetic ratio, α is the Gilbert damping parameter, $\boldsymbol{H}_{\text{eff}}$ is the effective field, and $\boldsymbol{m}$ is the magnetization unit vector. The latter two terms, which represent the SOT, are separated to two parts [34]. The first part is the field-like torque associated to the Rashba-Edelstein effect [35], and the second part is the antidamping-like torque associated to SHE. ζ_{FL} and ζ_{AD} are field-like torque and antidamping-like torque coefficient, respectively. The direction of field-like torque and antidamping-like torque are illustrated in Figure 2.3. From the LLG equation, in SOT-MRAM with PMA, the spin-polarization of the pure spin current is perpendicular to the magnetization direction of the free magnetic layer, thus the spin torque is maximized and the magnetization can switch very fast (< ns) [36]. In TI/FM systems, SHE dominates the Rashba-Edelsten effect, making the antidamping-like torque becomes the major torque [25, 27, 31]. The antidampting-like torque is defined by $\boldsymbol{\tau}_{\mathrm{AD}} = -\boldsymbol{m} \times \boldsymbol{H}_{\mathrm{AD}}$, where $\boldsymbol{H}_{\mathrm{AD}}$ is the antidamping-like effective field given as $\boldsymbol{H}_{\mathrm{AD}} = -\frac{\hbar}{2eM_s t} J_s(\boldsymbol{\sigma}\times\boldsymbol{m})$. In this equation, M_s is the saturation magnetization and t is the thickness of FM layer. Based on this equation, the charge-to-spin conversion efficiency and spin Hall angle can be evaluated by measuring H_{AD} [28, 37].

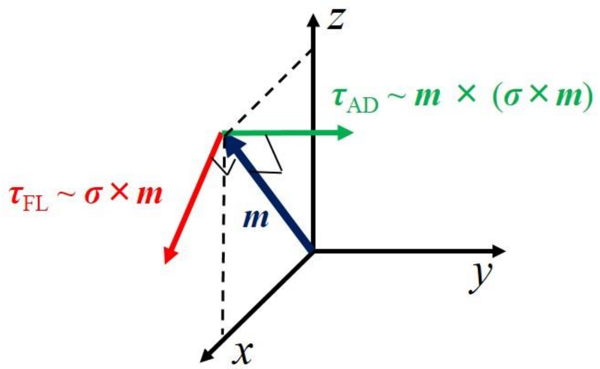

Figure 2.3 Schematic illustration of the directions of field-like torque (red) and antidamping-like torque (green)

2.4 Topological insulator

TI is a kind of quantum material with insulating bulk but conductive surface states. The concept of topology states is first introduced in 1980s [38] to explain the quantum Hall effect in metal-oxide-semiconductor field effect transistor [39]. However, the quantum Hall effect is difficult to come into application, because it can only be observed at ultralow temperature and high magnetic field. In 2005, the quantum SHE is proposed in materials with topological order [40], and its existence is predicted in a HgTe quantum well in 2006 [41]. The quantum spin Hall effect is originated from the spin-orbit interaction without relying on magnetic field and low temperature. Since this phenomenon is observed in experiments in 2007 [42], the exploration for applications of TI at room temperature comes into sight of researchers. The HgTe quantum well is a 2D TI with topological edge states. In 2009, the first 3D TI BiSb with the insulating bulk and 2D surface states was observed by angle resolved photoemission spectroscopy (ARPES) [12].

In TI, the band structure of bulk is similar to that of normal insulators. In contrast, there are conductive electronic states with Dirac-like dispersion on the edge/surface as shown in Figure 2.4(b) and 2.4(d) [41, 44]. The electrons on the edge/surface are under strong SOI with spin-momentum locking [13, 43]. In 2D TI, the electrons have only two direction to go, with up-spin and down-spin electrons moving to opposite direction as shown in Figure 2(a). The schematic illustration of electrons on surface states in 3D TI is shown in Figure 2(c). Dissipation is avoided in the spin current because back scattering is inhibited. Therefore, the TI has high potential to be applied in novel electronic devices, with the expectation to go beyond the Moore's Law.

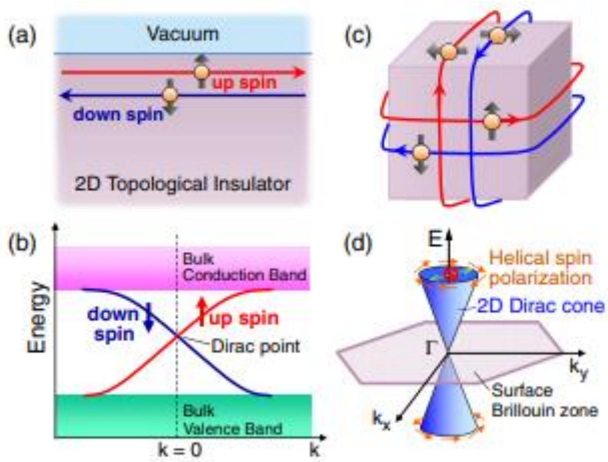

Figure 2.4 **(a)** Schematic of edges state in 2D TI. **(b)** Energy dispersion of the spin non-degenerate edge state of a 2D TI forming a 1D Dirac cone. **(c)** Schematic of 2D surface states in 3D TI. **(d)** Energy dispersion of the spin non-degenerate surface state of a 3D TI forming a 2D Dirac cone. Figure from [44]. © [2013] The Physical Society of Japan (J. Phys. Soc. Jpn. 82, 102001.)

One of the important applications of TI is as the spin Hall layer in SOT-MRAM thanks to its large spin Hall angle originated from strong SOI and Dirac-like dispersion [45, 46]. It has been reported that Bi_2Se_3 and $(BiSb)_2Te_3$ has large spin Hall angle of 3.5 and 2.5 at room temperature, respectively. While the spin Hall angles are at least one order of magnitude larger than that of that of W, which is the best heavy metal candidate, the limited surface density of states restricts the electrical conductivity σ of those TIs to the order of ~ $10^4\ \Omega^{-1}m^{-1}$ (for example, σ ~ $5.7\times10^4\ \Omega^{-1}m^{-1}$ for Bi_2Se_3 and $1.8\times10^4\ \Omega^{-1}m^{-1}$ for $(Bi_{0.07}Sb_{0.93})_2Te_3$). Since the spin Hall layer is in contact with the FM free layer, the low conductivity will lead to a large shunting current to FM layer with less than 10% of the current flowing in the TI. To reduce the unnecessary energy consumption, TI with both large spin Hall angle and high electrical conductivity is highly required.

2.5 A conductive topological insulator BiSb

Composed of group-V semimetals Bi and Sb, BiSb crystal has the same rhombohedral *A*7 structure as the two elements. It is known that there is a band gap when the concentration of Sb is between 7% and 22% [47, 49] as shown in Figure 2.5(a). BiSb becomes TI in this region with small bulk bandgap (~ 20 meV) [47, 49] and high bulk conductivity σ of 4 ~ 6.4 × $10^5\ \Omega^{-1}m^{-1}$ [50]. In thin films, the quantum size effect significantly increases the band gap of BiSb, so that the current flows mostly on the surface when the thickness reaches 10 nm [51]. Thanks to the multi-surface states, σ of BiSb thin films is as high as 2.5×10^5 $\Omega^{-1}m^{-1}$. Figure 2.5(c) summarized the room temperature conductivity of BiSb as a function of Sb concentration in BiSb thin films with different thickness.

On the other hand, from the ARPES mapping in Figure 2.5(b) [12], the surface states Dirac cones has been confirmed. This suggests the large SHE of BiSb. Previous results of our group show that BiSb has the spin Hall angle of 52 in epitaxial BiSb(012)/MnGa bilayers, which is the largest value among all materials so far [25]. Nevertheless, these works were done by molecular beam epitaxy (MBE), which is not utilized in MRAM manufacturing. Therefore, it is necessary to fabricate high quality BiSb thin films by sputtering deposition.

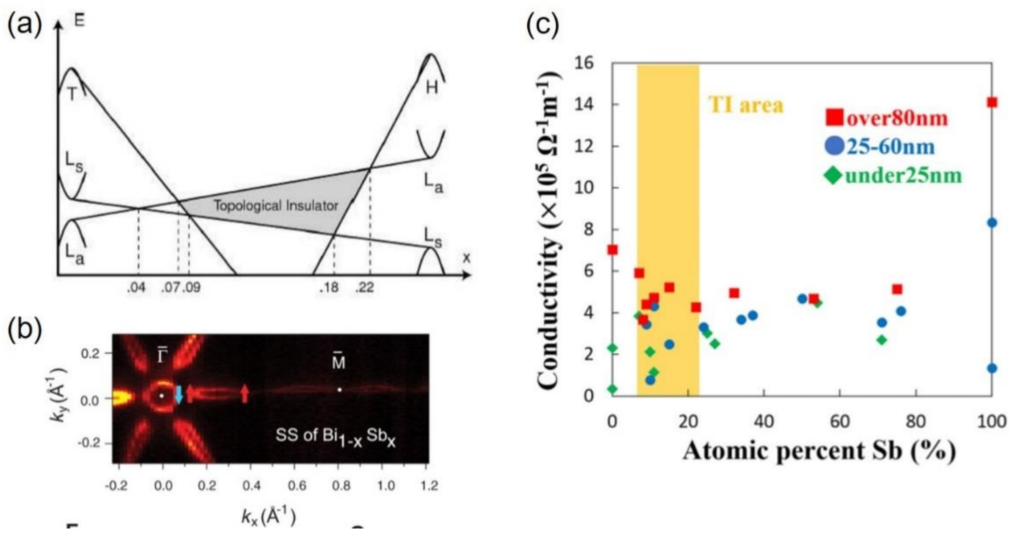

Figure 2.5 **(a)** Band structure of BiSb [48]. Reprinted figure with permission from Fu L. et al., Phys. Rev. B, 76, 045302 (2007). Copyright (2022) by the American Physical Society. **(b)** ARPES mapping for the surface states of BiSb [12]. Reprinted figure with permission from Hsieh D., et al. Science 323.5916, 919 (2009). Copyright (2022) by the

AAAS. **(c)** Room temperature conductivity of BiSb as a function of Sb concentration in BiSb thin films with different thickness [51]. Reprinted figure with permission from Ueda Y., et al. Appl. Phys. Lett. 110, 062401 (2017). Copyright (2022) by AIP publishing.

However, the spin Hall angle of BiSb heavily relies on the crystal quality and the ferromagnetic layer interface. The BiSb layer with spin Hall angle of 52, epitaxially grown by MBE, has high quality single crystal and optimized (012) orientation. It is known that the BiSb(012) surface have four Dirac cones: three Dirac cones due to time reversal symmetry at the $\overline{\Gamma}$, $\overline{X_1}$, $\overline{M}$ point, and one Dirac cone due to crystal symmetry near $\overline{X_2}$ point, as seen in Figure 2.6(b) [52]. Meanwhile, other surfaces, such as BiSb(001), has only one Dirac cone at the $\overline{\Gamma}$ point, as seen in Figure 2.6(a) [12]. Since Dirac points are hot spots for Berry curvature, the BiSb(012) surface has the largest spin Hall angle due to the strong intrinsic mechanism, while other orientation has smaller spin Hall angle. Therefore, optimizing the crystal orientation is important for obtaining large spin Hall angle of BiSb.

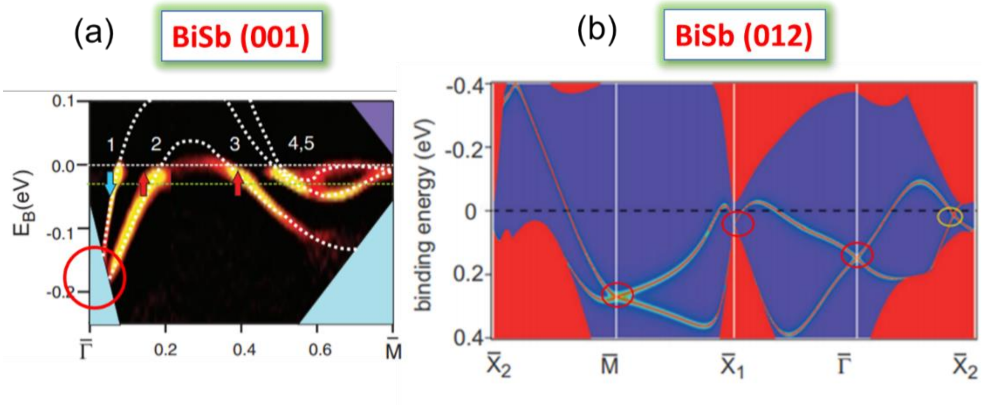

Figure 2.6 Topological surface states for (a) BiSb(001) [12] (Reprinted figure with permission from Hsieh D., et al. Science 323.5916, 919 (2009). Copyright (2022) by the AAAS) and (b) BiSb(012) [52] (Reprinted figure with permission from Zhu X., et al.

New J. Phys. 15, 103011 (2013). Copyright (2022) by IOP publishing). The circles indicate Dirac cones.

2.6 Summary

In this chapter, we briefly introduce the SOI, which is the origin of SHE in NM materials. The SOT associated with SHE can efficiently switch the magnetization in NM/FM system. We explain the method to evaluate the spin Hall angle from the antidamping-like torque in TI/FM system. Furthermore, TI BiSb is introduced as the best candidate for SOT-MRAM thanks to its large spin Hall angle and high electrical conductivity. These previous works are the foundation of our work that utilizes BiSb to realize the SOT magnetization switching in all-sputtered BiSb/FM heterostructures.

References

[1] Thomas L. The Motion of the Spinning Electron. Nature 117, 514 (1926).

[2] Ando Y. Spintronics technology and device development. Jpn. J. Appl. Phys. 54, 070101 (2015).

[3] Sinova J., et al. Spin hall effects. Rev. Mod. Phys. 87, 1213 (2015).

[4] Ando K., et al. Inverse spin-Hall effect induced by spin pumping in metallic system. J. Appl. Physics 109, 103913 (2011).

[5] Maekawa S., et al., eds. Spin current. Vol. 22. Oxford University Press, 2017.

[6] Stöhr J., et al. Magnetism. Solid-State Sciences. Springer, Berlin, Heidelberg 5 (2006).

[7] Kato Y., et al. Observation of the spin Hall effect in semiconductors. Science 306.5703, 1910 (2004).

[8] Dyakonov M., et al. Current-induced spin orientation of electrons in semiconductors. Phys. Lett. A 35, 459 (1971).

[9] Hirsch J. E. Spin hall effect. Phys. Rev. Lett. 83, 1834 (1999).

[10] Zhang S. Spin Hall effect in the presence of spin diffusion. Phys. Rev. Lett. 85, 393 (2000).

[11] Sinova J., et al. Surprises from the spin Hall effect. Phys. Today, 70, 38 (2017).

[12] Hsieh D., et al. Observation of unconventional quantum spin textures in topological insulators. Science 323.5916, 919 (2009).

[13] Hirahara T., et al. Topological metal at the surface of an ultrathin $Bi_{1-x}Sb_x$ alloy film. Phys. Rev. B 81, 165422 (2010).

[14] Kurebayashi H., et al. An antidamping spin–orbit torque originating from the Berry curvature. Nat. Nanotechnol. 9, 211 (2014).

[15] Gao T., et al. Intrinsic spin-orbit torque arising from the berry curvature in a metallic-magnet/Cu-oxide interface. Phys. Rev. Lett. 121, 017202 (2018).

[16] Qi X., et al. The quantum spin Hall effect and topological insulators. Phys. Today 63, 1 (2010).

[17] Moore J. The birth of topological insulators. Nature 464, 194 (2010).

[18] Miron I. M., et al. Perpendicular switching of a single ferromagnetic layer induced by in-plane current injection. Nature 476, 189 (2011).

[19] Liu L., et al. Current-induced switching of perpendicularly magnetized magnetic layers using spin torque from the spin Hall effect. Phys. Rev. Lett. 109, 096602 (2012).

[20] Yu G., et al. Switching of perpendicular magnetization by spin–orbit torques in the absence of external magnetic fields. Nat. Nanotechnol. 9, 548 (2014).

[21] Liu L., et al. Spin-torque switching with the giant spin Hall effect of tantalum. Science 336.6081, 555 (2012).

[22] Morota M., et al. Indication of intrinsic spin Hall effect in 4d and 5d transition metals. Phys. Rev. B 83, 174405 (2011).

[23] Hao Q., et al. Giant spin Hall effect and switching induced by spin-transfer torque in a W/$Co_{40}Fe_{40}B_{20}$/MgO structure with perpendicular magnetic anisotropy. Phys. Rev. Appl. 3, 034009 (2015).

[24] Cho S., et al. Large spin Hall magnetoresistance and its correlation to the spin-orbit torque in W/CoFeB/MgO structures. Sci. Rep. 5.1, 1 (2015).

[25] Khang N. H. D. et al, A conductive topological insulator with large spin Hall effect for ultralow power spin–orbit torque switching. Nat. Mater. 17, 808 (2018).

[26] Hai P. N. Spin Hall effect in topological insulators. J. Magn. Soc. Jpn. 44, 137 (2020).

[27] Mellnik A. R., et al. Spin-transfer torque generated by a topological insulator. Nature 511, 449 (2014).

[28] Wu H., et al. Spin-Orbit Torque Switching of a Nearly Compensated Ferrimagnet by Topological Surface States. Adv. Mater. 31, 1901681 (2019).

[29] Chen T., et al. Efficient Spin-Orbit Torque Switching with Nonepitaxial Chalcogenide Heterostructures. ACS Appl. Mater. Interfaces, 12, 7788 (2020).

[30] Wu H., et al. Room-Temperature Spin-Orbit Torque from Topological Surface States. Phys. Rev. Lett. 123, 207205 (2019).

[31] Fan Y., et al. Magnetization switching through giant spin–orbit torque in a magnetically doped topological insulator heterostructure. Nat. Mater. 13, 699 (2014).

[32] Manchon A., et al. Current-induced spin-orbit torques in ferromagnetic and

antiferromagnetic systems. Rev. Mod. Phys. 91, 035004 (2019).

[33] Gilbert T. A phenomenological theory of damping in ferromagnetic materials. IEEE Trans. Magn. 40, 3443 (2004).

[34] Haney P., et al. Current induced torques and interfacial spin-orbit coupling: Semiclassical modeling. Phys. Rev. B 87, 174411 (2013).

[35] Kim K, et al. Magnetization dynamics induced by in-plane currents in ultrathin magnetic nanostructures with Rashba spin-orbit coupling. Phys. Rev. B 85, 180404 (2012).

[36] Garello K., et al. Ultrafast magnetization switching by spin-orbit torques. Appl. Phys. Lett. 105, 212402 (2014).

[37] Khang N. H. D., et al. Spin–orbit torque as a method for field-free detection of in-plane magnetization switching. Appl. Phys. Lett. 117, 252402 (2020).

[38] Thouless D., et al. Quantized Hall conductance in a two-dimensional periodic potential. Phys. Rev. Lett. 49, 405 (1982).

[39] Klitzing K. V., et al. New method for high-accuracy determination of the fine-structure constant based on quantized Hall resistance. Phys. Rev. Lett. 45, 494 (1980).

[40] Kane C., et al. Quantum spin Hall effect in graphene. Phys. Rev. Lett. 95, 226801 (2005).

[41] Bernevig A., et al. Quantum spin Hall effect and topological phase transition in HgTe quantum wells. Science 314.5806, 1757 (2006).

[42] König M., et al. Quantum spin Hall insulator state in HgTe quantum wells. Science 318.5851, 766 (2007).

[43] Zhang H. et al. Topological insulators in Bi_2Se_3, Bi_2Te_3 and Sb_2Te_3 with a single Dirac cone on the surface. Nat. Phys. 5, 438 (2009).

[44] Ando Y. Topological insulator materials. J. Phys. Soc. Jpn. 82, 102001 (2013).

[45] Shao Q., et al. Room Temperature Highly Efficient Topological Insulator / Mo / CoFeB Spin-Orbit Torque Memory with Perpendicular Magnetic Anisotropy. 2018 IEEE International Electron Devices Meeting (IEDM), 36.3.1 (2018).

[46] Shao Q., et al. Roadmap of spin-orbit torques. IEEE Trans. Magn. 57, 800439 (2021).

[47] Lenoir B., et al. Transport properties of Bi-RICH Bi-Sb alloys. J. Phys. Chem. Solids 57, 89 (1996).

[48] Fu L. and Kane C.L. Topological insulators with inversion symmetry. Phys. Rev. B 76, 045302 (2007).

[49] Teo J. C. Y., et al. Surface states and topological invariants in three-dimensional topological insulators: Application to $Bi_{1-x}Sb_x$. Phys. Rev. B 78, 045426 (2008).

[50] Kitagawa H., et al. 22nd Int. Conf. on Thermoelectrics, 2003, p. 290.

[51] Ueda Y., et al. Epitaxial growth and characterization of $Bi_{1-x}Sb_x$ spin Hall thin films on GaAs(111)A substrates. Appl. Phys. Lett. 110, 062401 (2017).

[52] Zhu X., et al. Three Dirac points on the (110) surface of the topological insulator $Bi_{1-x}Sb_x$. New J. Phys. 15, 103011 (2013).

Chapter 3 Crystal growth and characterization of BiSb thin films by sputtering deposition on sapphire substrates

3.1 Introduction

As introduced in previous chapters, BiSb is expected to be the best candidate for the pure spin source in SOT-MRAM. Although the giant spin Hall effect has been observed in several topological insulators, BiSb is particularly promising because it shows both a giant spin Hall angle ($\theta_{SH} \sim 52$ for the BiSb(012) surface) [1] and high electrical conductivity (average $\sigma \sim 2.5 \times 10^5\ \Omega^{-1}\mathrm{m}^{-1}$) [2]. In previous works, SOT switching with ultralow current density and large critical interfacial Dzyaloshinskii-Moriya-Interaction were demonstrated in MnGa/BiSb bilayers [2], and giant unidirectional spin Hall magnetoresistance was observed in GaMnAs/BiSb bilayers [3]. However, topological insulator thin films, including BiSb, are usually deposited by MBE, which is not suitable for mass production of realistic spintronic devices. Thus, physical vapor deposition of high quality topological insulators is strongly required.

In this chapter, we report on the growth and characterization of BiSb thin films deposited on sapphire substrates by sputtering deposition with Ar and Kr plasma. By optimizing the growth conditions, we are able to obtain quasi-single-crystal BiSb(001) thin films with equivalent twin crystals. The conductivity of BiSb at the studied thicknesses exceeds $10^5\ \Omega^{-1}\mathrm{m}^{-1}$, reaching a maximum of $1.8 \times 10^5\ \Omega^{-1}\mathrm{m}^{-1}$ at 10 nm. From the temperature dependence of the electrical resistivity, we confirm the existence of metallic surface states, and demonstrate that the surface states dominate the conduction in 10 nm films. Our results demonstrate that it is possible to obtain sputtered BiSb thin films with quality approaching that of epitaxial BiSb grown by MBE.

3.2 Growth and characterization techniques

Magnetron sputtering deposition

Magnetron sputtering deposition is a physical vapor deposition method for thin films. In sputtering process, the atoms or molecules of material are ejected from a target by accelerated ions of sputtering gas. An electromagnetic field is applied near the cathode, and the sputtering gas is ionized into plasma. The ions in the plasma are accelerated by the electric field to impact the target, and the atoms or molecules are knocked out and deposited on the substrate. Figure 3.1 shows the working principle of sputtering deposition.

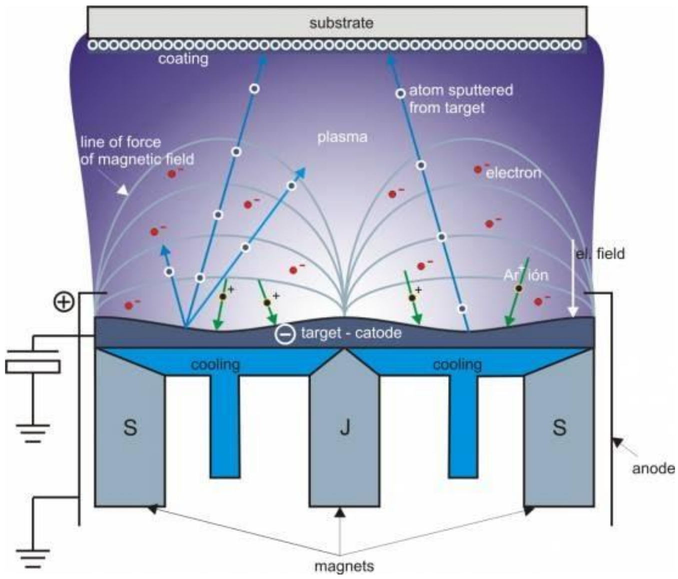

Figure 3.1 Working principle of magnetron sputtering. Source: Stanford Advanced Materials.

Sputtering deposition has several advantages over other deposition methods. Partial pressure of background gas and potential contaminants are minimized by evacuating the chamber into a high pressure of $10^{-7} \sim 10^{-8}$ Pa. In the electromagnetic field, sputtering gas is ionized into ions and secondary electrons. The secondary electrons are restricted in a circular cycloid near the cathode. The cycloid is long and the secondary electrons can help ionize more sputtering gas atoms. This realizes high deposition speed. The secondary electrons will finally move to the substrate with very low energy, making little change in the substrate temperature. Therefore, it has all-around high performance in quality, efficiency and reliability. These advantages make sputtering deposition the best method for thin film deposition for large wafers. It has been the most widely used technique for metal thin film deposition in HDD and electronics industry. For the mass production of MRAM, it is required to deposit the thin films on a large substrate for further device fabrication process of integrated circuits. Therefore, for mass production of SOT-MRAM it is necessary to investigate the possibility of high-quality BiSb deposition by sputtering.

X-ray diffraction spectroscopy

X-ray diffraction spectroscopy (XRD) is one of the most important and fundamental non-destructive technique for structure analysis of all types of materials: crystals, powders and fluids. In our work, we use it to analyze the crystallization of BiSb thin films. In XRD measurements, X-ray is irradiated into the crystal. With the diffraction and reflection by adjacent atomic layers, there will be a phase difference in the emergent X-ray. The distance between the adjacent atomic planes can be calculated through this phase difference, thereby the crystal orientation can be distinguished. The peaks of the spectrum follows the Bragg's law: $n\lambda = 2d\sin\theta$, where λ is the wave length of X-ray, θ is the incident angle, and d is the distance between different planes.

The schematic of x-ray measurements is illustrated in Figure 3.2(b). The main phase of a crystal can be acquired by θ-2θ scan. Furthermore, the in-plane texture can be analyzed by the azimuth angle φ – tilting angle χ scan.

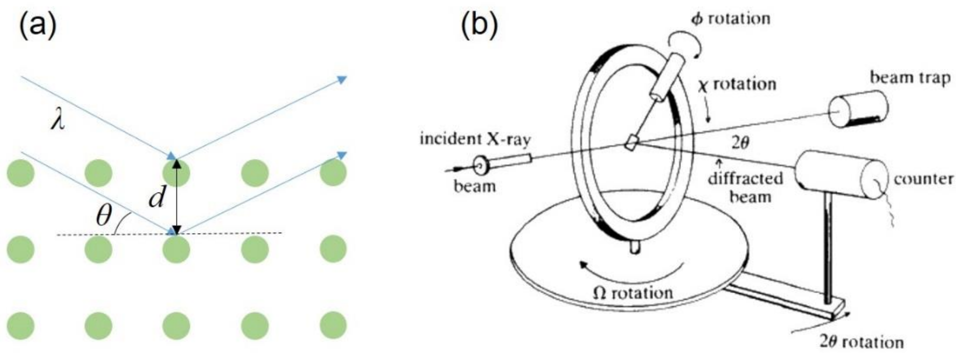

Figure 3.2 **(a)** Illustration of Bragg law. **(b)** XRD apparatus. Source: SERC at Carleton College.

3.3 BiSb thin Film growth and characterization

Sample growth

In the bulk TI region of $0.07 < x < 0.22$, $Bi_{1-x}Sb_x$ has a band gap smaller than 20 meV [4], high carrier mobility, μ, of $1.5–5 \times 10^3$ $cm^2V^{-1}s^{-1}$ [4, 5], and high bulk conductivity ($4–6.4 \times 10^5$ $\Omega^{-1}m^{-1}$) [6] comparing with those of Bi_2Se_3 and Bi_2Te_3 (~ 10^4 $\Omega^{-1}m^{-1}$). It is reported that in TI region, the bulk band gap of BiSb is largest when the concentration of Sb is 15% [5]. Because the electrons in the valence band can be excited to the conduction band at room temperature, it is possible that the current can flow in the bulk. Larger bulk band gap can suppress the excitation of electrons, making the bulk conductance decrease and more current flows on the surface. The surface with Dirac cone structure can generate large SHE, thereby large spin Hall angle can be expected. This fact has been confirmed recently in a recent work by Ichimura et al. [7]. Therefore, we choose single sputtering target $Bi_{0.85}Sb_{0.15}$ in this work.

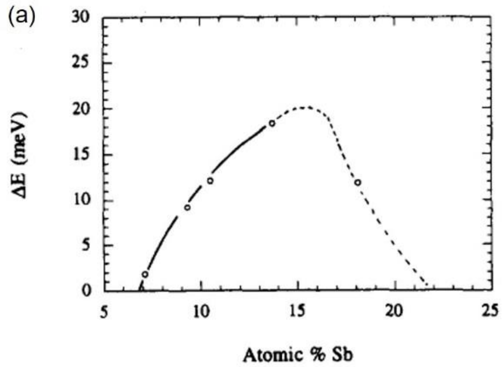

Blanked before original source published.

Figure 3.3 Sb concentration dependence of **(a)** Band gap [6] and **(b)** effective spin Hall angle in $(Co/Tb)_3$/Pt/BiSb heterostructures [7].

We deposit BiSb thin films with various thicknesses on sapphire C-plane (0001) substrates by radio-frequency magnetron sputtering. Since the lattice constants are a = 4.53 Å, c = 11.8 Å for $Bi_{0.85}Sb_{0.15}$ and a = 4.76 Å, c = 13.0 Å for sapphire, there is a lattice mismatch of -5.2% between BiSb and the sapphire substrates. Before deposition, the sapphire substrates were chemically cleaned in a hot solution mixture of phosphoric and sulfuric acid at 160°C [8] for 15 minutes. The substrates were then thermally cleaned by heating in the deposition chamber at 850°C [9] for 30 minute. Table 3.1 shows the list of samples and their deposition condition used in this work. There are two series of samples: samples A1-1 to A2-3 were deposited using Ar plasma, and samples K1-1 to K2-3 were deposited using Kr plasma. The substrate temperature was either kept constant (one-step) or changed (two-step) during the deposition, as discussed below. The Ar/Kr gas pressure was kept at 0.2 Pa, and the typical sputtering power was 0.9 W/cm^2. For samples deposited by the one-step method, the best substrate temperature varies according to the thickness of BiSb film. For 10 nm-thick BiSb films (samples A1-1 and

K1-1), we found that the substrate temperature T_S = 50 ℃ was optimal, as for T_S higher than 100°C, the films became nonconductive. On the other hand, the best T_S for films over 14 nm was 150°C (samples A1-2 to A1-4, K1-2, and K1-2). To further improve the crystal quality, we employed a two-step technique for thick films (samples A2-1 to A2-3 and samples K2-1 to K2-3). First, we deposited a BiSb layer thinner than 10 nm at 50°C. Then, we increased T_S to 150°C, and annealed the layer for 10 minutes. Finally, we deposited the rest at 150°C. We found that this two-step technique can improve the crystal quality and the electrical conductivity of BiSb thin films thicker than 10 nm.

Sample	Substrate temperature	Thickness (nm)	Gas
A1-1	50 ℃	10	Ar
A1-2	150 ℃	14	
A1-3	150 ℃	28	
A1-4	150 ℃	40	
A2-1	50 ℃ → 150 ℃	14	
A2-2	50 ℃ → 150 ℃	24	
A2-3	50 ℃ → 150 ℃	40	
K1-1	50 ℃	10	Kr
K1-2	150 ℃	30	
K1-3	150 ℃	50	
K2-1	50 ℃ → 150 ℃	17	
K2-2	50 ℃ → 150 ℃	25	
K2-3	50 ℃ → 150 ℃	43	

Table 3.1 Samples studied in this chapter

Crystal structure analysis

$Bi_{1-x}Sb_x$ has a rhombohedral crystal structure (Figure 3.4), which is similar to other topological insulators, such as Bi_2Se_3 and Bi_2Te_3. As introduced in previous chapters, the spin Hall angle of BiSb strongly relies on its crystal orientation. Therefore, it is important to investigate how BiSb is crystallized at different temperature. Here we use XRD and TEM to characterize the crystal orientation (the TEM technique will be introduced in Chapter 6).

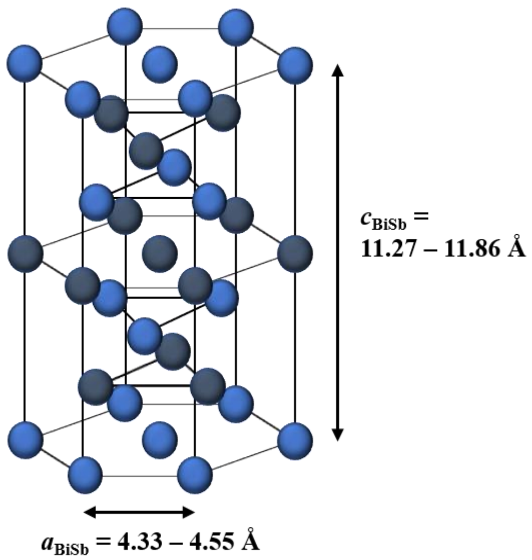

Figure 3.4 Crystal structure of BiSb

Figure 3.5(a)-3.5(d) show the $\theta - 2\theta$ X-ray diffraction (XRD) spectra of BiSb thin films deposited in various conditions. Figure 3.5(a) shows the XRD spectra of samples A1-1 to A1-4, deposited by Ar plasma in one-step. The patterns show strong BiSb(003), (006) and (009) peaks, indicating the dominant BiSb(001) phase. At 10 nm, there is no other phase than BiSb(001), demonstrating that it is possible to obtain a single-phase BiSb thin film by sputtering deposition. As the thickness increases, extra phases such as BiSb(012) and BiSb(014) start to appear. Meanwhile, the two-step deposition can significantly suppress these extra phases, as can be seen in Figure 3.5(b) for samples A2-1 to A2-3. Indeed, the BiSb(001) single phase was observed up to at least 24 nm by the two-step deposition. For samples deposited by Kr plasma, the BiSb(001) single phase was observed even by one-step deposition up to 50 nm, as shown in Figure 3.5(c). However, a weak BiSb(014) phase exists for thick samples deposited by Kr plasma in two-step, as shown in Figure 3.5(d). The surface morphology observed by atomic force microscopy (AFM) shows that the 10 nm thick BiSb films have smoother surfaces than thicker films. The roughness of 10 nm-thick BiSb thin films is about 0.9 nm for sample A1-1, and about 0.8 nm for sample K1-1, as shown in Figure 3.6. However, the surface smoothness deteriorated rapidly as the thickness increased from 10 nm, which is consistent with the emergence of other phases as revealed by the XRD spectra.

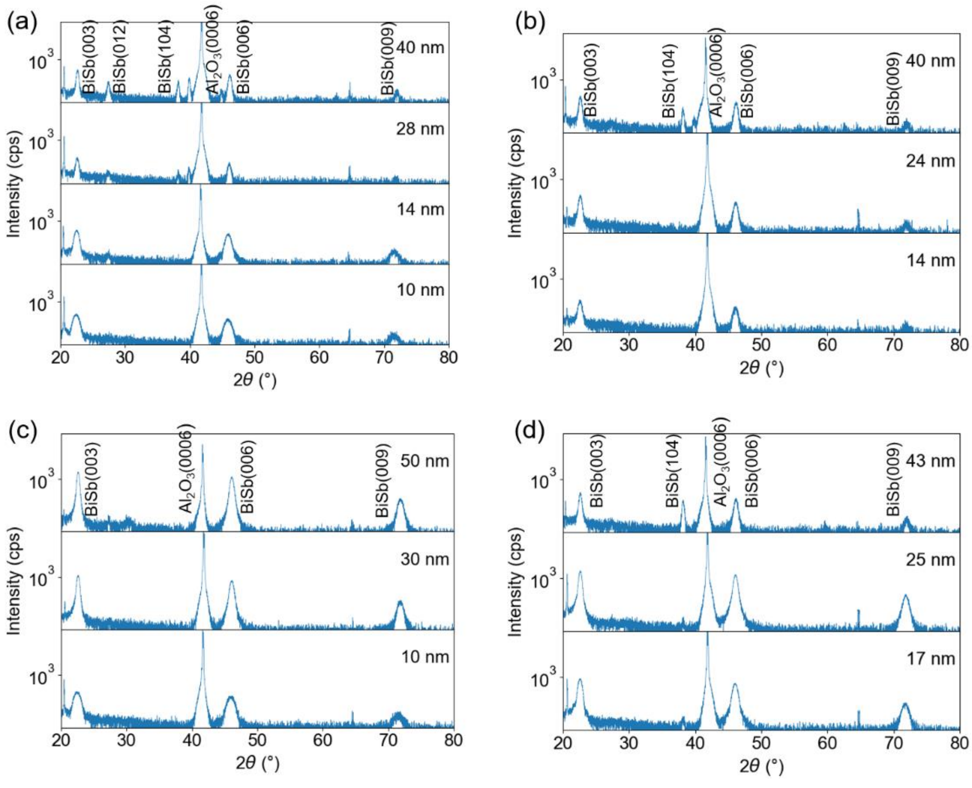

Figure 3.5 XRD $\theta-2\theta$ spectra of BiSb films on sapphire substrates, deposited by **(a)** Ar plasma in one-step, **(b)** Ar plasma in two-step, **(c)** Kr plasma in one-step, **(d)** Kr plasma in two-step.

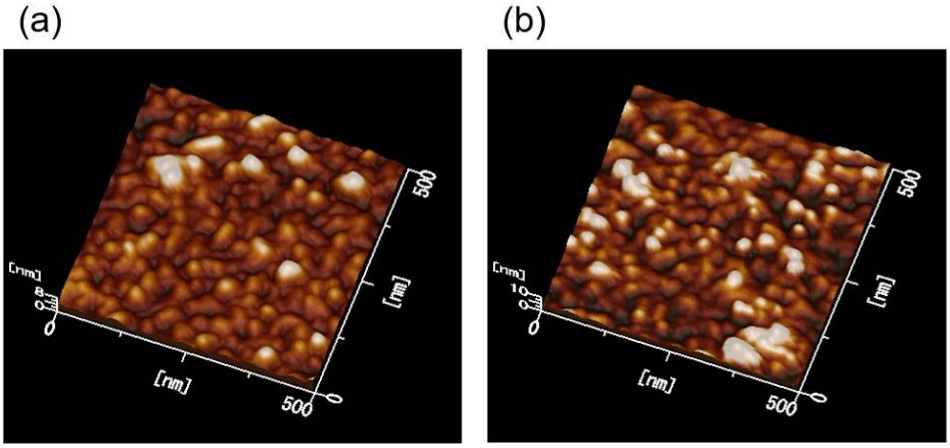

Figure 3.6 Surface morphology by AFM of 10 nm BiSb by **(a)** Ar and **(b)** Kr plasma.

Next, we performed the XRD $\chi-\varphi$ scan [10] to investigate the in-plane texture of the 10 nm-thick samples A1-1 and K1-1. The θ angle was set at 13.6° for the (012) plane. Figure 3.7(a) and 3.7(b) show the polar mapping for χ = 0-90° and φ = 0-360° scan of samples A1-1 and K1-1, respectively. The polar maps show 6 strong peaks located at χ = 55°. Considering the epitaxial single crystal BiSb(001) has 3 distinct peaks at χ = 55° separated by the azimuth angle of 120° (Figure 3.7(c)), Figure 3.7(a) and 3.7(b) indicate that there are equivalent twin crystals in samples A1-1 and K1-1 [11, 12]. However, there is no other plane in the polar maps besides BiSb(012), indicating the high crystal ordering of sputtered BiSb films despite the large lattice mismatch of -5.2% between the BiSb films and the sapphire substrates.

We further characterize the crystal structure at the interface between BiSb and the sapphire substrates by using high-resolution TEM. Figure 3.8 shows a TEM image of a BiSb film deposited on sapphire by Ar plasma, magnified near the interface. We can see that the first 2 nm BiSb has some crystal disorder, which absorbs the lattice mismatch with the sapphire substrate. When the thickness exceeds 2 nm, the crystal ordering improves rapidly, and a quasi-single-crystal BiSb film can be obtained. These results show the robustness of BiSb against lattice mismatch.

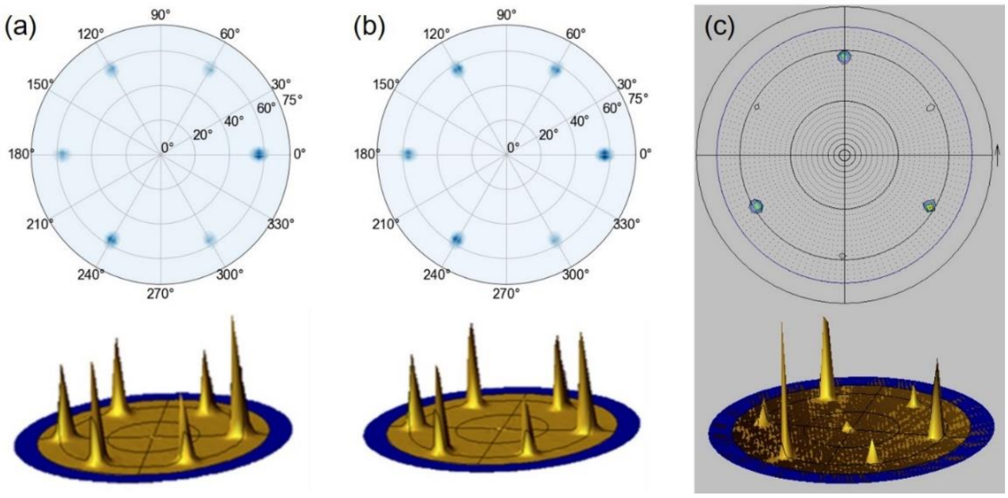

Figure 3.7 XRD $\chi - \varphi$ polar mapping of the 10 nm-thick BiSb films deposited by **(a)** Ar, **(b)** Kr plasma in one-step, and **(c)** MBE, respectively.

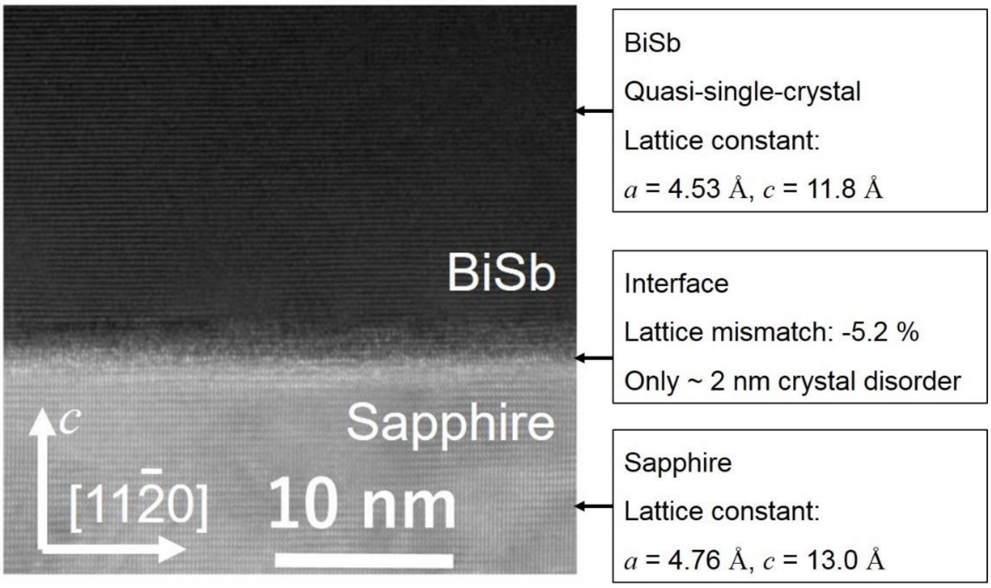

Figure 3.8 TEM image near the interface of BiSb (001) / sapphire C-plane (0001) substrate.

3.4 Electrical measurements

Hall bar device process for electrical measurements

For TI – FM heterostructures in SOT-MRAM, the high conductivity of TI is important to reduce the shunting current to the metallic FM layer. Thus, it is necessary to demonstrate highly conductive BiSb by sputtering deposition for future integration in spintronic devices. Furthermore, it is necessary to confirm the surface states in sputtered BiSb, which is important for large spin Hall angle. Because BiSb has metallic surfaces while the bulk performs like conventional semiconductors, the surface contribution can be distinguished by measuring the temperature dependence of conductivity, which shows different characteristics in surface and bulk states. We performed conductivity measurements using a 5-terminal Hall bar device in Figure 3.10. The process is as follows:

(1) Positive photoresist OFPR mask is formed on the surface of BiSb.

(2) Photoresist outside of the Hall bar is removed by photolithography and development (developer solution: NMD3).

(3) BiSb outside of the Hall bar is milled by Ar+ ion milling.

(4) Photoresist on the Hall bar is removed (solution: Stripper 104).

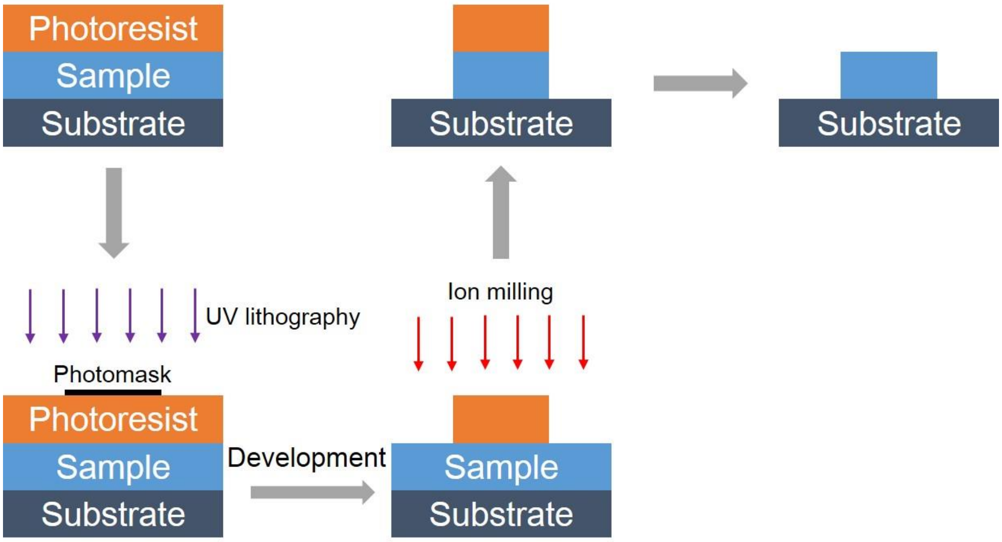

Figure 3.9 Device fabrication process

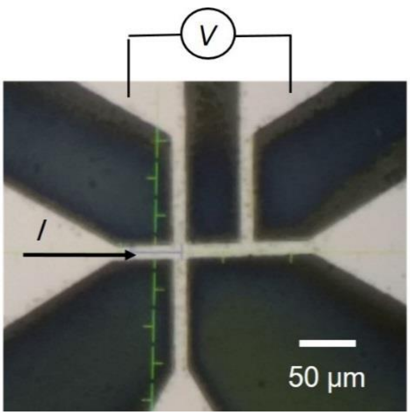

Figure 3.10 Optical image of a Hall bar with the electrical measurement set-up.

Electrical measurements results

Figure 3.11 shows the electrical conductivity, σ, of the BiSb thin films as a function of the film thickness, measured at 300 K. Two distinct features are observed. First, σ of the two-step samples is slightly higher than that of the one-step samples. Second, the thin samples have higher conductivity than that of the thick samples. The latter cannot be simply explained by the single BiSb(001) phase in the thin samples and the existence of multi phases in the thick samples. For example, the Kr one-step samples have nearly the same σ as with the Ar one-step samples, although the Kr one-step samples have a single phase of BiSb(001) up to 50 nm, while the Ar one-step samples have a single phase of BiSb(001) at 10 nm, two phases of BiSb(001) and (012) at 14 nm and 28 nm, and three phases of BiSb(001), (012), (104) at 40 nm. Instead, this feature can be explained by the existence of the topological surface states. The conductivity of a topological insulator is given by $\sigma = \sigma_S t_S / t + \sigma_B$, where σ_S and σ_B are the conductivity of the surface states and bulk states, and t_S and t are the thickness of the surface and the whole film, respectively. When the bulk conduction is dominant (i.e. $t >> t_S$), σ approaches σ_B. However, when t is reduced, the contribution of surface conduction becomes much more important, and σ becomes larger than σ_B, which explains the increasing σ at reduced thicknesses. We note that the even for the thick BiSb films, σ is still larger than 1×10^5 $\Omega^{-1}m^{-1}$. The highest σ of 1.8×10^5 $\Omega^{-1}m^{-1}$ is obtained for the 10 nm-thick Ar1-1 and Kr1-1 samples, which is close to that of high quality MBE-grown 10 nm-thick BiSb films on GaAs(111)A substrates (2.5×10^5 $\Omega^{-1}m^{-1}$), demonstrating that it is possible to obtain reasonably conductive and high quality BiSb thin films by sputtering deposition. Note that while sputtering deposition of another topological insulator, $Bi_{1-x}Se_x$, has been attempted, the crystal quality is much poorer than the MBE-grown Bi_2Se_3, and the conductivity of $Bi_{1-x}Se_x$ is reduced to about $7.8\times10^3\ \Omega^{-1}m^{-1}$ [13] from that of epitaxial Bi_2Se_3 ($\sim5\times10^4\ \Omega^{-1}m^{-1}$) [14]. In contrast, the conductivity of sputtered 10 nm-thick BiSb is not much different from that of MBE-grown 10 nm-thick BiSb.

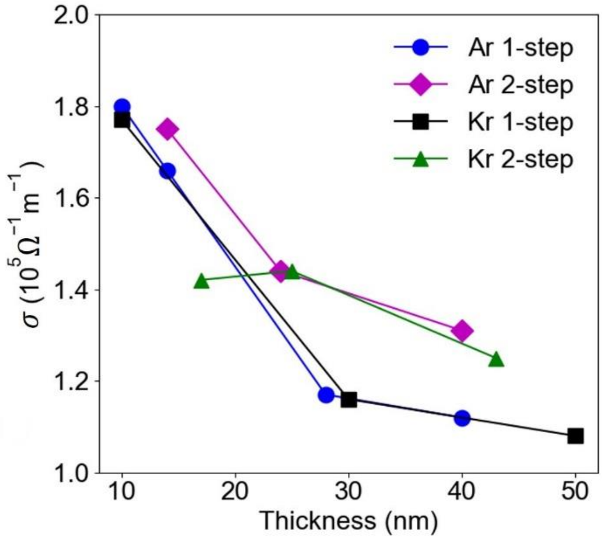

Figure 3.11 Electrical conductivity at 300 K of BiSb thin films with different thicknesses.

Another distinct feature of BiSb from other well-known V-VI topological insulators such as Bi_2Se_3, Bi_2Te_3 or Sb_2Te_3, is that its bulk is always an intrinsic semiconductor with the Femi level in the band gap. This is because Bi and Sb are in the same V-group, thus deviation of the composition or existence of anti-site defects does not result in any donors / acceptors that would generate free carriers and shift the Fermi level to the conduction band (as in the case of Bi_2Se_3 or Bi_2Te_3 due to anti-site Se/Te) or to the valence band (as in the case of Bi_2Te_3 or Sb_2Te_3 due to anti-site Bi/Sb). This intrinsic semiconducting behavior of the bulk states has been confirmed in MBE-grown BiSb films on GaAs(111)A substrates [2]. Thus, the temperature dependence of the bulk conductivity is given by

$\sigma_{\mathrm{B}} = \sigma_{\mathrm{B0}} \exp\left(-\frac{E_{\mathrm{g}}}{2k_{\mathrm{B}}T}\right)$, where E_{g} is the effective band gap, and T is the temperature. Therefore, the total conductivity can be described by [15]

$$\sigma = \frac{\sigma_{\mathrm{Sh}}}{t} + \sigma_{\mathrm{B}} = \frac{\sigma_{\mathrm{Sh}}}{t} + \sigma_{\mathrm{B0}} \cdot \exp\left(-\frac{E_{\mathrm{g}}}{2k_{\mathrm{B}}T}\right), \qquad (3.1)$$

where $\sigma_{\mathrm{Sh}} = \sigma_{\mathrm{S}} t_{\mathrm{S}}$ is the surface sheet conductance. Next, we measured the temperature dependence of resistivity in order to further demonstrate the existence of the surface states and estimate the effective band gap. Figure 3.12(a)-3.12(d) show the temperature-dependence of the electrical resistivity normalized by its value at 300 K (ρ/ρ_{RT}) for Ar one-step, Ar two-step, Kr one-step, and Kr two-step samples, respectively. For thick samples, there are parallel conduction on the surface and in the bulk due to thermally excited intrinsic carriers at room temperature. With the temperature decreasing, the bulk conduction is suppressed, and the surface conduction becomes overwhelmingly dominant, explaining the plateaus of resistivity below 100 K observed for thick samples in Figure 3.12(a)-3.12(d). The dashed lines in Figure 3.12(a)-3.12(d) are fits to the experimental data using Equation (3.1). For thin samples, the surface conduction dominates even at room temperature, thus the resistivity is nearly temperature-independent, confirming the metallic nature of the surface states [15]. These behaviors are similar to those of high quality MBE-grown BiSb thin films.

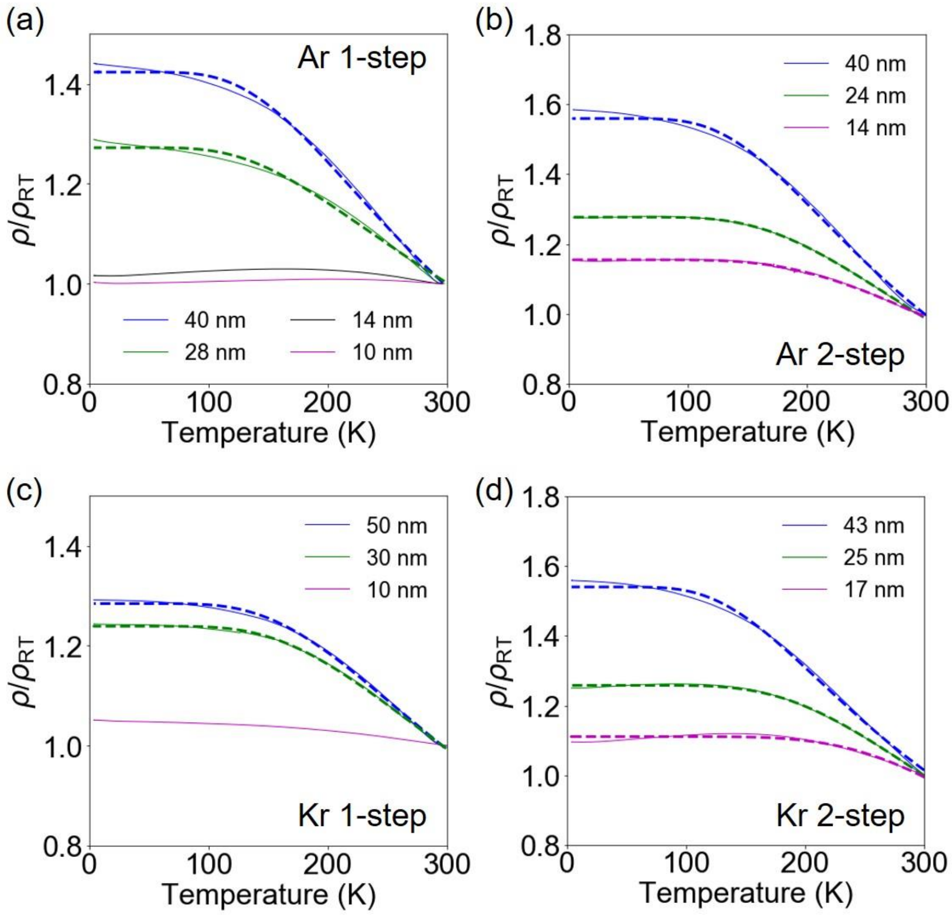

Figure 3.12 Temperature dependence of normalized resistivity ρ/ρ_{RT} of BiSb films deposited by **(a)** Ar plasma in one-step, **(b)** Ar plasma in two-step, **(c)** Kr plasma in one-step, and **(d)** Kr plasma in two-step. The dash lines are fitting curves by $\sigma = \sigma_{\mathrm{Sh}}/t + \sigma_{\mathrm{B0}} \exp\left(-\frac{E_{\mathrm{g}}}{2k_{\mathrm{B}}T}\right)$.

From fitting Equation (3.1) to the experimental data of thick samples, we can evaluate the contribution of the surface states to the total conductivity $\Gamma = \frac{\sigma_{\mathrm{Sh}}}{t}/(\frac{\sigma_{\mathrm{Sh}}}{t} + \sigma_{\mathrm{B}})$. From equation 3.1, we can obtain

$$\frac{\rho}{\rho_{\mathrm{RT}}} = \frac{\sigma_{\mathrm{RT}}}{\sigma} = \frac{\sigma_{\mathrm{RT}}}{\sigma_{\mathrm{Sh}}/t + \sigma_{\mathrm{B0}} \cdot \exp(-E_{\mathrm{g}}/2k_{\mathrm{B}}T)} = \frac{1}{a + b \cdot \exp\,(-c/T)},$$

in which the normalized fitting parameters are

$$a = \frac{\sigma_{Sh}}{\sigma_{RT} \cdot t},\ \ b = \frac{\sigma_{\mathrm{B0}}}{\sigma_{\mathrm{RT}}},\ \ c = \frac{E_g}{2k_B}.$$

Therefore, the surface contribution is nothing other than a, and the bulk conductivity at room temperature is given by

$$\sigma_{\mathrm{B}} = \ \sigma_{\mathrm{B0}} \cdot \exp\left(-\frac{E_{\mathrm{g}}}{2k_{\mathrm{B}}T}\right) = \sigma_{\mathrm{RT}} b * \exp\left(-c/T\right).$$

Experimental data			Fitting results		
Sample	t (nm)	σ_{RT} ($10^5\Omega^{-1}\mathrm{m}^{-1}$)	σ_{Sh}/t ($10^5\Omega^{-1}\mathrm{m}^{-1}$)	σ_{B} ($10^5\Omega^{-1}\mathrm{m}^{-1}$)	Γ (%)
A1-3	28	1.17	0.92	0.25	79
A1-4	40	1.12	0.79	0.34	70
A2-1	14	1.75	1.52	0.25	87
A2-2	24	1.44	1.13	0.33	78
A2-3	40	1.31	0.84	0.47	64
K1-2	30	1.16	0.94	0.23	81
K1-3	50	1.08	0.84	0.25	78
K2-1	17	1.42	1.28	0.15	90
K2-2	25	1.44	1.14	0.3	79
K2-3	43	1.25	0.81	0.42	65

Table 3.1 Fitting results for the surface conductivity, the bulk conductivity, and the contribution of the surface states to the total conductivity for samples thicker than 10 nm.

Table 3.1 shows the fitting results for the surface conductivity, the bulk conductivity, and the contribution of the surface states to the total conductivity for samples thicker than 10 nm. The bulk conductivity is only about 2 ~ 4×10^4 $\Omega^{-1}\mathrm{m}^{-1}$, which is especially small in thinner samples, and the surfaces conductivity dominates the total conductivity.

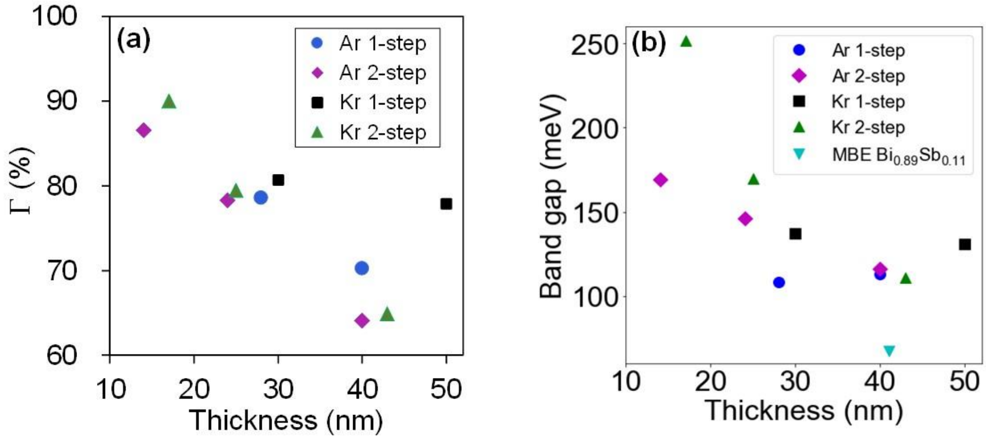

Figure 3.13 **(a)** Surface state contribution to the total conductivity Γ at room temperature, and **(b)** effective band gap of sputtered BiSb thin films thicker than 10 nm. For reference, the effective band gap of an MBE-grown BiSb film is also shown.

Figure 3.13(a) shows Γ at room temperature for samples thicker than 10 nm. One can see that even for very thick samples of 40-50 nm, Γ is larger than 60%. Γ rapidly increases with decreasing the thickness, and reaches nearly 90% for samples thinner than 20 nm. This indicates that the surface states dominate electrical conduction in BiSb. Furthermore, we can estimate the effective band gaps, which are plotted in Figure 3.13(b). For comparison, we also show the band gap of a 41 nm-thick MBE-grown $Bi_{0.89}Sb_{0.11}$ thin film. The band gaps include the intrinsic band gap (~ 20 meV) and the extrinsic band gap due to the quantum confinement effect. In general, because of the quantum confinement effect in BiSb, the effective band gap is much larger than the intrinsic value [2]. The data in Figure 3.13 shows the overall trend that the effective band gap increases with decreasing the thickness, which agrees with the existence of the extrinsic band gap due to quantum confinement. The effective band gaps of sputtered BiSb films are twice as large as that of MBE-grown BiSb, and depend on the sputtering condition. The origins of this enhancement of the effective band gap of sputtered BiSb are not clear, but may be due to the lowering in the effective electron mass that enhances the extrinsic band gap, or extra biaxial tensile strain on the films during the sputtering process that can enlarge the intrinsic band gap [16].

3.5 Conclusion

In conclusion, we have characterized BiSb thin films deposited on sapphire substrates by sputtering deposition. We show that it is possible to deposit high quality quasi-single-crystal BiSb thin films by sputtering deposition with quality approaching that of MBE-grown epitaxial thin films. We confirmed the existence of surface states from the thickness-dependence and temperature-dependence of the electrical conductivity/resistivity. Our results are promising for future integration of BiSb in SOT-based spintronic devices, such as SOT-MRAM or spin Hall oscillators.

References

[1] Khang N. H. D. et al, A conductive topological insulator with large spin Hall effect for ultralow power spin–orbit torque switching. Nat. Mater. 17, 808 (2018).

[2] Ueda Y., et al. Epitaxial growth and characterization of $Bi_{1-x}Sb_x$ spin Hall thin films on GaAs(111)A substrates. Appl. Phys. Lett. 110, 062401 (2017).

[3] Khang N. H. D., et al. Giant unidirectional spin Hall magnetoresistance in topological insulator–ferromagnetic semiconductor heterostructures. J. Appl. Phys. 126, 233903 (2019).

[4] Teo J. C. Y., et al. Surface states and topological invariants in three-dimensional topological insulators: Application to $Bi_{1-x}Sb_x$. Phys. Rev. B 78, 045426 (2008).

[5] Lenoir B., et al. Transport properties of Bi-RICH Bi-Sb alloys. J. Phys. Chem. Solids

57, 89 (1996).

[6] Kitagawa H., et al. 22nd Int. Conf. on Thermoelectrics, 2003, p. 290.

[7] Ichimura M, et al. BiSb トポロジカル絶縁体のスピンホール効果の Sb 組成比依存性. 12p-S302-5, JSAP autumn 2021.

[8] Chen Y., et al. Plasma assisted molecular beam epitaxy of ZnO on c-plane sapphire: Growth and characterization. J. Appl. Phys. 84, 3912 (1998).

[9] Johnson M. A. L., et al. MBE growth and properties of ZnO on sapphire and SiC substrates. J. Electron. Mater. 25, 855 (1996).

[10] Jeffrey C. A., et al. X-ray characterization of as-deposited, epitaxial films of Bi(012) on Au(111). Surf. Sci. 600, 95 (2006).

[11] Nagao T., et al. Nanofilm Allotrope and Phase Transformation of Ultrathin Bi Film on Si(111) − 7×7. Phys. Rev. Lett. 93, 105501 (2004).

[12] Yao K., et al. Influence of crystal orientation and surface termination on the growth of BiSb thin films on GaAs substrates. J. Cryst. Growth 511, 99 (2019).

[13] Mahendra DC, et al. Room-temperature high spin–orbit torque due to quantum confinement in sputtered $Bi_xSe_{(1-x)}$ films. Nat. Mater. 17, 800 (2018).

[14] Mellnik A. R., et al. Spin-transfer torque generated by a topological insulator. Nature 511, 449 (2014).

[15] Xiao S., et al. Bi(111) thin film with insulating interior but metallic surfaces. Phys. Rev. Lett. 109, 166805 (2012).

[16] Yu W., et al. Strain induced quantum spin Hall insulator in monolayer β-BiSb from first-principles study. RSC Adv. 7, 27816 (2017).

Chapter 4 Ultrahigh efficient spin-orbit torque magnetization switching in all-sputtered topological insulator – ferromagnet multilayers

4.1 Introduction

In chapter 3, high quality single layer BiSb thin films with high electrical conductivity (1.8×10^5 Ω^{-1} m^{-1}) were successfully deposited on sapphire substrate by sputtering deposition. We demonstrated that surface states are dominant in 10 nm BiSb thin films, even by sputtering deposition. Thus, we can expect that the high electrical conductivity and high surface contribution can be obtained on other substrates or on top of MTJ. On the other hand, the supremacy of BiSb by MBE has been demonstrated in previous works. The conductivity of MBE-grown BiSb thin films is as high as 2.5×10^5 Ω^{-1} m^{-1} [1]. Furthermore, a giant spin Hall effect with $\theta_{SH} \sim 52$ has been observed in BiSb(012) thin films in junctions with MnGa grown on GaAs substrates [2]. These advantages make BiSb become a better candidate for SOT-MRAM compared with heavy metals like Pt, Ta and W, and other TIs like Bi_2Se_3 and $(Bi_{0.07}Sb_{0.93})_2Te_3$. Nevertheless, following works on sputtered polycrystalline BiSb yields a maximum θ_{SH} of only 1.2 [3], or even no SHE [4]. Therefore, it is very important to demonstrate the three requirements: (1) a large spin Hall angle, (2) large electrical conductivity σ of order of 10^5 Ω^{-1} m^{-1}, and (3) can be deposited using industry-friendly techniques, for sputtered BiSb for any realistic applications to SOT-based spintronic devices.

In this chapter, we demonstrate ultrahigh efficient SOT magnetization switching in all-sputtered BiSb – (Co/Pt) multilayers with large PMA. We show that the sputtered BiSb has a large spin Hall angle of $\theta_{SH} = 10.7$ and high electrical conductivity of $\sigma = 1.5 \times 10^5$

$\Omega^{-1}m^{-1}$, thus satisfying all the three requirements for SOT-MRAM implementation. Despite the large PMA field of 5.2 kOe of the (Co/Pt) multilayers, we achieve robust SOT magnetization at a low current density of 1.5×10^{6} Acm^{-2}. Our results demonstrate the potential of BiSb topological insulator for mass production of ultralow power SOT-MRAM and other SOT-based spintronic devices. Compared with other works on TI / magnetic layers with small magnetization, the large magnetization of the (Co/Pt) multilayers in this work is compatible to realistic MRAM.

4.2 Sample growth and device fabrication

Sample growth

The main concerns for fabrication of high-quality TI - perpendicularly magnetized FM multilayers include the selection of materials for the FM layer, and the deposition sequence for BiSb and FM layers. Considering the large surface roughness of TIs (~ 5 Angstrom for BiSb) and atomic inter diffusion during annealing process of the MTJ, it is not realistic to deposit the MTJ on top of the TI layer. Instead, the MTJ should be deposited and fabricated first, then the TI layer should be deposited on top of the free magnetic layer at the last step. Furthermore, to achieve high enough thermal stability, the free magnetic layer should be composed of ferromagnetic multilayers with high PMA that couple ferromagnetically or antiferromagnetically to the CoFeB layer. Noting that the $(Co/Pt)_n$ (n=2-6) multilayers have been frequently used in MRAM production as a part of the synthetic antiferromagnetic reference layer with large PMA for pinning, we choose the (Co 0.4 nm /Pt 0.4 nm)$_2$ multilayers (referred below as CoPt) to realize thin ferromagnetic multilayers with large PMA for evaluating the SOT performance of the BiSb layer. Since c-plane (0001) sapphire substrate is helpful for $(Co/Pt)_n$ growth with high PMA, we select sapphire substrates in this work. Figure 4.1(a) shows the structure of samples.

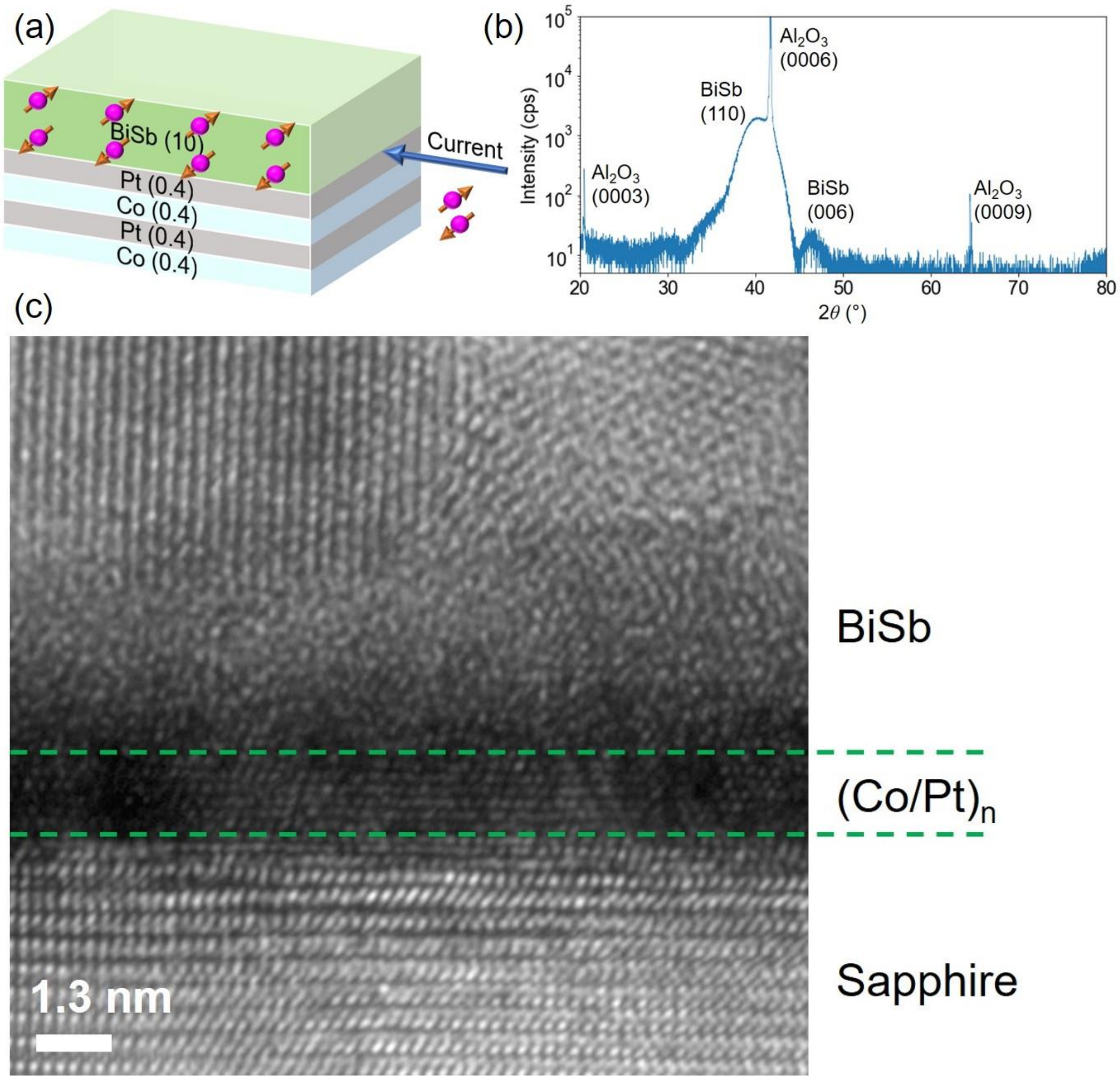

Figure 4.1 **(a)** Schematic structure of our multilayers. **(b)** XRD spectrum, and **(c)** cross-sectional TEM image of the sample.

Figure 4.1(a) shows the studied multilayer heterostructure, which consists of perpendicularly magnetized (Co 0.4 nm /Pt 0.4 nm)$_2$ multilayers / 10 nm $Bi_{0.85}Sb_{0.15}$ topological insulator layer, capped by 1 nm MgO / 1 nm Pt (not shown). The multilayers were deposited on *c*-plane sapphire substrates by a combination of direct current (DC) and radio-frequency (RF) magnetron sputtering in a multi-cathode chamber. Characterization by XRD and TEM shows that the BiSb layer is polycrystalline with the dominant (110) orientation, shown in Figure 4.1(b) and 4.1(c), respectively. The existence of metallic surface states as well as insulating bulk states with a band gap more than 170 meV for thin (< 20 nm) BiSb films was confirmed in Chapter 3.

Hall bar device fabrication process

For electrical measurements, we fabricated 25 μm-wide Hall bars by optical lithography. In order to minimize the diffusion of Sb atoms to FM layer induced by high temperature during baking the photoresist and ion milling process, we employed the lift-off process to fabricate the Hall bar, as shown in Figure 4.2. The sample is heated only once during the electrode fabrication. The fabrication process is as follows.

(1) Photoresist is formed on the sapphire substrate.
(2) A Hall-bar shaped hole is patterned by photolithography and development.
(3) Sample growth by sputtering deposition.
(4) The samples are patterned into 90 μm-long × 25 μm-wide Hall bars by lift-off.
(5) The same process (different pattern) as (1) – (2) is reproduced for electrodes deposition.
(6) 45 nm-thick Pt were deposited as electrodes by sputtering.
(7) The devices are completed by lift-off to form the electrodes. The effective length of the devices is reduced to 50 μm.

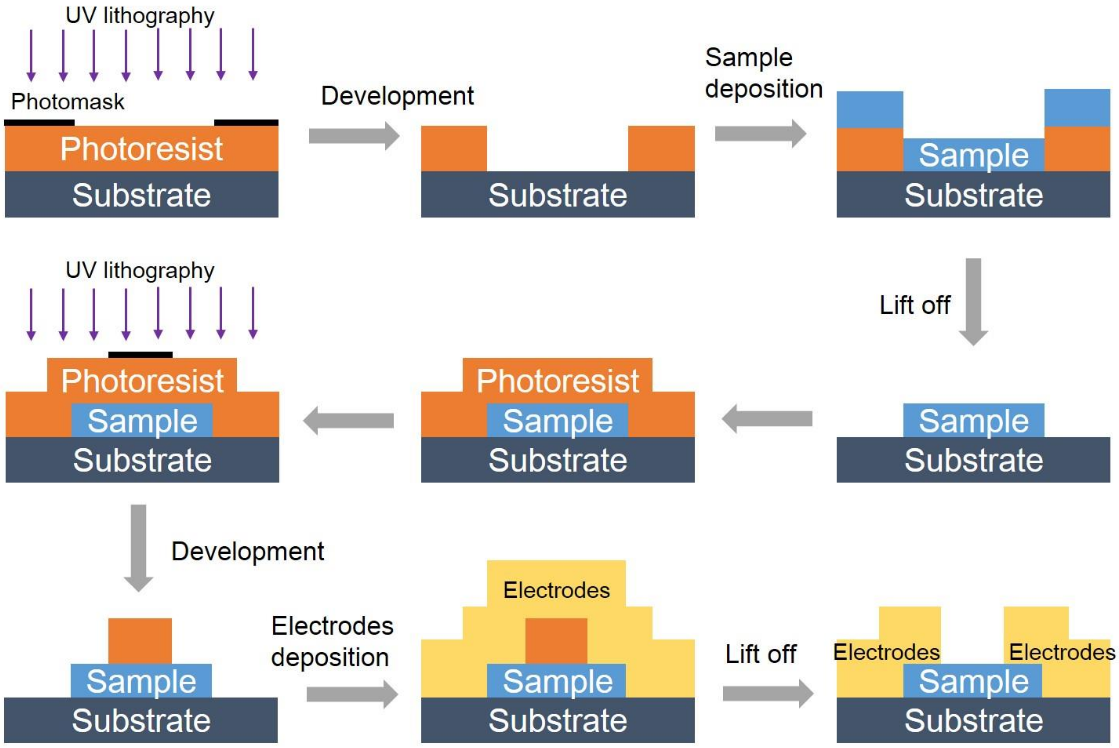

Figure 4.2 Device fabrication process for the Hall bars in this Chapter

4.3 Characterization techniques

Superconducting quantum interference device

In this work, we use superconducting quantum interference device (SQUID) to evaluate the magnetization and the magnetic anisotropy field of magnetic thin films. SQUID uses superconducting loops and the Josephson effect. There are two Josephson junctions connected in parallel. If there is no external magnetic field, the input current equally flows into the two junctions. If there is an external field, the current in two branch will be different to create a magnetic field to compensate the external magnetic flux. Thereby, there will be a voltage induced in the circuit. By measuring this voltage, the external magnetic field can be calculated.

Hall effect measurement

We perform the Hall effect measurement in order to detect the Hall effect and anomalous Hall effect. The Hall bar device is put into an external magnetic field. The DC current is applied to the x direction, and the transverse Hall voltage is measured. The Hall resistivity can be expressed as: $\rho_H = \rho_O + \rho_{AHE} = R_O H_{ext} + R_{AHE} M$, where ρ_O is the ordinary Hall resistivity, ρ_{AHE} is the anomalous Hall resistivity, H_{ext} is the external magnetic field, M is the magnetization of sample, R_O and R_{AHE} are the coefficient of ordinary and anomalous Hall effect, respectively. By sweeping the external magnetic field, the hysteresis loop is acquired, and the Hall resistance of sample can be measured. The experimental set-up is shown in Figure 4.3(a).

Second harmonic measurement

We performed the second harmonic Hall measurements to evaluate the spin Hall angle [5]. The schematic of measurement is shown in Figure 4.3(b). An alternating current (AC) $I = I_0 \sin\omega t$ (ω = 259.68 Hz) was applied to the Hall bar under a sweeping external field along the x direction. Under an AC current, BiSb generate an antidamping-like field H_{AD}, originated from the SHE, and field-like field H_{FL} originated from the Rashba-Edelstein effect. In TI/FM systems, the spin Hall effect dominates the Rashba-Edelstein effect, thus, the H_{FL} can be neglected [2, 6, 7]. The H_{AD} induces oscillation of the magnetic vector around the equilibrium position under the AC current [8-10]. Therefore, the Hall resistance R_{AHE} can be expressed as $R_{AHE} = R_{AHE0} + \Delta R_{AHE} \sin\omega t$, in which ΔR_{AHE} corresponds to the oscillation of magnetization. Therefore, the Hall voltage is given by $V_H = I_0 \sin\omega t \times (R_{AHE0} + \Delta R_{AHE} \sin\omega t) = I_0 R_{AHE0} \sin\omega t + I_0 \Delta R_{AHE} \sin^2\omega t = V_{xy}^{\omega} + V_{xy}^{2\omega}$, in which the first harmonic term V_{xy}^{ω} corresponds to the anomalous Hall effect, and the second harmonic term $V_{xy}^{2\omega}$ corresponds to the oscillation induced by H_{AD}. Both of V_{xy}^{ω} and $V_{xy}^{2\omega}$ is measured by a lock-in amplifier. The $V_{xy}^{2\omega}$ is given by [10]:

$$R_{\mathrm{H}}^{2\omega} = \frac{R_{\mathrm{H}}}{2}\frac{H_{\mathrm{AD}}}{H_x - H_{\mathrm{u}}(H_x/|H_x|)} + R_{\mathrm{thermal}}\frac{H_x}{|H_x|} \qquad (4.1)$$

where H_{AD} is the antidamping-like effective field, R_{H} is the Hall resistance, H_{u} is the PMA field and R_{thermal} is the contribution from the anomalous Nernst (ANE) and spin Seebeck (SSE) effects. H_{AD} can be obtained by fitting this equation to the experimental data, and the spin Hall angle can hereby evaluated. The set-up of second harmonic measurement is shown in Figure 4.3(c).

SOT magnetization switching

The experimental set-up is shown in Figure 4.3(d). A small in-plane magnetic field is applied along the *x* direction to break symmetry. A DC or pulse current is applied to the Hall bar device. The current induces a pure spin current in BiSb layer, which induces a SOT and switch the magnetization in the CoPt layer. The magnetization switching is detected by measuring the V_{xy} under a small DC current.

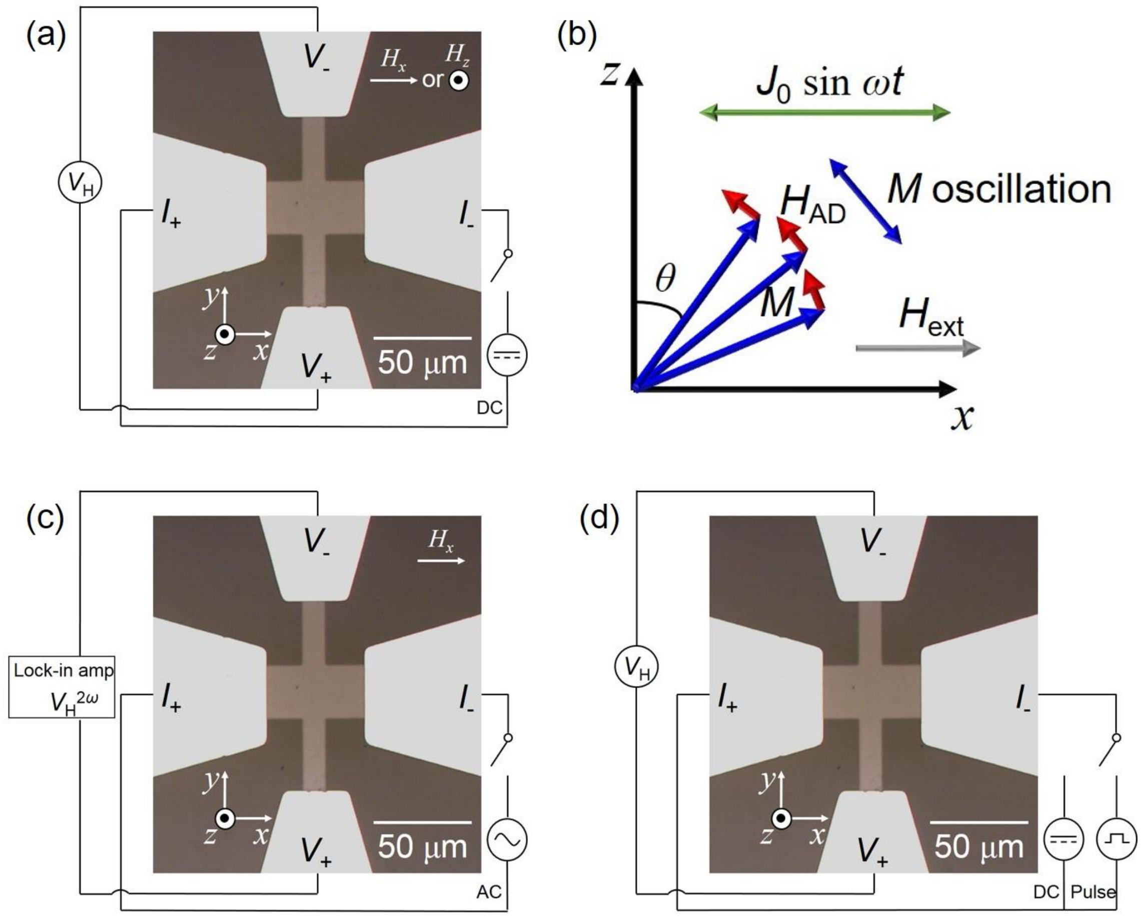

Figure 4.3 **(a)(c)(d)** Optical images of Hall bar with the experimental set-up for **(a)** Hall effect, **(c)** Second harmonic measurements and **(d)** SOT magnetization switching. **(b)** Schematic for second harmonic measurements.

4.4 Spin Hall angle evaluation

First, we evaluate the conductivity of BiSb. By measuring the resistance of $(Co/Pt)_2$ / BiSb and $(Co/Pt)_2$ thin films, we estimate that the conductivity of the BiSb from the parallel resistor model. The conductivity of BiSb layer is $1.5\times10^5\ \Omega^{-1}m^{-1}$, which is much higher than that of sputtered $Bi_{1-x}Se_x$, and close to that of MBE grown BiSb on GaAs(111)A substrates. This demonstrates that is possible to grow highly conductive BiSb topological thin films on top of perpendicularly magnetized metallic layers by the sputtering technique. Thanks to the high conductivity of the BiSb layer, 50% of the applied current flows into the BiSb and contribute to the SOT magnetization switching.

Figure 4.4(a) shows the magnetic hysteresis curves of the as-grown sample measured by a SQUID under an in-plane and out-of-plane external magnetic field, respectively. The saturation magnetization M_{CoPt}, normalized by the CoPt layer thickness (t_{CoPt} = 1.6 nm), is 613 emu·cm^{-3}. The uniaxial anisotropy field H_{u} = 15 kOe is very large for the as-grown film. Figure 4.4(b) and 4.4(c) shows the anomalous Hall resistance (R_{H}) measured for a Hall bar under a sweeping out-of-plane and in-plane field, respectively, which confirms PMA of the CoPt layer. In Fig. 4.4(c), we show the fitting curve (red curve) to the data by the function $R_{\mathrm{H}} = R_{\mathrm{H}}(0)\sqrt{1-\left(\frac{H_{\mathrm{k}}}{H_{\mathrm{u}}}\right)^2}$, in which $R_{\mathrm{H}}(0)$ is the Hall resistance at zero field, H_x is the external field, and H_{u} is the PMA field. From this fitting, we obtain a PMA field of 5.2 kOe. H_{u} is reduced after Hall bar device fabrication by optical lithography undergoing a cycle of thermal annealing, but is still much larger than that of NiFe or CoTb used in previous works.

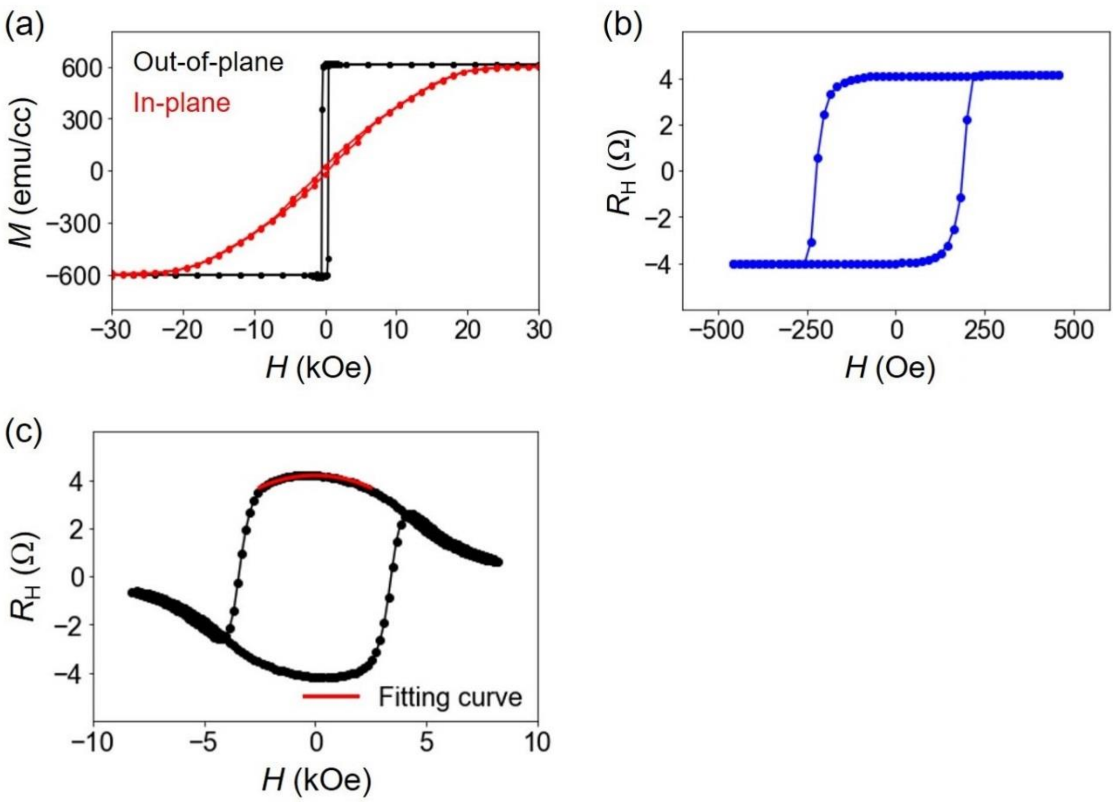

Figure 4.4 **(a)** Magnetization curves of as-grown Co/Pt multilayers. **(b)(c)** Hall resistance of a Hall bar device measured with magnetic field applied perpendicular to the film plane and in-plane along the current direction.

Next, we performed the second harmonic Hall measurements to evaluate the spin Hall angle. Figure 4.5 shows $R_H^{2\omega}$- H_x curves at different current density. Fitting Eq. (4.1) to the high field data in the $R_H^{2\omega}$- H_x curves yields H_{AD} (red curves in Figure 4.5). Figure 4.6 shows H_{AD} as a function of J^{BiSb}. From the H_{AD} / J^{BiSb} gradient, we can calculate the effective spin Hall angle $\theta_{SH}^{eff} = \frac{2e}{\hbar} M_{CoPt} t_{CoPt} \frac{H_{AD}}{J^{BiSb}} = 12.3$.

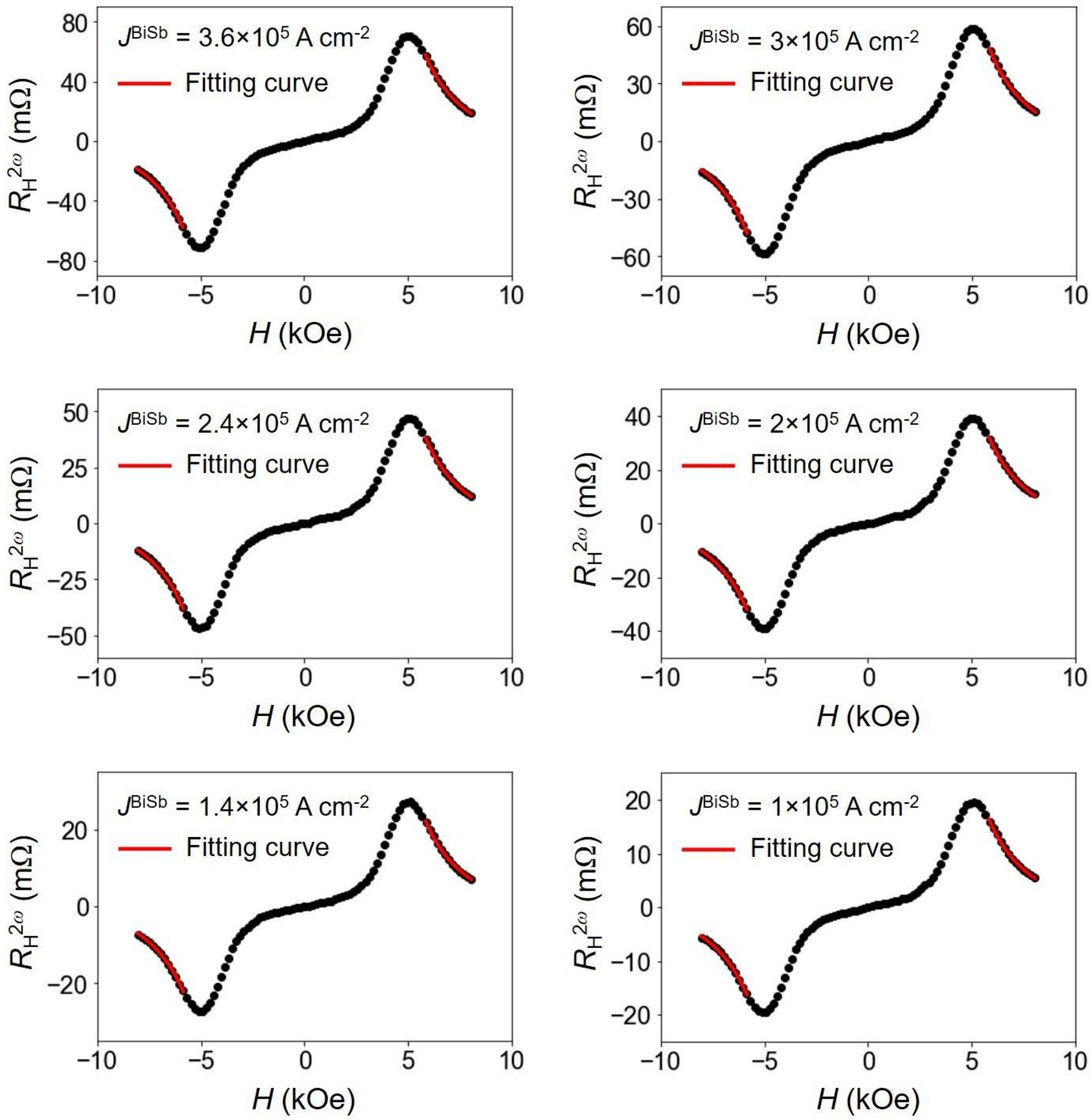

Figure 4.5 Second harmonic Hall resistance data for estimation of the antidamping-like H_{AD} as a function of J_{BiSb}. The red curves are the theoretical fitting using Equation 4.1.

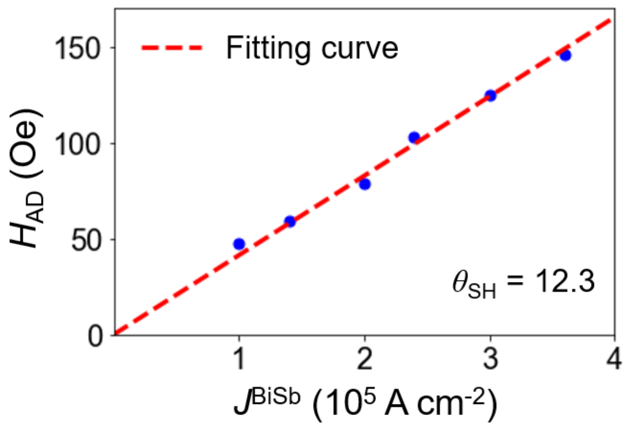

Figure 4.6 H_{AD} as a function of J^{BiSb}.

It is reported that CoPt multilayers can generate a "self" spin-orbit torque because of the spin Hall effect in Pt [11]. we performed the same second harmonic measurement for a $[Co(0.4)/Pt(0.4)]_2$ sample without BiSb layer to evaluate the "self" spin-orbit torque and "self" spin Hall angle. The results are shown in Figure 4.7. By fitting the high field data in the $R_H^{2\omega}$- H_x curve (Figure 4.7(a) – 4.7(e)) to the Equation (4.1), we obtained H_{AD} at each current density. Figure 4.7(f) shows H_{AD} as a function of J^{CoPt}, from which we can evaluate that the spin Hall angle of CoPt is 0.26. This value is consistent with those observed in $Pt/(Co/Pt)_n$ by Jinnai et al. with a maximum effective spin Hall angle of 0.30 for the underneath Pt layer [11]. By reading the phase of second harmonic signal by the lock-in amplifier (Figure 4.8), we confirmed that the SOT of CoPt multilayers has the same polarity as that of $(Co/Pt)_2$ / BiSb. This indicates that the SOT of CoPt assists the spin Hall effect in $(Co/Pt)_2$ / BiSb, and we need to subtract this effect. The contribution from SOT of CoPt is calculated by (θ_{SH}^{Pt} / 12.3) × (J^{CoPt} /J^{BiSb}) = 13%. Therefore, we obtain the intrinsic spin Hall angle of BiSb θ_{SH} = 10.7, which demonstrates the feasibility of BiSb for ultralow power SOT-MRAM.

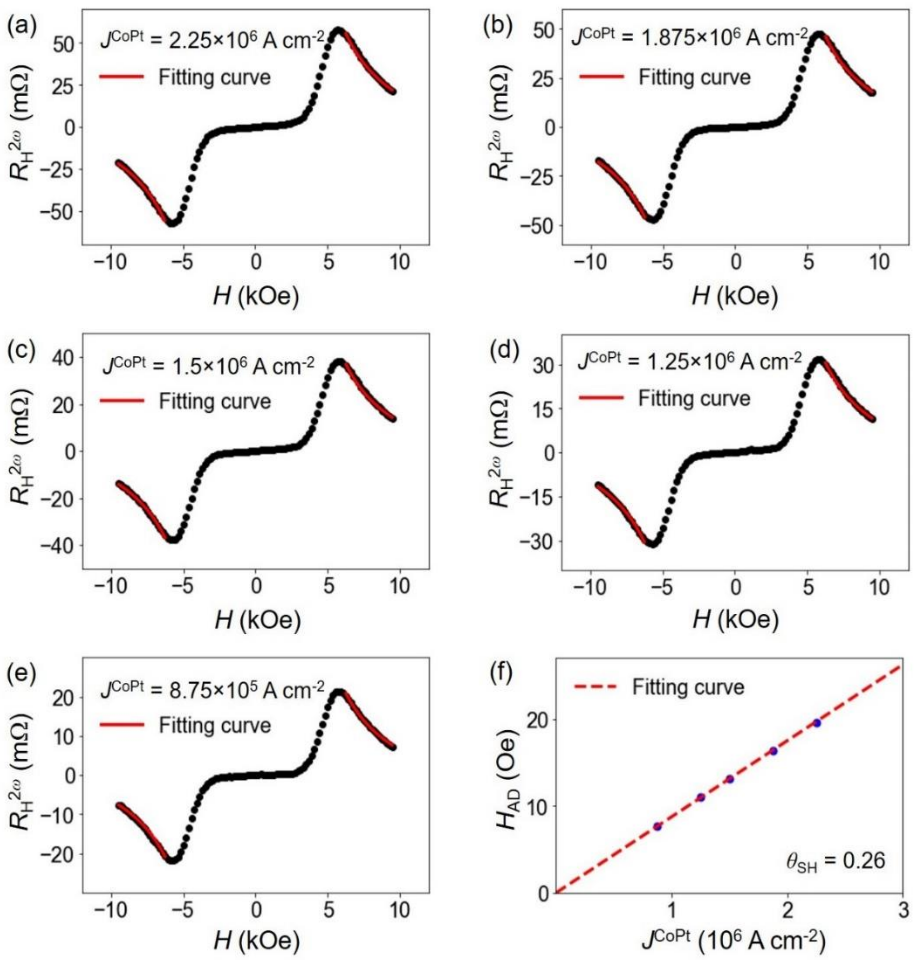

Figure 4.7 **(a) – (e)** 2nd harmonic Hall resistance as a function of in-plane magnetic field at various current densities J^{CoPt}. Solid lines are fitting curves using Equation 4.1 in the manuscript. **(f)** H_{AD} as a function of J^{CoPt}.

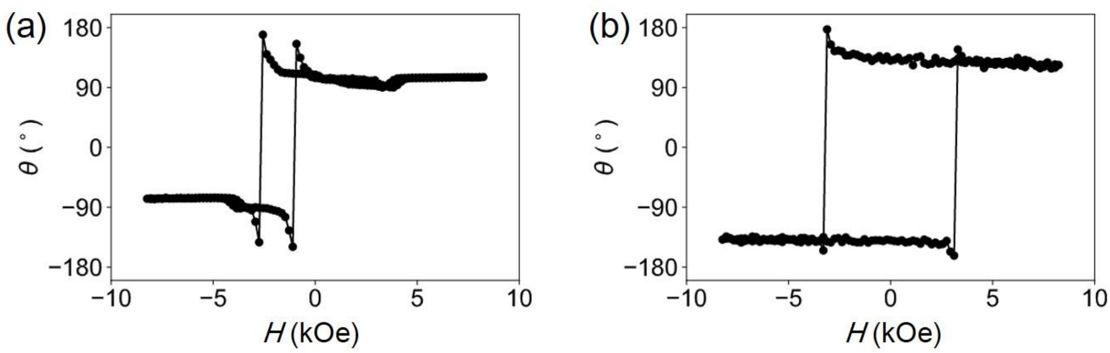

Figure 4.8 Phase of second harmonic voltage signal of **(a)** $(Co/Pt)_2$ / BiSb and **(b)** $(Co/Pt)_2$ thin films.

4.5 Ultrahigh efficient spin-orbit torque magnetization switching by DC and pulse currents

We demonstrate ultrahigh efficient and robust SOT magnetization switching in the CoPt/BiSb multilayers. Figure 4.9 shows the SOT magnetization switching by DC currents with an applied external field along the *x* direction. We achieved Hall resistance switching whose amplitude is consistent with that of the Hall resistance loop shown in Figure 4.4(b), indicating full magnetization switching. The switching direction is reversed when the external magnetic field direction is reversed, which is consistent with the characteristic of SOT. Typical DC threshold switching current density $J_{\mathrm{th}}^{\mathrm{BiSb}}$ is 1.5×10^6 Acm^{-2} at the bias field of 2.75 kOe. Note that thanks to the high electrical conductivity $\sigma = 1.5\times10^5\ \Omega^{-1}\mathrm{m}^{-1}$ of BiSb, the total current density including the shutting current in the CoPt is kept at 2.6×10^6 Acm^{-2}.

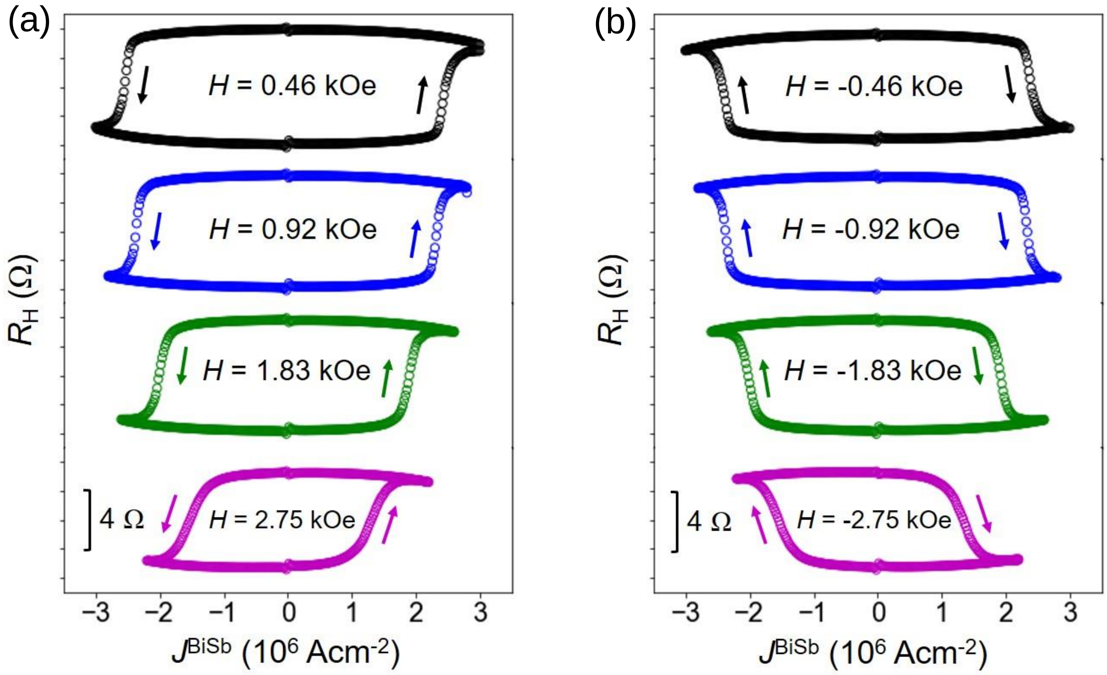

Figure 4.9 SOT magnetization switching by DC currents. Switching loops measured under an in-plane magnetic field applied along **(a)** +*x* direction and **(b)** - *x* direction.

Next, we performed SOT magnetization switching by pulse currents. Figure 4.10(a) and 4.10(b) show a representative SOT switching loops by 0.1 ms pulse currents at +1.83 kOe and -1.83 kOe, respectively. Figure 4.10(c) plots J_{th}^{BiSb} at various pulse width t_{pulse}, and the theoretical fitting using the thermal activation model $J_{th}^{BiSb} = J_0^{BiSb} \times \left[1-\frac{1}{\Delta}\ln\left(\frac{\tau_{pulse}}{\tau_0}\right)\right]$ [12], where J_0^{BiSb} is the zero-kelvin threshold switching current density, Δ is the thermal stability factor, and $1 / \tau_0 = 1$ GHz ($\tau_0 = 1$ ns) is the attempt switching frequency. The fitting yields $J_0^{BiSb} = 4.6 \times 10^6$ Acm^{-2} and Δ = 38. Because magnetization switching occurs by domain wall nucleation and domain wall motion, Δ reflects the energy barrier of the volume with size equal to the domain wall width, i.e., Δ should be considered as the energy barrier to nucleate a domain wall, rather than the energy barrier for coherently switching of the whole volume of the magnetic layer [13]. Therefore, Δ evaluated by this way is smaller than that should be expected for switching the whole volume of the magnetic layer. Nevertheless, the obtained Δ of CoPt is large enough to ensure that the total Δ in ferromagnetically (antiferromagnetically) coupled CoFeB/Ta(Ru)/CoPt free layer can exceeds 60 for 10 years thermal stability, while the switching current density remains the same [14]. Our data can be used to estimate the performance of BiSb-based SOT-MRAM. For example, we estimate that the switching current density at t_{pulse} = 10 ns would be J_{th}^{BiSb} (10 ns) = 4.3×10^6 Acm^{-2}, which is about 20 times smaller than that of heavy metals.

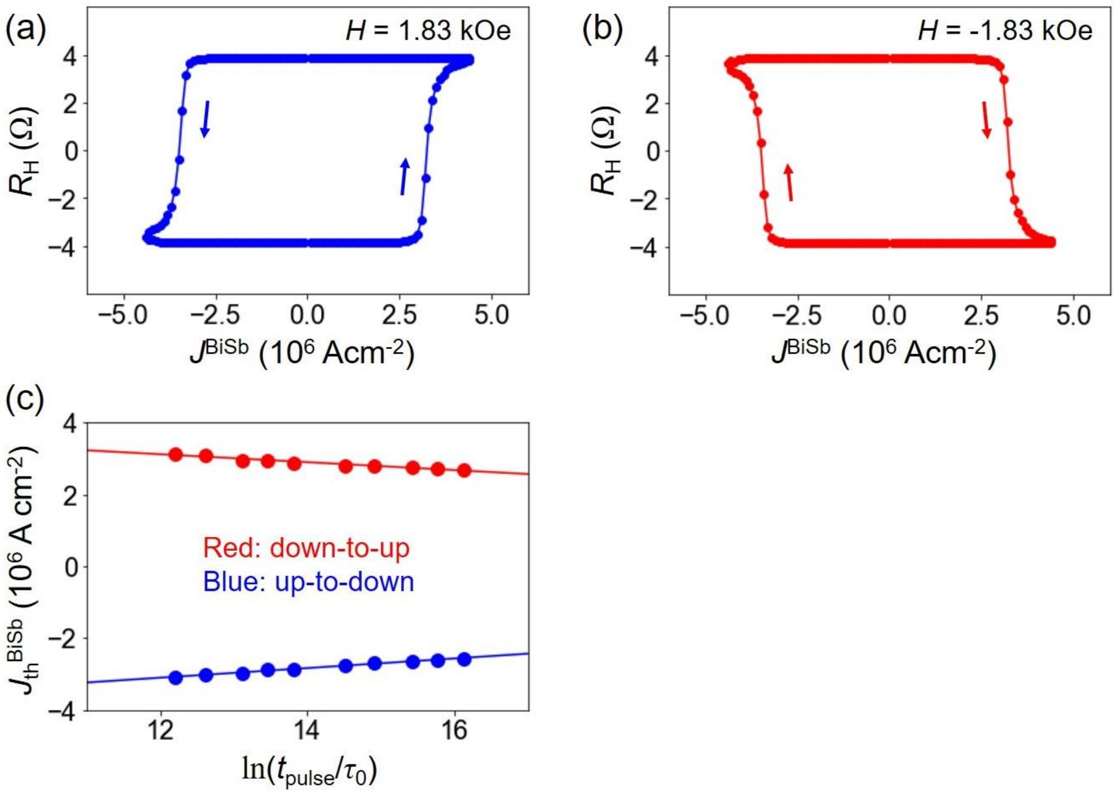

Figure 4.10 SOT magnetization switching by pulse currents. **(a)(b)** Switching loop by 0.1 ms pulse currents under an in-plane magnetic field of H = +1.83 kOe and -1.83 kOe, respectively. **(c)** Threshold current density J_{th}^{BiSb} as a function of t_{pulse}.

Finally, we demonstrate robust SOT switching in the CoPt/BiSb junction. For this purpose, we applied a sequence of 75 pulses (J_{th}^{BiSb} = 4.4×10^6 Acm^{-2}, t_{pulse} = 0.1 ms) as shown in the top panel of Figure 4.11. The Hall resistance data recorded for a total of 150 pulses under ±1.83 kOe are shown in the bottom panel in Figure 4.11. We observed a robust SOT switching with no change in the device characteristics, indicating that the BiSb topological insulator deposited by the sputtering technique has great potential for realistic SOT-MRAM.

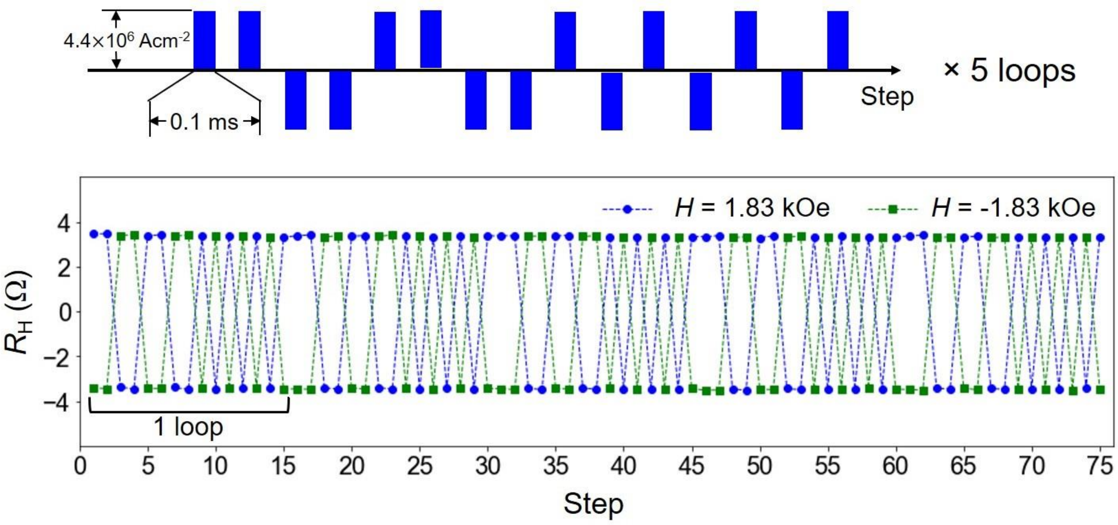

Figure 4.11 Robust SOT magnetization switching by 0.1 ms pulse current.

As a control experiment, we attempt to switch the magnetization of the $(Co/Pt)_2$ multilayers by the self-SOT effect. We applied the same current density to the $(Co/Pt)_2$ multilayers as that flowed into the $[Co/Pt]_2$ multilayers in the $[Co/Pt]_2$/BiSb heterostructure. In the first experiment shown in Figure 4.12(b), we applied a DC current up to $\pm1.38\times10^7$ Acm^{-2} under an in-plane bias field of 2.75 kOe. We observed no switching but Joule heating. Next, we attempt self-SOT switching by 1 ms and 0.1 ms pulse currents ramped up to $\pm2.5\times10^7$ Acm^{-2} and $\pm2.75\times10^7$ Acm^{-2}, respectively. Again, we observed no switching as shown in Figure 4.12(c) and 4.12(d).

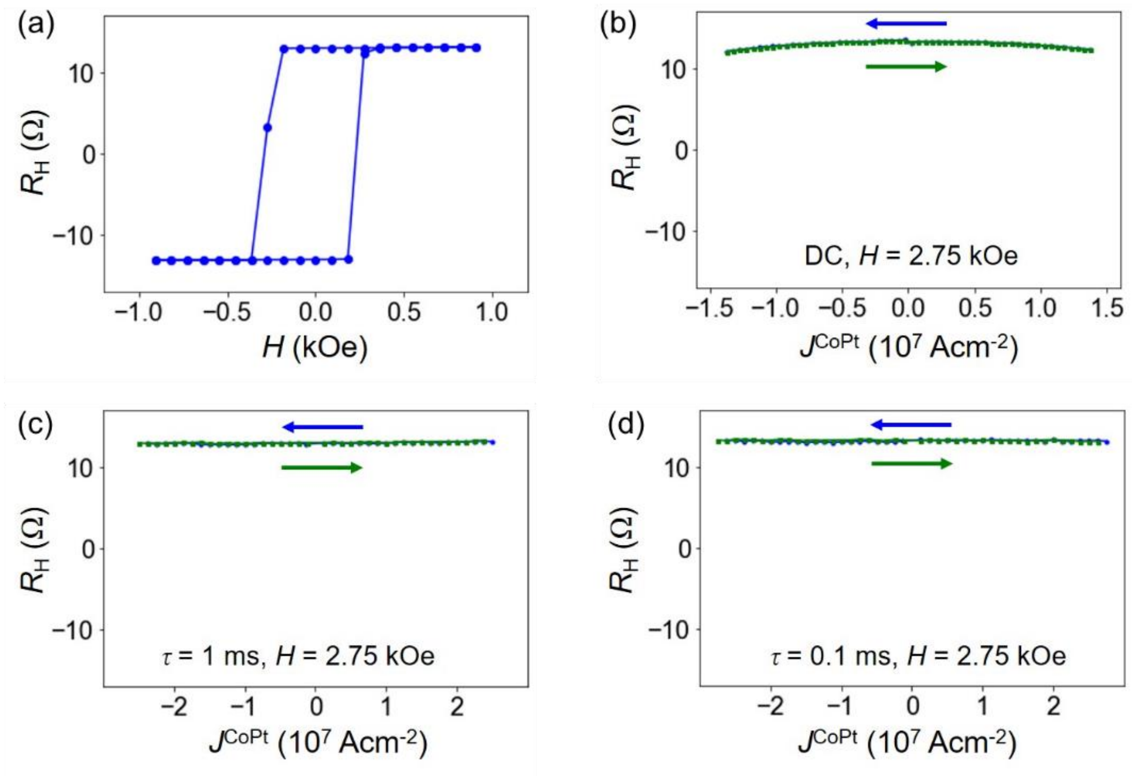

Figure 4.12 **(a)** Hall resistance of a $[Co/Pt]_2$ Hall bar device measured with a perpendicular magnetic field. Magnetization switching test for Co/Pt multilayers by **(b)** DC, **(c)** and **(d)** pulse current with pulse width of τ = 1 ms and τ = 0.1 ms, respectively.

4.6 Discussion

Table 4.1 summarizes θ_{SH}, σ, the spin Hall conductivity $\sigma_{SH} = (\hbar/2e)\sigma\theta_{SH}$, and the SOT normalized power consumption P_n at room temperature of several heavy metals and TIs. Here, θ_{SH} of TIs are their best values reported in literature. For the calculation of the P_n, we assumed bilayers of spin Hall material (thickness t = 6 nm for heavy metals and t = 10 nm for TIs) and CoFeB (thickness t_{FM} = 1.5 nm, conductivity $\sigma_{FM} = 6\times10^5\ \Omega^{-1}\ m^{-1}$). Considering the shunting current in the ferromagnetic layer, the SOT power consumption is proportional to $(\sigma t + \sigma_{FM}t_{FM})/(\sigma t\theta_{SH})^2$. One can see that not only θ_{SH} but also σ affect the SOT power consumption, a fact usually overlooked in literature. For example, while the sputtered Bi_xSe_{1-x} has a much larger spin Hall angle (θ_{SH} = 18.6) [15] than that (θ_{SH} = 3.5) of MBE-grown Bi_2Se_3 [6], their power consumption is nearly the same, because Bi_xSe_{1-x} has poorer crystal quality than Bi_2Se_3 and thus very low conductivity. Meanwhile, the sputtered BiSb thin film in this work shows both high $\sigma = 1.5 \times 10^5\ \Omega^{-1}\ m^{-1}$ and large θ_{SH} = 10.7, which are optimal for both small switching current density and small switching power consumption [16]. Indeed, the switching power consumption for sputtered BiSb is 50 times smaller than that for sputtered Bi_xSe_{1-x}, and over 300 times smaller than that for W, which is the most used heavy metal in SOT-MRAM development. The small switching current density and switching power also help suppress failure of the spin Hall layer due to electromigration and Joule heating [17].

SOT Materials	$\lvert\theta_{SH}\rvert$	σ ($\Omega^{-1}m^{-1}$)	$\lvert\sigma_{SH}\rvert$ [($\hbar/2e$) $\Omega^{-1}m^{-1}$]	P_n
Ta	0.15	5.3×10^5	8.0×10^4	1
Pt	0.08	4.2×10^6	3.4×10^5	3.6×10^{-1}
W	0.4	4.7×10^5	1.9×10^5	1.6×10^{-1}
$(Bi_{0.07}Sb_{0.93})_2Te_3$ (MBE)	2.5	1.8×10^4	4.5×10^4	3.0×10^{-1}
Bi_2Se_3 (MBE)	3.5	5.7×10^4	2.0×10^5	2.1×10^{-2}
Bi_xSe_{1-x} (Sputtered)	18.6	7.8×10^3	1.5×10^5	2.6×10^{-2}
$Bi_{0.85}Sb_{0.15}$ (Sputtered)	10.7	1.5×10^5	1.6×10^6	5.2×10^{-4}

Table 4.1 Spin Hall angle θ_{SH}, electrical conductivity σ, spin Hall conductivity σ_{SH}, and SOT normalized power consumption P_n of several heavy metals and topological insulators.

Note that the obtained θ_{SH} is still smaller than the highest θ_{SH} ~ 52 observed in the MBE-grown BiSb(012), because BiSb deposited on top of Pt is polycrystalline and does not have the optimized (012) orientation. We expect that even higher θ_{SH} can be obtained if we can control the crystal orientation of BiSb by inserting a seed layer that promotes the (012) orientation. Our results demonstrate the feasibility of BiSb for not only ultralow power SOT-MRAM but also other SOT-based spintronic devices, such as race-track memories [18] and spin Hall oscillators [19, 20].

References

[1] Ueda Y., et al. Epitaxial growth and characterization of $Bi_{1-x}Sb_x$ spin Hall thin films on GaAs(111)A substrates. Appl. Phys. Lett. 110, 062401 (2017).

[2] Khang N. H. D. et al, A conductive topological insulator with large spin Hall effect for ultralow power spin–orbit torque switching. Nat. Mater. 17, 808 (2018).

[3] Chi Z., et al. The spin Hall effect of Bi-Sb alloys driven by thermally excited Dirac-like electrons. Sci. Adv. 6, eaay2324 (2020).

[4] Roschewsky N., et al. Spin-orbit torque and nernst effect in Bi-Sb/Co heterostructures. Phys. Rev. B 99, 195103 (2019).

[5] Hayashi M., et al. Quantitative characterization of the spin-orbit torque using harmonic Hall voltage measurements. Phys. Rev. B 89, 144425 (2014).

[6] Mellnik A. R., et al. Spin-transfer torque generated by a topological insulator. Nature 511, 449 (2014).

[7] Fan Y., et al. Magnetization switching through giant spin–orbit torque in a magnetically doped topological insulator heterostructure. Nat. Mater. 13, 699 (2014).

[8] Kim J., et al. Layer thickness dependence of the current-induced effective field vector in Ta | CoFeB | MgO. Nat. Mater. 12, 240 (2013).

[9] Shao Q., et al. Strong Rashba-Edelstein effect-induced spin–orbit torques in monolayer transition metal dichalcogenide/ferromagnet bilayers. Nano Lett. 16, 7514 (2016).

[10] Wu H., et al. Spin-Orbit Torque Switching of a Nearly Compensated Ferrimagnet

by Topological Surface States. Adv. Mater. 31, 1901681 (2019).

[11] Jinnai B., et al. Spin-orbit torque induced magnetization switching in Co/Pt multilayers. Appl. Phys. Lett. 111, 102402 (2017).

[12] Koch R. H., et al. Time-resolved reversal of spin-transfer switching in a nanomagnet. Phys. Rev. Lett. 92, 088302 (2004).

[13] Sato H., et al. CoFeB Thickness Dependence of Thermal Stability Factor in CoFeB/MgO Perpendicular Magnetic Tunnel Junctions. IEEE Magn. Lett. 3, 3000204 (2012).

[14] Sato H., et al. Perpendicular-anisotropy CoFeB-MgO magnetic tunnel junctions with a MgO/CoFeB/Ta/CoFeB/MgO recording structure. Appl. Phys. Lett. 101, 022414 (2012).

[15] Mahendra DC, et al. Room-temperature high spin–orbit torque due to quantum confinement in sputtered $Bi_xSe_{(1-x)}$ films. Nat. Mater. 17, 800 (2018).

[16] Li X., et al. Materials Requirements of High-Speed and Low-Power Spin-Orbit-Torque Magnetic Random-Access Memory. IEEE J. Electron Devices Soc. 8, 674 (2020).

[17] Shiokawa Y., et al. High write endurance up to 10^{12} cycles in a spin current-type magnetic memory array. AIP Adv. 9, 035236 (2019).

[18] Ryu K.-S. et al. Chiral spin torque at magnetic domain walls. Nat. Nanotech. 8, 527–533 (2013).

[19] Liu L., et al. Magnetic Oscillations Driven by the Spin Hall Effect in 3-Terminal Magnetic Tunnel Junction Devices. Phys. Rev. Lett. 109, 186602 (2012).

[20] Shirokura T., et al. Bias-field-free spin Hall nano-oscillators with an out-of-plane precession mode. J. Appl. Phys. 127, 103904 (2020).

Chapter 5 Low power spin-orbit torque switching in sputtered BiSb topological insulator / perpendicularly magnetized CoPt / MgO multilayers on oxidized Si substrate

5.1 Introduction

In Chapter 4, we demonstrated that sputtered BiSb has a large spin Hall angle of 10.7, and high electrical conductivity of $1.5\times10^5\ \Omega^{-1}\ \mathrm{m}^{-1}$. That work confirms the potential of BiSb for the application in mass production of SOT-MRAM. Nevertheless, realistic SOT-MRAM is integrated on Si substrates. In recent years, integration of embedded MRAM [1] has been implemented with exclusive advantages, such as high reading/writing speed and long lifetime [2]. Furthermore, there are reports of neuromorphic computing by using spin-torque nano-oscillators as physical neurons [3-5]. These works use devices based on STT, while SOT-based device is expected to increase the performance with improved writing speed and reliability. The core structure of SOT-MRAM and spin-torque nano-oscillators is MTJ consisting of a pinned FM layer, an insulating tunnel barrier, and a free FM layer, and BiSb spin Hall layer in contact with the free layer. The de-facto tunnel barrier material is MgO, while the FM layers are typically CoFeB, FeB, or CoFe, which may be coupled to Co/Pt multilayers with strong PMA for pinning. For realistic MRAM, MTJs have to be deposited on Si/SiO_x substrates [3-5], thereby performance of BiSb deposited on Si/SiO_x substrate is of great interest. Although the SOT effect of BiSb has been studied in oxidized Si/CoTb/BiSb heterostructures, the effective spin Hall angle θ_{SH}^{eff} of BiSb is reduced to 1.2 due to the low spin transmissivity at the CoTb interface [6]. Furthermore, the studied CoTb layer is ferrimagnetic with small magnetization and small PMA field of ~ 1 kOe, which is not suitable for SOT-MRAM. Thus, study of SOT effect in junctions of BiSb and high-PMA ferromagnetic layer deposited on oxidized Si substrate is strongly required.

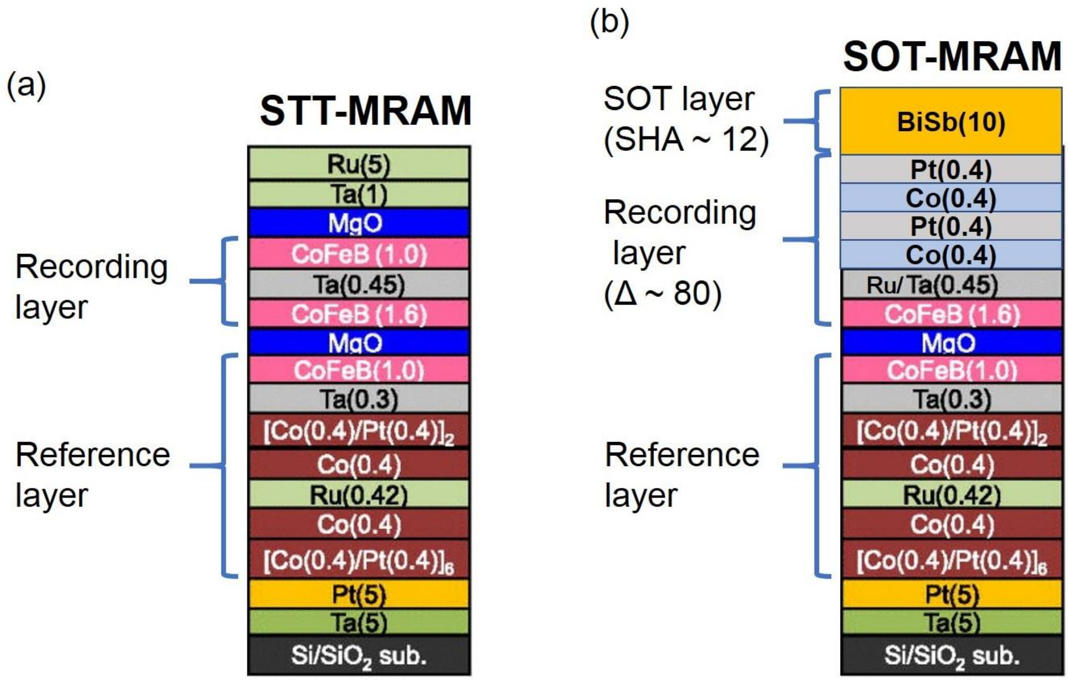

Figure 5.1 (a) STT-MRAM MTJ stack with a double interface MgO/CoFeB/Ta/CoFeB/MgO free layer [7] © [2014] IEEE. **(b)** BiSb-based SOT-MRAM stack with CoFeB/Ta(Ru)/(Co/Pt)n/BiSb (right) free layer.

Based on the works in Chapter 4, we propose a practical structure for MRAM, shown in Figure 5.1. It is an improvement from the MTJ stack developed for STT-MRAM by Ikeda et al [7]. This structure has a high thermal stability factor of $\Delta \sim 80$ at diameter of 50 nm. Typically, the perpendicular magnetic anisotropy (PMA) at a single CoFeB/MgO interface can yield only $\Delta \sim 40$, which is not enough for STT-MRAM applications, thus a double interface MgO/CoFeB/Ta/CoFeB/MgO free layer was proposed [8], as shown in Figure 5.1(a). Based on this structure, we propose a SOT-MRAM, shown in Figure 5.1(b), that CoFeB is ferromagnetically or antiferromagnetically coupled to $(Co/Pt)_n$

multilayers with a middle Ta or Ru layer, then BiSb is deposited on top of the $(Co/Pt)_n$ multilayers. This scenario has many advantages. First, the $(Co/Pt)_n$ multilayers add an extra Δ (~ 40 for n = 2 as demonstrated in this work) so that the total Δ ~ 80 can be achieved. It has been shown that it is possible to increase Δ by this way without increasing the switching current density [8]. Furthermore, we can increase the number of (Co/Pt) pairs to keep Δ > 60 when the diameter is further reduced. Secondly, the $(Co/Pt)_n$ multilayers protect the CoFeB layer from diffusion of Bi/Sb atoms during BiSb deposition, which can damage the CoFeB layer. Finally, we have demonstrated in Chapter 4 that a large spin Hall angle larger than 10 can be achieved with the BiSb/$(Co/Pt)_n$ interface. In this chapter, we concentrate on the top BiSb/$(Co/Pt)_n$ on Si/SiO_x substrate.

We study the SOT characteristics in all-sputtered BiSb – Pt/Co/Pt – MgO heterostructures deposited on oxidized Si substrates. The Pt/Co/Pt trilayers have a large PMA of 4.5 kOe. We found that the BiSb layer has a large effective spin Hall angle $\theta_{\mathrm{SH}}^{\mathrm{eff}}$ = 2.4 and high electrical conductivity of $\sigma = 1.0\times10^5\ \Omega^{-1}\mathrm{m}^{-1}$. The magnetization can be switched by a current density as small as 2.3×10^6 Acm^{-2} at pulse width of 100 μs, which is 1 or 2 orders of magnitudes smaller than that in heavy metals. Robust switching and fast switching down to 100 ns are also realized. Our work demonstrates the high efficiency and robustness of BiSb as a spin current source in realistic SOT devices.

5.2 Sample growth

We prepare the heterostructure consisting of $Bi_{0.85}Sb_{0.15}$ (10 nm) – Pt (0.8 nm)/Co (0.6 nm)/ Pt (0.8 nm) – MgO (10 nm) on oxidized Si substrate, from top to bottom, by direct-current (for BiSb and all metallic layers) and radio-frequency (for MgO) magnetron sputtering, as shown in Figure. 5.2(a). The sample is capped by MgO (1 nm) and Pt (1 nm) for preventing the oxidation of BiSb. MgO is deposited on the Si/SiO_x substrate to compensate the surface roughness of SiO_x. The Pt/Co/Pt trilayers (denoted below as CoPt) are designed to be symmetric to eliminate any parasitic SOT effect from the Pt layers and to generate large enough PMA.

For electrical measurements, the sample was patterned into 50 μm-long × 25 μm-wide Hall bars by the same lift-off method as introduced in chapter 4. In μm-size Hall bar, the magnetization switching occurs through domain wall nucleation and domain wall motion [9], thus the switching time is limited by the propagation time of the domain walls through the Hall bar. Therefore, for SOT switching measurement by short pulses, we scale down the Hall bar size to 5 μm × 15 μm for shorter domain wall propagation length. The small Hall bar is shown in Figure 5.2(b).

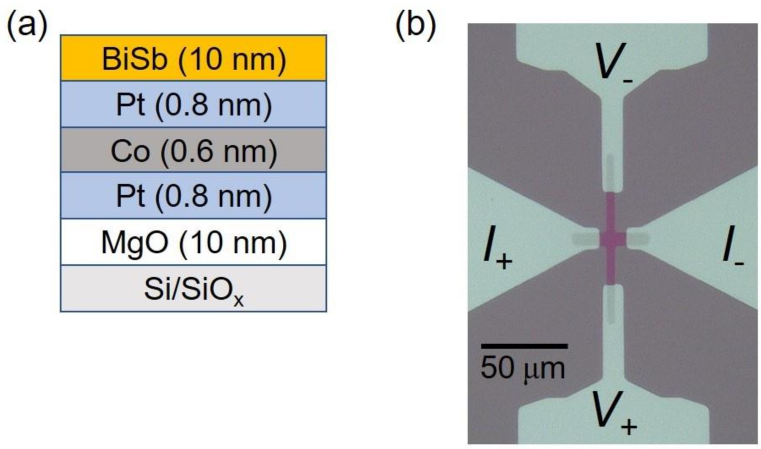

Figure 5.2 **(a)** Schematic structure of our samples. **(b)** Optical image of 5 μm × 15 μm Hall bar

5.3 Spin Hall angle evaluation

Figure 5.3(a) and 5.3(b) show the anomalous Hall resistance R_H of the sample measured with a sweeping external field applied perpendicular to the film plane (Figure 5.3(a)) and in-plane along the current direction (Figure 5.3(b)), respectively, which confirm PMA of CoPt. In Fig 5.3(b), we show the fitting curve to the data by the function R_{H} = $R_{\mathrm{H}}(0)\sqrt{1-\left(\frac{H_x}{H_u}\right)^2}$, in which $R_{\mathrm{H}}(0)$ is the Hall resistance at zero field, H_x is the external field, and H_u is the PMA field. From this fitting, we obtain a PMA field of 4.5 kOe, which is comparable to that of CoFeB/MgO. The conductivity of the BiSb top layer is evaluated as 1.0×10^5 $\Omega^{-1}\mathrm{m}^{-1}$ by the parallel resistor model. While this value is smaller than that of MBE-grown BiSb (2.5×10^5 $\Omega^{-1}\mathrm{m}^{-1}$) [10], it is larger than that of MBE-grown Bi_2Se_3 (5.6×10^4 $\Omega^{-1}\mathrm{m}^{-1}$) [11] and MBE-grown $(BiSb)_2Te_3$ (1.8×10^4 $\Omega^{-1}\mathrm{m}^{-1}$) [12], and helps reduce the shunting current to other metallic layers significantly. Indeed, we estimate that 31% of the applied current flows into the BiSb.

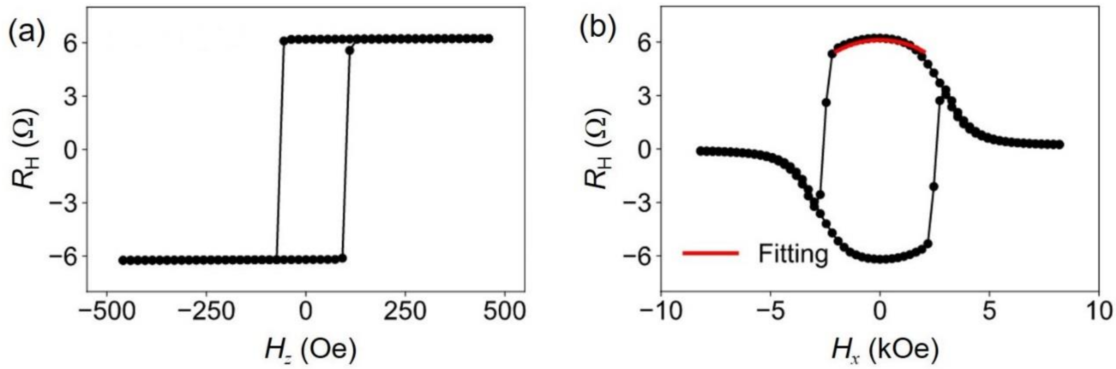

Figure 5.3 **(a)(b)** Hall resistance of a Hall bar device measured with magnetic field applied perpendicular to the film plane and in-plane along the current direction.

We performed high-field second harmonic Hall measurements to characterize the spin Hall effect of BiSb [13-15]. An alternating current (AC) $J = J_0\sin\omega t$ ($\omega/2\pi = 259.68$ Hz) was applied to the Hall bar under a sweeping external field applied along the current direction (x direction). The 2$^{\mathrm{nd}}$ harmonic Hall resistance $R_{\mathrm{H}}^{2\omega}$, originated from the oscillation of the net magnetic moment under the SOT magnetic fields, are measured by the lock-in amplifier at different current density. Figure 5.4(a) shows $R_H^{2\omega}$– H_x curves measured at several BiSb current density J^{BiSb}. A representative fitting by equation [15]

$$R_H^{2\omega} = \frac{R_H}{2}\frac{H_{AD}}{H_x - H_u(H_x/|H_x|)} + R_{thermal}\frac{H_x}{|H_x|} \qquad (5.1)$$

to the experimental data at $J^{BiSb} = 2.48\times10^5$ Acm^{-2} is shown in Figure 5.4(a) (dashed curves). H_{AD} yielded from the fittings is plotted as a function of J^{BiSb} in Figure 5.4(b). The effective spin Hall angle θ_{SH}^{eff} is then calculated from $\theta_{SH}^{eff} = \frac{2e}{\hbar} M_{CoPt} t_{CoPt} \frac{H_{AD}}{J^{BiSb}} \sim 2.4$, where M_{CoPt} = 500 emu/cc is the saturation magnetization of CoPt, measured by SQUID. Since the top Pt (0.8 nm) layer induces some spin loss of the spin current injected from BiSb, the effective spin Hall angle θ_{SH}^{eff} of BiSb is smaller than the real spin Hall angle θ_{SH} by $\theta_{SH}^{eff}=\theta_{SH}$*sech($t_{Pt}/\lambda_{SF}^{Pt}$), where t_{Pt} = 0.8 nm is the top Pt layer thickness and λ_{SF}^{Pt} is the diffusion length of Pt. If we use the spin diffusion length λ_{SF}^{Pt} = 1.1 nm for Pt reported in Pt/Bi_xTe_{1-x} [16], we expect that θ_{SH} = 3.1.

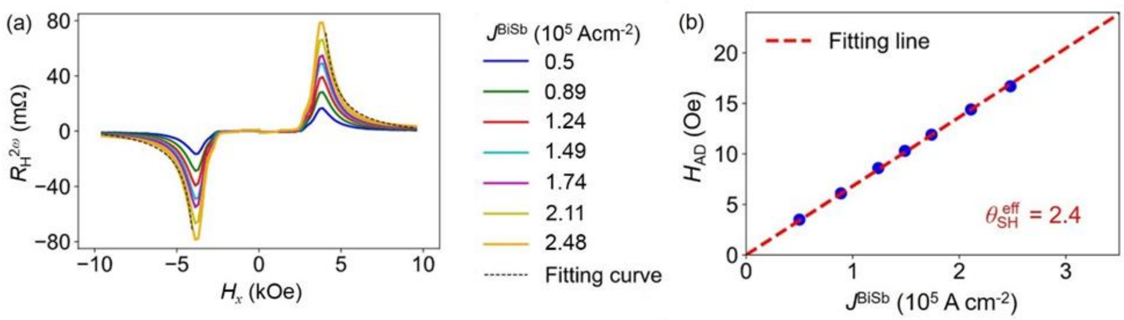

Fig. 5.4 **(a)** High-field 2nd harmonic Hall resistance as a function of the in-plane external magnetic field H_x at different BiSb current densities. Dashed curves are theoretical fitting using Eq. 5.1 to data at J^{BiSb} = 2.48×10^5 Acm^{-2}. **(b)** Antidamping-like field H_{AD} as a function of J^{BiSb}.

To further confirm that the observed large SOT effect is from the contribution of BiSb, we prepared a control sample MgO(10) / Pt(0.8) / Co(0.6) / Pt(0.8) / Ta (6) (units in nanometer). We used the second harmonic measurement to evaluate the spin Hall angle. The results are shown in Figure 5.5. For this control sample, the Hall resistance R_H = 3 Ω, saturation magnetization M_{CoPt} = 500 emu/cc, anisotropy field H_u = 1.8 kOe, and current distribution is 50% for Ta. From the second harmonic measurements, we obtained θ_{SH}^{eff} = -0.06 for Ta.

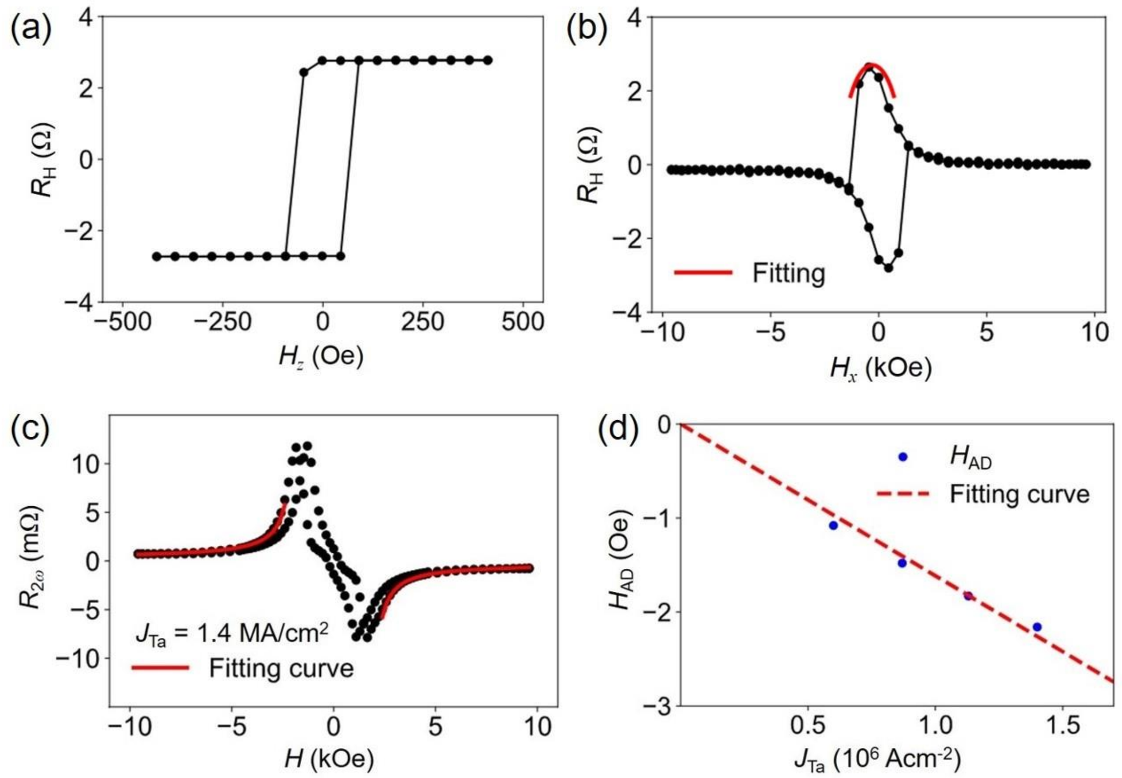

Figure 5.5 **(a)(b)** Hall resistance of a control sample MgO(10) / Pt(0.8) / Co(0.6) / Pt(0.8) / Ta (6), measured with magnetic field applied perpendicular to the film plane and in-plane along the current direction. **(c)** Representative second harmonic Hall resistance as a function of in-plane external field. Red curves are theoretical fitting using Eq. 5.1. **(d)** Antidamping-like field H_{AD} as a function of J_{Ta}.

5.4 SOT magnetization switching by DC and pulse currents

We demonstrate SOT magnetization switching of CoPt by pulse currents. Figure 5.6 shows the SOT magnetization switching curves by DC currents, with an external field H_x = ±183 Oe applied along the x direction to break symmetry. The switching direction is reversed when the external magnetic field direction is reversed, which is consistent with the characteristic of SOT. The amplitude of the Hall resistance switching is consistent with that of hysteresis curve in Figure 5.3, indicating full magnetization switching. The threshold current density J_{th}^{BiSb}, at which R_H changes sign, is 1.0×10^6 Acm^{-2}. Thanks to the high conductivity of BiSb, the current density in the whole structure is as low as 2.46×10^6 Acm^{-2}.

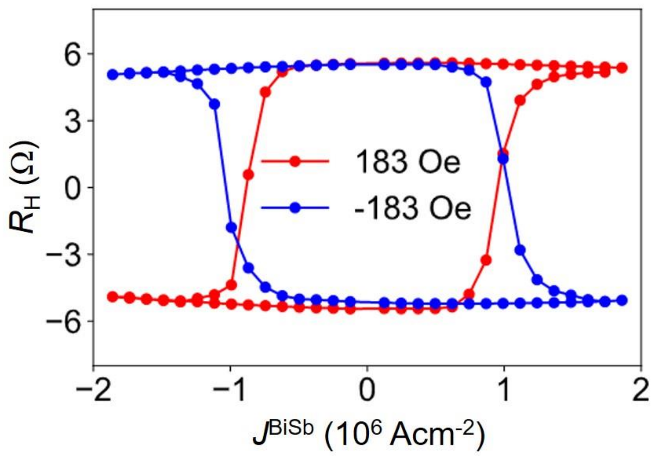

Figure 5.6 SOT magnetization switching by DC currents. Switching loops measured under an in-plane magnetic field applied along +x (red) direction and -x (blue) direction.

Figure 5.7 shows the SOT magnetization switching curves at different pulse width with an external field H_x = ±183 Oe along the x direction. The full SOT magnetization switching can also be achieved by pulse currents. The threshold current density J_{th}^{BiSb}, at which R_H changes sign, is 2.3×10^6 Acm^{-2} at pulse width of 100 μs. We then plot J_{th}^{BiSb} as a function of pulse width τ for forward (blue) and backward (red) SOT switching in Figure 5.8, and fit the data by the thermal activation model $J_{\mathrm{th}}^{\mathrm{BiSb}}=J_0^{\mathrm{BiSb}}\times\left[1-\frac{1}{\Delta}\ln\frac{\tau}{\tau_0}\right]$ (solid lines) [17], where J_0^{BiSb} is the zero-Kelvin threshold switching current density, Δ is the thermal stability factor, and $1/\tau_0 = 1$ GHz ($\tau_0 = 1$ ns) is the attempt switching frequency. From the fitting, we obtain $\Delta = 32$, which is slightly lower than $\Delta \sim 38$ in CoFeB/MgO. The Δ can be further improved by ferromagnetically coupling CoPt to CoFeB/MgO through a thin Ru layer, thus we expect CoPt/Ru/CoFeB/MgO can yield a total $\Delta = 70$ for 10-year thermal stability [8]. Figure 5.9 shows the field dependence of the SOT magnetization switching at $\tau = 100$ μs. Note that the amplitude of the switching loop R_{H} at each H_x is consistent with $R_{\mathrm{H}} = R_{\mathrm{H}}(0)\sqrt{1-\left(\frac{H_x}{H_u}\right)^2}$, where $R_{\mathrm{H}}(0) = 6.1\ \Omega$ and $H_k = 4.5$ kOe. These results demonstrated the full switching as well as the consistency of large PMA.

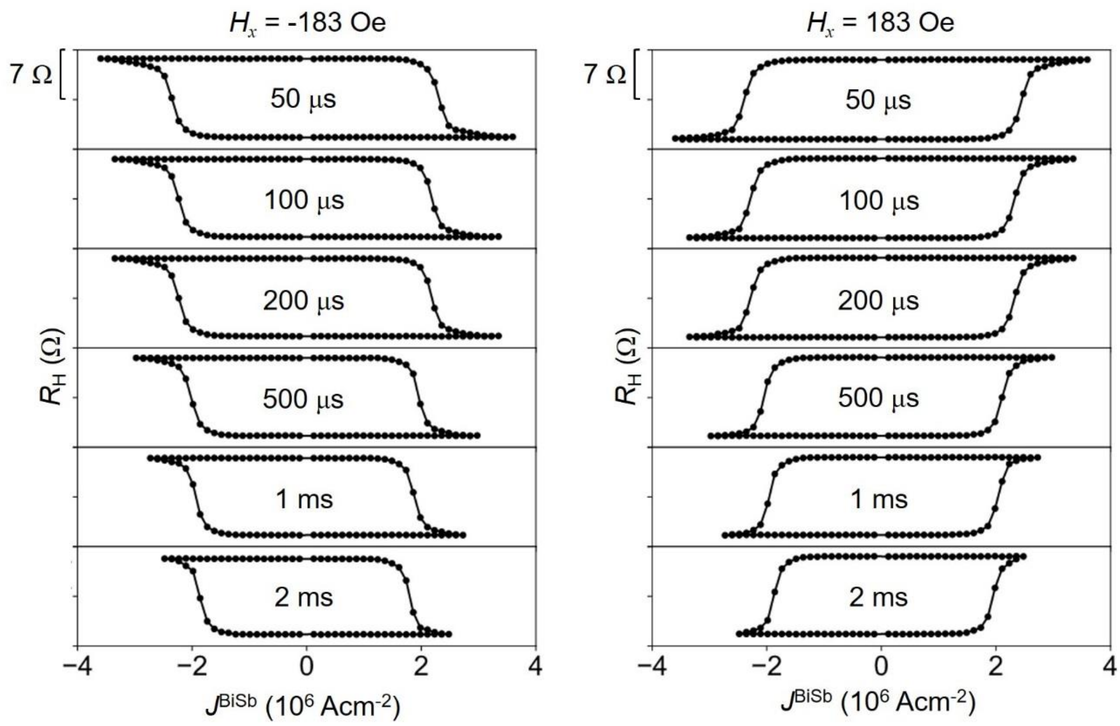

Fig. 5.7 SOT switching loops at different pulse width τ, measured under a bias in-plane magnetic field applied along the $+x$ (left) direction and $-x$ (right) direction.

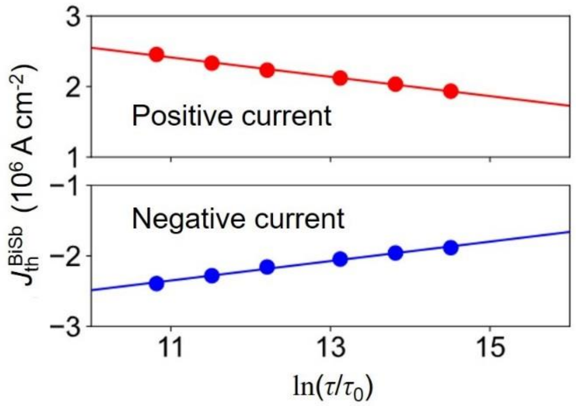

Figure 5.8 Threshold current density J_{th}^{BiSb} as a function of τ.

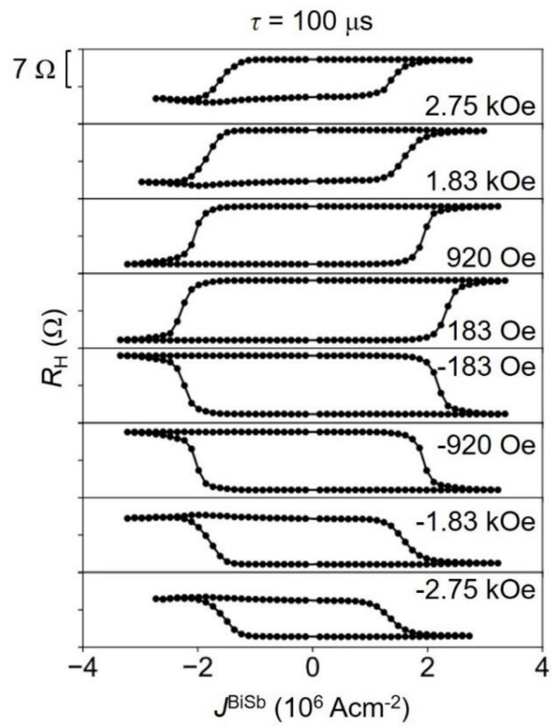

Figure 5.9 Bias field dependence of SOT switching loops at τ = 100 μs.

In Figure 5.10, we demonstrate robust SOT switching by applying repeatedly 100 μs pulses currents of $\pm 2.9\times 10^6$ Acm^{-2}, as the top panels in Figure 5.10 for 5 loops, at bias field of ± 183 Oe. We observed a robust full SOT switching with R_H depending on the direction of pulse current and H_x.

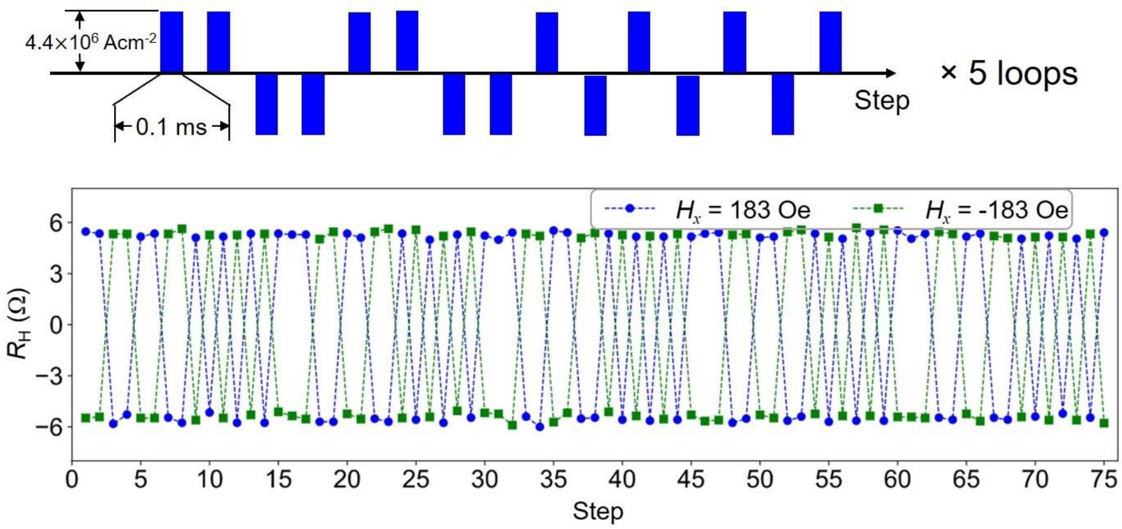

Figure 5.10 Robust SOT magnetization switching by 100 μs pulse currents.

In order to further confirm the large SOT effect of BiSb, we also perform the SOT magnetization switching for the control sample MgO(10) / Pt(0.8) / Co(0.6) / Pt(0.8) / Ta(6) (thickness in nm). In the control sample, the magnetization is switched by only 20% by a threshold current density 8×10^6 A/cm^2, as shown in Figure 5.11. The current density is more than 3 times larger than that of BiSb despite the control sample has a much smaller H_u. Because the control sample uses the same Pt/Co/Pt multilayers, the effect of both Ta and Pt can be included. Together with the second harmonic measurements, it can be confirmed that the SOT effect in our work is from the contribution of BiSb, which can generate a much higher SOT efficiency than heavy metals.

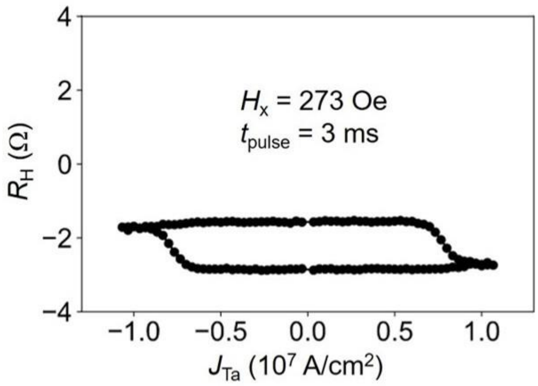

Figure 5.11 SOT switching loop in the control sample MgO/Pt/Co/Pt/Ta by a pulse current t_{pulse} = 3 ms under a bias field of 273 Oe.

Finally, we performed the SOT magnetization switching measurements by shorter pulses down to 100 ns. Figure 5.12(a) shows the anomalous Hall resistance of a small Hall bar device. The SOT magnetization switching loops at 500 ns, 200 ns and 100 ns (which is the limit of our signal generator) are shown in Figure 5.12(b). We achieved full magnetization switching with J_{th}^{BiSb} = 5.4 × 10^6 Acm^{-2} at 100 ns under H_x = 183 Oe, which is still one order of magnitude smaller than that of heavy metals.

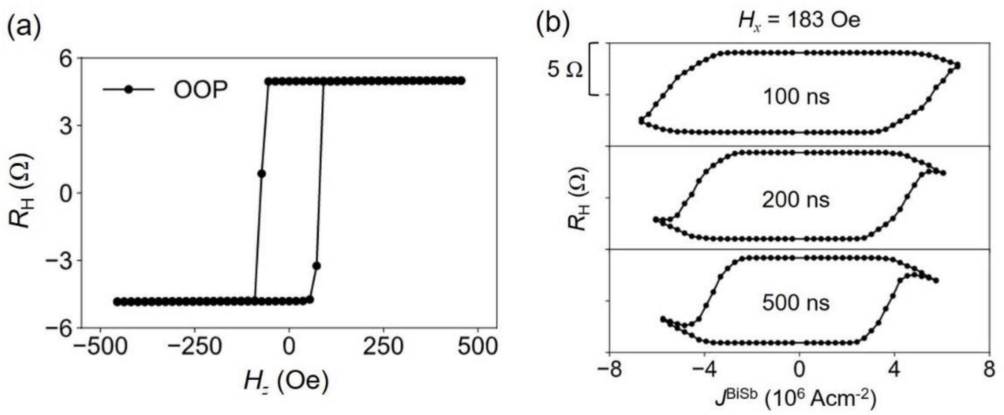

Figure 5.12 **(a)** Hall resistance of a 5 μm × 15 μm Hall bar device measured with a perpendicular magnetic field. **(b)** Switching loops by 500 ns, 200 ns and 100 ns pulse currents measured under H_x = 183 Oe.

5.5 Discussion

In summary, we have investigated SOT performance of BiSb topological insulator in junctions with CoPt with large PMA on MgO buffer, deposited fully by the sputtering technique on oxidized Si substrates. Although the CoPt layer has a large PMA field of 4.5 kOe, we were able to perform SOT switching with low current densities and fast pulse down to at least 100 ns. The sputtered BiSb layer has a relatively high conductivity of 1.0×10^5 $\Omega^{-1}m^{-1}$ compared with other MBE-grown TIs, and a large effective spin Hall angle of 2.4. Table 5.1 compares the normalized power consumption between Ta, Pt, W and sputtered BiSb on SiO_x. One can see that the power consumption of sputtered BiSb on SiOx is much smaller than that of heavy metals, thanks to its high spin Hall angle relatively high conductivity. Our work shows that it is possible to implement ultralow power SOT-MRAM and other SOT devices, such as spin Hall oscillator [18], using BiSb on Si substrates.

SOT Materials	$\lvert\theta_{SH}\rvert$	σ ($\Omega^{-1}m^{-1}$)	P_n
Ta	0.15	5.3×10^5	1
Pt	0.08	4.2×10^6	3.6×10^{-1}
W	0.4	4.7×10^5	1.6×10^{-1}
$Bi_{0.85}Sb_{0.15}$ (Sputtered on SiOx)	3.1	1.0×10^5	6.5×10^{-3}

Table 5.1 Spin Hall angle θ_{SH}, electrical conductivity σ, spin Hall conductivity σ_{SH} , and SOT normalized power consumption P_n of Ta, Pt, W, and sputtered BiSb on Si/SiOx substrates.

References

[1] Mahmoudi H., et al. Implication logic gates using spin-transfer-torque-operated magnetic tunnel junctions for intrinsic logic-in-memory. Solid-State Electron. 84, 191 (2013).

[2] Apalkov D., et al. Magnetoresistive random access memory. Proc. IEEE 104, 1796 (2016).

[3] Torrejon J., et al. Neuromorphic computing with nanoscale spintronic oscillators. Nature 547, 428 (2017).

[4] Romera M., et al. Vowel recognition with four coupled spin-torque nano-oscillators. Nature 563, 230 (2018).

[5] Borders W. A., et al. Integer factorization using stochastic magnetic tunnel junctions. Nature 573, 390 (2019).

[6] Khang N. H. D., et al. Ultralow power spin–orbit torque magnetization switching induced by a non-epitaxial topological insulator on Si substrates. Sci. Rep. 10, 12185 (2020).

[7] Ikeda S., et al. Perpendicular-anisotropy CoFeB-MgO based magnetic tunnel junctions scaling down to 1X nm. 2014 IEEE International Electron Devices Meeting (IEDM). IEEE, 2014.

[8] Sato H., et al. Perpendicular-anisotropy CoFeB-MgO magnetic tunnel junctions with a MgO/CoFeB/Ta/CoFeB/MgO recording structure. Appl. Phys. Lett. 101, 022414 (2012).

[9] Grimaldi E., et al. Single-shot dynamics of spin–orbit torque and spin transfer torque switching in three-terminal magnetic tunnel junctions. Nat. Nanotechnol. 15, 111 (2020).

[10] Khang N. H. D. et al, A conductive topological insulator with large spin Hall effect

for ultralow power spin–orbit torque switching. Nat. Mater. 17, 808 (2018).

[11] Mellnik A. R., et al. Spin-transfer torque generated by a topological insulator. Nature 511, 449 (2014).

[12] Wu H., et al. Room-Temperature Spin-Orbit Torque from Topological Surface States. Phys. Rev. Lett. 123, 207205 (2019).

[13] Hayashi M., et al. Quantitative characterization of the spin-orbit torque using harmonic Hall voltage measurements. Phys. Rev. B 89, 144425 (2014).

[14] Kim J., et al. Layer thickness dependence of the current-induced effective field vector in Ta | CoFeB | MgO. Nat. Mater. 12, 240 (2013).

[15] Wu H., et al. Spin-Orbit Torque Switching of a Nearly Compensated Ferrimagnet by Topological Surface States. Adv. Mater. 31, 1901681 (2019).

[16] Chen T., et al. Efficient spin–orbit torque switching with nonepitaxial chalcogenide heterostructures. ACS Appl. Mater. Interfaces 12, 7788 (2020).

[17] Koch R. H., et al. Time-resolved reversal of spin-transfer switching in a nanomagnet. Phys. Rev. Lett. 92, 088302 (2004).

[18] Shirokura T., et al. Bias-field-free spin Hall nano-oscillators with an out-of-plane precession mode. J. Appl. Phys. 127, 103904 (2020).

Chapter 6 Structure analysis by transmission electron microscope

6.1 Introduction

In previous chapters, we demonstrated that BiSb can be deposited by sputtering deposition with large spin Hall angle and high electrical conductivity, and realized low energy SOT magnetization switching in all-sputtered BiSb / CoPt multilayers on sapphire and Si/SiO_x substrate. However, there is still room for improvement in BiSb deposition by sputtering. Ideally, material for spin Hall layer in realistic SOT-MRAM requires a spin Hall angle larger than 10. The spin Hall angle of sputtered BiSb on Si/SiO_x substrates is 3.1, which is much smaller than that of MBE-grown ideal BiSb, as well as that of sputtered BiSb on sapphire substrates. It is required to robustly grow BiSb with large spin Hall angle for future SOT-MRAM.

In this chapter, we discuss the reason for the relatively small spin Hall angle in sputtered BiSb, and the possible solution to improve it. It is known that most TIs have low thermal and chemical stability [1-3]. During the heating process, the Sb atoms are easy to diffuse to the FM layers. Since the spin Hall angle becomes maximum when the concentration of Sb is 15%, it will decrease if the BiSb lose Sb atoms [4]. Moreover, the Sb diffusion to FM layers will lead to a drastic decrease of PMA. In the sample we studied in Chapter 4, the as-grown CoPt has a large PMA field of 15 kOe, but it is reduced to 5.2 kOe after device fabrication process. Therefore, the Sb diffusion will make it difficult to obtain FM layers with large PMA, which is important SOT-MRAM. In this work, we use scanning transmission electron microscope (STEM) and EDX spectroscopy to analyze the elements distribution in different structures. Because of the limitation of TEM schedules, we measure some different samples to those in previous chapters. Nevertheless, the results can still provide some guidance for our future works.

6.2 Characterization technique: transmission electron microscope

TEM is the equipment to observe a sample at atomic resolution. In the measurement process, an accelerated and focused electron beam is transmitted through a thin specimen. Thanks to the short de Broglie wavelength of electrons, TEM can provide much higher resolution than optical microscopes. STEM combines the principles of SEM into TEM. It can collect the signals that cannot be correlated in TEM, including secondary electrons, scattered beam electrons, characteristic X-rays, and electron energy loss. Especially, X-ray is emitted during the collision process between electrons and specimen, whose energy is characteristic of the elemental composition of the sample. EDX spectrometer is used to count and sort characteristic X-rays according to their energy. It is an important tool in this work to analyze the element composition and distribution in this work.

6.3 Sample growth and specimen processing

We prepared 2 groups of control experiments. In the first group, we use the $(Co/Pt)_2$/BiSb (top) on sapphire in Chapter 4, and another BiSb (10) (bottom) / Pt (1) / Co (1) / Pt (1) for comparison (unit in nm). These samples are denoted as sample 1A and 1B respectively. The magnetization of 1B is in-plane. In the second group, two $[Co (0.9) / Gd (0.4)]_3$ / Pt (1) / BiSb (10) (top) samples on Si/SiO_x substrates are prepared, denoted as sample 2A and 2B respectively. In sample 2A, the $(Co/Gd)_3$/Pt multilayers were taken out from the deposition chamber and exposed to the air for 30 minutes before BiSb was deposited. Both samples in group 2 are capped by 1 nm Pt to prevent the oxidation.

Anomalous Hall effect measurements show that sample 2A has PMA while the magnetization of sample 2B is in-plane. All samples are deposited by DC magnetron sputtering. The structures of samples in this chapter are illustrated in Figure 6.1.

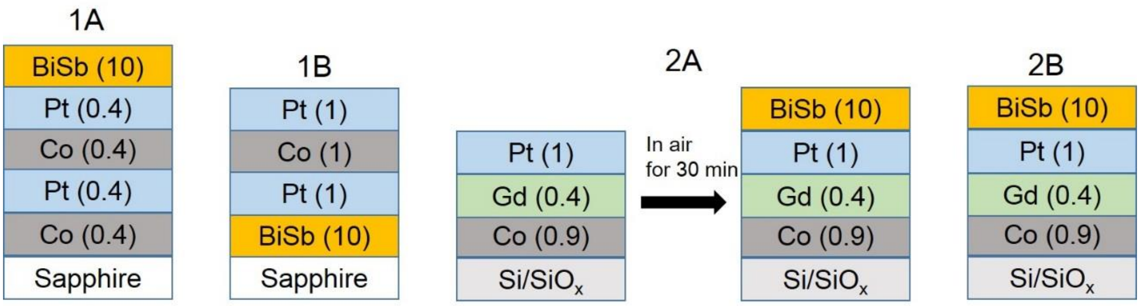

Figure 6.1 Schematic of sample structures in this work

Specimen processing by focused ion beam

Before the observation by TEM, the samples were fabricated to thin specimens, which are suitable for TEM observation, by a focused ion beam (FIB) - Scanning Electron Microscope (SEM) mixed system. A FIB uses a beam of ions, which can be focused on the surface, to image the sample. The ion beam with high energy can also mill the sample with nanometer precision under the observation by SEM and FIB. For TEM observation, milled specimen needs to be attached to an appropriative pillar. The milling process is described as follows.

(1) Deposit 1 μm Pt on the surface to protect the surface from the damage by the ion beam.

(2) Mill three sides and the bottom of the desired 3 μm×15 μm region.

(3) Insert the needle, contact it with the end of the specimen, and attach them together by Pt deposition (Figure 6.2(a)).

(4) Cut the fourth side, and retract the needle. Now the specimen is attached with the needle.

(5) Take out the remaining raw sample, and put the appropriative holder into the chamber.

(6) Insert the needle with specimen again, adjust the position, and contact the specimen with the pillar on the holder. Attach the specimen with the pillar by Pt deposition (Figure 6.2(b)).

(7) Mill the connection between the specimen and the needle, and retract the needle.

(8) Mill both sides of the specimen to make it thinner (Figure 6.2(c)). We need to mill it into a fusiform, because this shape can keep the specimen most stable in STEM when it is irradiated by electrons. We mill it narrower and narrower, and evaluate the thickness by the contrast. The process can be finished if the FIB image becomes transparent, and the pillar with specimen can be taken out from the chamber. The specimen is finally milled to 10-nm wide.

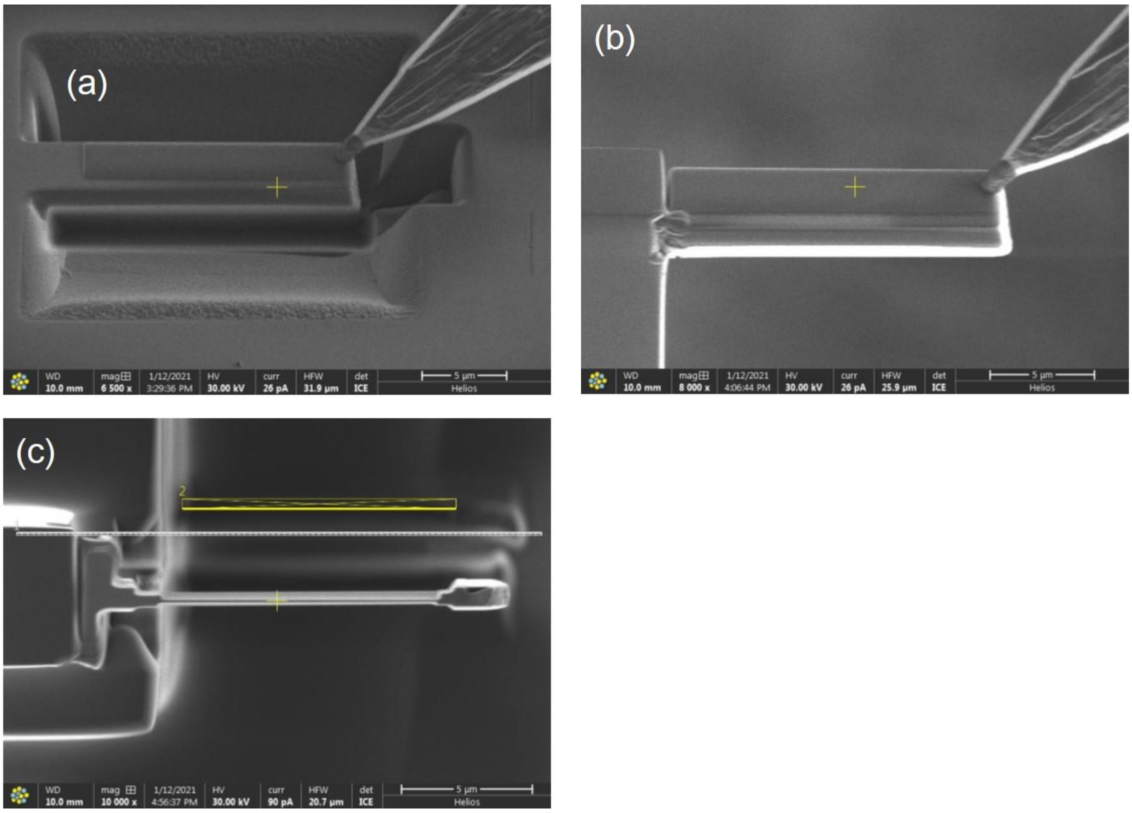

Figure 6.2 FIB images of specimen preparation for TEM observation

6.4 Experimental results

Figure 6.3(a) and 6.3(b) shows the TEM image of sample 1A and 1B with their nano-beam diffraction patterns, respectively. For sample 1A, because the thickness of Co and Pt layers is 0.4 nm, there is approximately only 1 layer of atoms in each layer. It is easy that the CoPt multilayer becomes alloy, which can be observed in the TEM image. Through the nano-beam diffraction patterns, it can be known that the CoPt is textured. In BiSb layer, the first 2 to 3 nm BiSb has some crystal disorder, which absorbs the lattice mismatch with CoPt. When the thickness exceeds 2 nm, BiSb become polycrystal, with different crystal ordering in different region. The polycrystallinity is confirmed by the nano-beam diffraction patterns, although BiSb(110) is the dominant phase. These results are consistent with the XRD spectrum in Chapter 4 with multi XRD phases. Note that BiSb deposited either directly on sapphire substrate (introduced in Chapter 3) or on CoPt has 2 nm crystal disorder, and crystal ordering improves rapidly when the thickness exceed 2 nm. These results demonstrate the robustness of BiSb by sputtering deposition on different interface.

For sample 1B, the Co-Pt interface is clear because the Co and Pt layers are relatively thick. However, the Co and Pt layers are weakly polycrystal according to the TEM image and nano-beam diffraction patterns. This is a possible reason that the magnetization of this sample does not have PMA. The BiSb layer directly deposited on sapphire substrate has high crystal ordering, which is consistent with the results of single layer BiSb in Chapter 3. However, the crystallinity becomes weak in part of the sample when the thickness exceeds 5 nm. This change can be demonstrated through the comparison of nano-beam diffraction patterns between BiSb near the substrate and near CoPt.

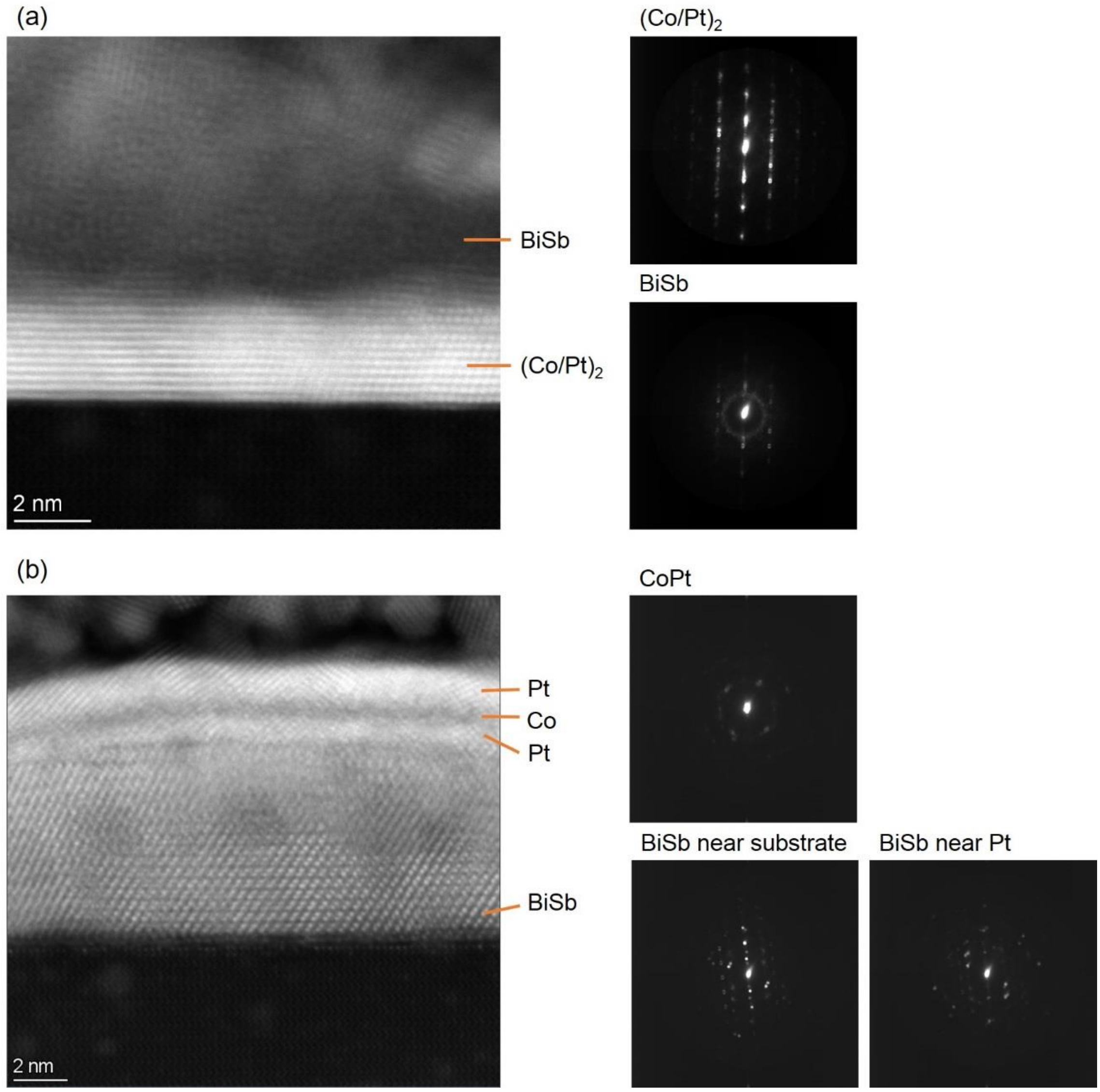

Figure 6.3 TEM images with nano-beam diffraction patterns for **(a)** sample 1A and **(b)** sample 1B.

Figure 6.4(a) and 6.4(b) show the EDX spectroscopy of sample 1A and 1B, respectively. We mapped the concentration of Sb atoms in CoPt layers. The concentration of Sb in CoPt layer is 5% in sample 1A, while that is 12% in sample 1B. The large Sb diffusion to CoPt is another possible reason that the PMA of CoPt in sample 1B was not realized. On the other hand, from the crystal quality, the BiSb in sample 1B is expected have larger spin Hall angle than that in sample 1A because of its higher crystal ordering. On the contrary, the spin Hall angle of sample 1A is 10.7, while that of sample 1B is only 1. This phenomenon can be explained by the EDX mapping results. In sample 1B, there is a massive Sb loss in BiSb, which makes the Sb concentration much smaller than 15% in BiSb layer. Because the spin Hall angle is largest when the Sb concentration is 15%, and rapidly decreases when either the Sb concentration increases or decreases, the sample 1A has large spin Hall angle with Sb concentration close to 15%. Furthermore, there is significant Pt diffusion into BiSb in sample 1B.

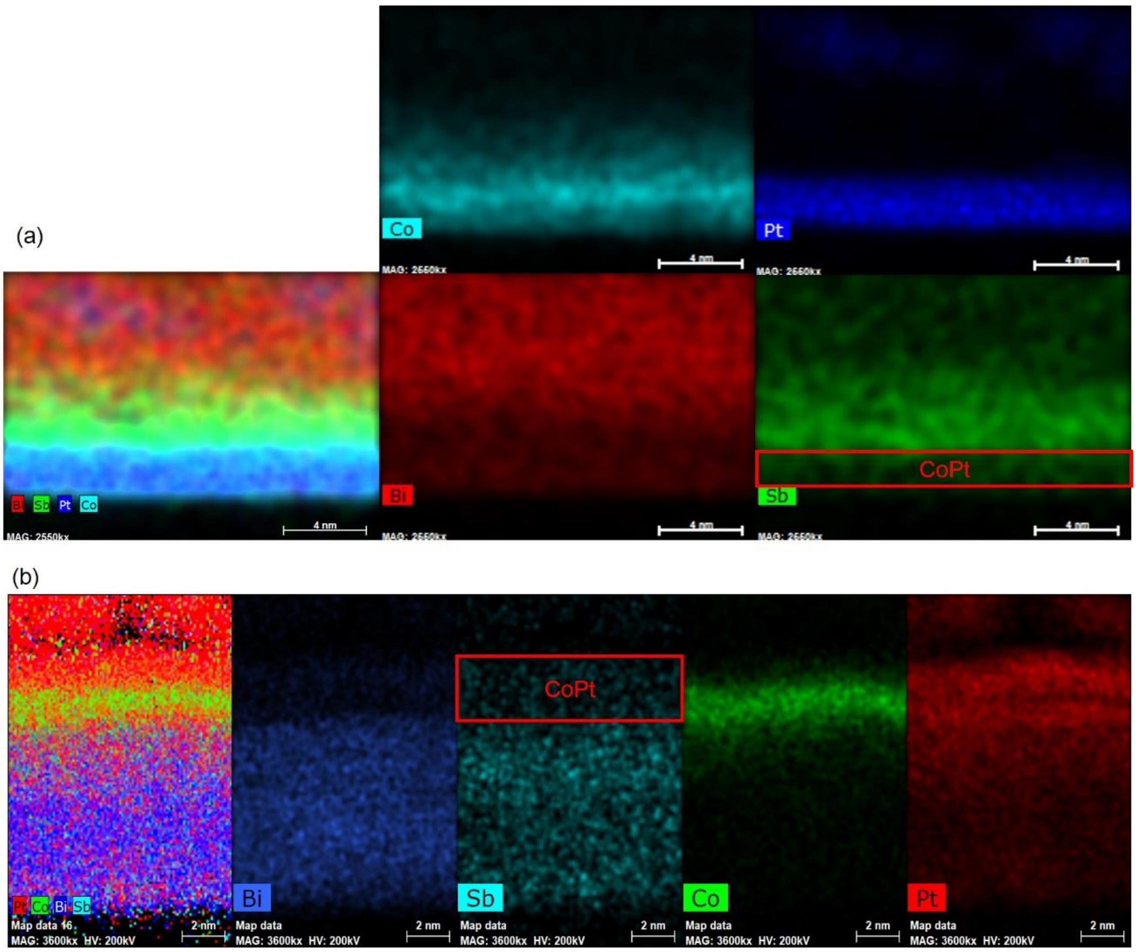

Figure 6.4 Distribution of each element by EDX mapping for (a) sample 1A and (b) sample 1B. Sb diffusion to CoPt layer is marked in the figures.

Figure 6.5(a) and 6.5(b) show the TEM image of sample 2A and 2B, respectively. The TEM images indicate the weak crystal ordering in the CoGd layer. However, BiSb becomes polycrystal after a thin crystal ordering in both samples on different BiSb-Pt interface (the difference will be explained below). These results provide another evidence for the robustness of BiSb deposition by sputtering. In this group, sample 2A with $(Co/Gd)_3/Pt$ exposed to air has PMA, while sample 2B has in-plane magnetization. We investigate the difference by analyzing the element distribution in each layer. In the STEM image of sample 2A, there is one more layer between BiSb and Pt, which does not exist in sample 2B. This layer is likely oxidized Pt due to exposure in air. This oxidized layer can become a barrier to prevent the Sb diffusion from BiSb to CoGd, and protects the PMA of CoPd.

This hypothesis was confirmed by the EDX spectroscopy. Figure 6.6(a) and 6.6(b) show the EDX spectroscopy of sample 2A and 2B, respectively. We mapped the element distribution in the Pt and CoGd layer. Table 6.1 shows the concentration of Sb and O atoms in Pt and CoGd layer. The O concentration in CoGd layer approaches to 50% in both samples, meaning that CoGd is oxidized by oxygen from SiO_x. However, the O concentration in Pt layer are quite different. In sample 2A, it is nearly double than that in sample 2B. The high O concentration in the Pt layer in sample 2A can also be confirmed by the EDX mapping. The oxidized part of Pt is marked red in Figure 6.6(a). This result is consistent with the TEM images, confirming the existence of oxidized Pt layer in sample 2A. Furthermore, the Sb concentration in CoGd is 0.7% and 3%, and that in Pt is 2% and 11% in sample 2A and 2B, respectively, indicating that the oxidized Pt layer can suppress the Sb diffusion to Pt and then CoGd. We conclude that the less diffusion of Sb protects the PMA of the CoGd layer in sample 2A.

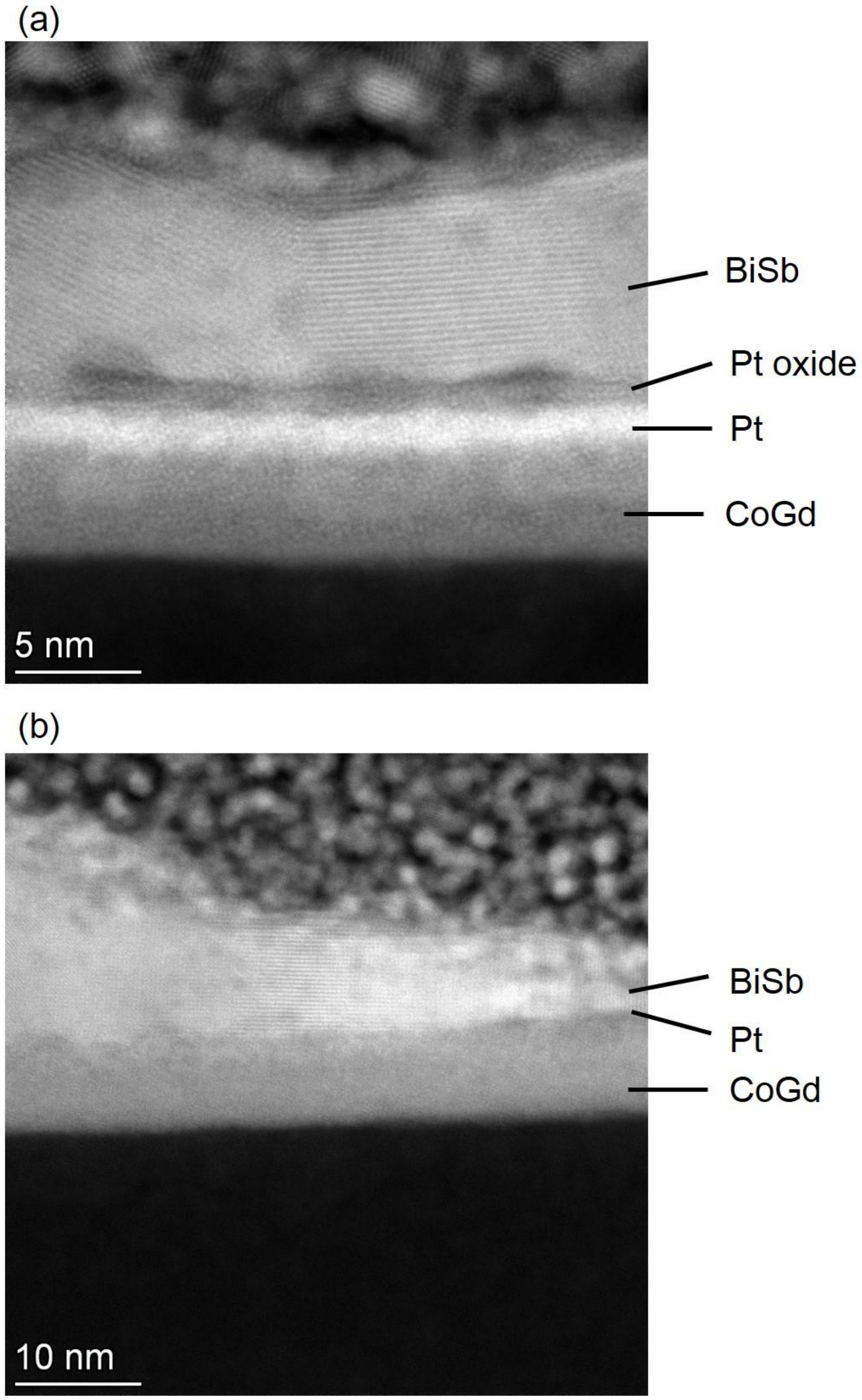

Figure 6.5 TEM images for **(a)** sample 2A and **(b)** sample 2B.

Sample 2A		Sample 2B	
Sb in Pt	2%	Sb in Pt	11%
Sb in CoGd	0.7	Sb in CoGd	3%
O in Pt	43%	O in Pt	27%
O in CoGd	49%	O in CoGd	46%

Table 6.1 Concentration of Sb and O atoms in Pt and CoGd layer in sample 2A and 2B.

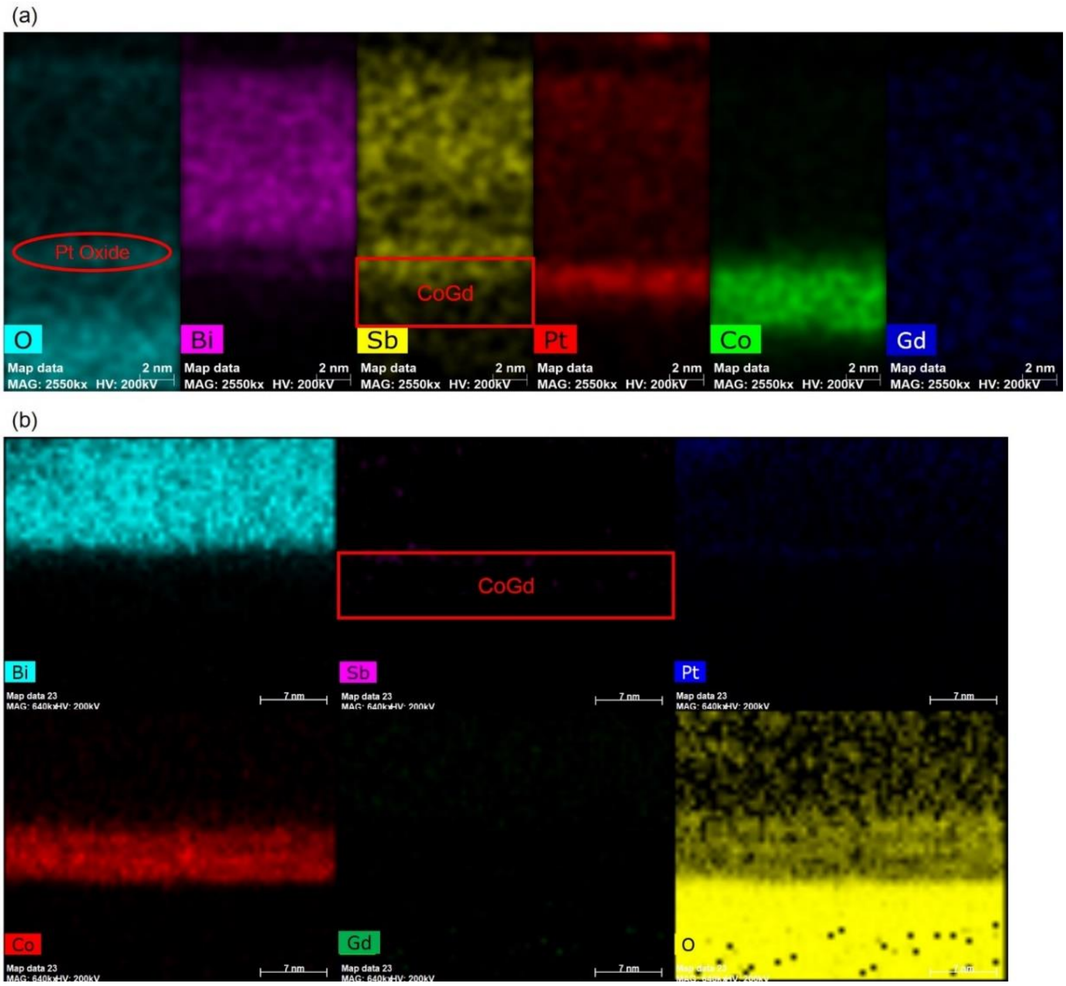

Figure 6.6 Distribution of each element by EDX mapping for **(a)** sample 2A and **(b)** sample 2B. Sb diffusion to CoGd layer in both samples, and oxidized Pt layer in sample 2A is marked in the figures.

6.5 Discussion

The studies in this chapter can provide some guidance to obtain BiSb/FM heterostructures with large spin Hall angle and large PMA. Firstly, the Sb loss in BiSb should be prevented in order to keep the Sb concentration unchanged. On the other hand, the Sb diffusion to FM layers is confirmed to be the reason that reduces or destroys PMA. If we directly deposit BiSb on FM layers, the percentage of Sb diffused to FM layers can be different in different samples, making the spin Hall angle unstable. Using the interlayer between BiSb and FM layers to prevent the Sb diffusion is a solution to this problem. NiO is a good choice as the material for the interlayer, because there are reports that NiO can enhance the SOT exerted on FM layers [5, 6]. Recently, by using a NiO interlayer, Sasaki *et al.* [7] has demonstrated BiSb/FM heterostructure with a large spin Hall angle of 10. This robustness is very important for mass production of SOT-MRAM.

References

[1] Zhu L., et al. Spin-orbit torques in heavy-metal–ferromagnet bilayers with varying strengths of interfacial spin-orbit coupling. Phys. Rev. Lett. 122, 077201 (2019).

[2] Zhu L., et al. Effective spin-mixing conductance of heavy-metal–ferromagnet interfaces. Phys. Rev. Lett. 123, 057203 (2019).

[3] Zhu L., et al. Maximizing spin-orbit-torque efficiency of Pt/Ti multilayers: Trade-off between intrinsic spin Hall conductivity and carrier lifetime. Phys. Rev. Appl. 12, 051002 (2019).

[4] Ichimura M., et al. BiSb トポロジカル絶縁体のスピンホール効果の Sb 組成比依存性. 12p-S302-5, JSAP autumn meeting 2021.

[5] Wang H., et al. Spin transport in antiferromagnetic insulators mediated by magnetic

correlations. Phys. Rev. B 91, 220410 (2015)..

[6] Wang Y., et al. Magnetization switching by magnon-mediated spin torque through an antiferromagnetic insulator. Science 366.6469, 1125 (2019).

[7] Sasaki J., et al. Highly efficient spin current source using BiSb topological insulator / NiO bilayers. 11a-S302-8, JSAP autumn meeting 2021.

Chapter 7 Conclusion

In Chapter 1, the background of this research was introduced. MRAM is promising for its non-volatility compared with traditional charge-based memories such as SRAM and DRAM. MRAM have so far evolved from toggle MRAM, spin-transfer-torque MRAM to SOT-MRAM. The requirements for the spin Hall layer of SOT-MRAM are identified as (1) large spin Hall angle, (2) high electrical conductivity, and (3) deposition by industrial friendly techniques, such as sputtering deposition. These requirements inspire the motivation of this work.

In Chapter 2, the fundamental physics of this work is introduced. TI BiSb is considered as the best candidate for spin current source of SOT-MRAM. As TI, BiSb has the protected topological surface states with strong SOI. Therefore, in BiSb / FM heterostructures, BiSb can generate a large SOT by SHE, which can switch the magnetization of the FM layer.

In Chapter 3, various single layer BiSb thin films were grown on sapphire substrate by sputtering deposition at different growth condition. It was demonstrated that the sputtered BiSb thin films have good crystal quality and high electrical conductivity, which are promising for MRAM applications. By XRD analysis of sputtered BiSb thin films, it was shown that BiSb thinner than 30 nm with strong (001) orientation can be obtained. The electrical conductivity of the BiSb thin films exceeds $1.5 \times 10^5\ \Omega^{-1}m^{-1}$ at room temperature. By measuring the temperature dependence of the resistivity, the surface states were confirmed in sputtered BiSb. The works in this chapter demonstrate that it is possible to obtain BiSb thin film with high quality close to that of MBE grown ones.

In Chapter 4, the spin Hall effect and SOT magnetization switching characteristics were investigated in an all-sputtered BiSb – $(Co/Pt)_2$ multilayers deposited by DC magnetron sputtering on sapphire substrates. It was shown that the sputtered BiSb thin films with the dominant (110) orientation have large spin Hall angle ($\theta_{SH} \cong 10.7$) and high electrical conductivity ($\sigma \sim 1.5 \times 10^5\ \Omega^{-1}m^{-1}$), which lead to ultrahigh efficient SOT magnetization switching of the $(Co/Pt)_2$ multilayers. Despite the perpendicular magnetic anisotropy (PMA) field of $(Co/Pt)_2$ is as large as 5.2 kOe, SOT magnetization switching was realized with a small DC threshold current density of 1.8×10^6 Acm^{-2} at H = 1.83 kOe. Robust switching was also realized by repeated 100 μs pulse currents.

In Chapter 5, low power and fast SOT magnetization switching was demonstrated in all-sputtered BiSb / perpendicularly magnetized CoPt / MgO multilayers on Si/SiO_x substrates. The magnetization can be efficiently switched by the spin Hall effect of BiSb with a relatively large spin Hall angle of 2.4. The magnetization of CoPt multilayers can be efficiently switched by a small threshold current density 2.3×10^6 Acm^{-2} at pulse width of 100 μs, which is close to that of the sample on sapphire substrate, under a small bias external field H = 183 Oe. Robust switching by repeated pluses and fast switching by pulses down to 100 ns was also realized.

In Chapter 6, element analysis by STEM and EDX was performed. In BiSb sputtering deposition, diffusion of Sb atoms to the FM layer reduces the PMA or influences the spin Hall angle. By evaluating the concentration of element in several samples by EDX spectroscopy, it becomes clear that Sb diffusion is a problem. Using an interlayer at BiSb – FM interface can be a solution that may further increase the device performance.

The research is concluded in chapter 7. The feasibility of BiSb growth by sputtering deposition on sapphire with large spin Hall angle of 10.7 and high electrical conductivity was demonstrated. In BiSb – FM heterostructures on Si/SiO_x, the spin Hall angle of BiSb can still be as large as 2.4 and the current density for magnetization switching is 1 order of magnitude smaller than that of other heavy materials. These works show the potential of BiSb as an effective spin current source for ultralow power SOT-MRAM and other SOT devices, such as spin Hall oscillator.